Spring 2018

Bedform Geometry and Bedload Sediment Flux in Coastal Wave, Current, and Combined Wave-Current Flows

Meagan Wengrove
University of New Hampshire, Durham

BEDFORM GEOMETRY AND BEDLOAD SEDIMENT FLUX IN COASTAL WAVE, CURRENT, AND COMBINED WAVE-CURRENT FLOWS

BY

MEAGAN E. WENGROVE

M.S. Civil Engineering, University of New Hampshire, 2012
B.S. Civil Engineering and International Affairs, University of New Hampshire, 2010

DISSERTATION

Submitted to the University of New Hampshire
in Partial Fulfillment of
the Requirements for the Degree of

Doctor of Philosophy

in

Ocean Engineering

May 2018

This dissertation has been examined and approved in partial fulfillment of the requirements for the degree of Doctor of Philosophy in Ocean Engineering by:

Dissertation Director, Diane L. Foster,
Director of the Ocean Engineering Program and Professor of Mechanical Engineering

Thomas C. Lippmann,
Associate Professor of Oceanography

Matthieu A. de Schipper,
Assistant Professor of Coastal Engineering

Christopher M. White,
Associate Professor of Mechanical Engineering

Anthony Lyons,
Research Professor

on 13 April 2018.

Original approval signatures are on file with the University of New Hampshire Graduate School.

To the ocean-human connection... may enhanced physical understanding of coastal dynamics aid in a resilient relationship between people and the shorelines we occupy.

ACKNOWLEDGMENTS

First off, I would like to acknowledge my advisor, Diane Foster, for her continuous support in my academic and personal endeavors. From the highs of receiving fellowships and job offers to the lows of being offered a *clean* sock from your floor... Diane, your mentoring in science and interpersonal connections has truly helped me to grow over the past eight years since we met. I look forward to passing along lessons and larks I have learned from you to my own students.

I would like to truly thank my insightful committee members Tom Lippmann, Matthieu de Schipper, Chris White, and Tony Lyons, for their guidance and intellectual input over the duration of my Ph.D. From deploying a bunch of instruments in the field and interpreting their data to discussing the interplay between small-scale and large-scale morphology and the momentum and transport gradients that play a role in shaping them, you each have significantly shaped the direction of my work.

I would like to acknowledge other intellectual input and field help from faculty, researchers, and graduate students over the last four and a half years. Jim Irish, Joe Calantoni, Rob Holman, Marcel Stive, Tom Weber, Sylvia Rodriguez-Abudo, Donya Frank, Reza Ebadi, Dan Hagan, Ad Reniers, Drummond Biles, Emily Carlson, Alex Padilla, Joe Klewicki, John Hughs-Clark, Larry Mayer, Brian Calder, Dirk-Jan Walstra, Larry Ward, Mike Allard, Max Radermacher, Martijn Henriquez, Jon Hunt, Nick Cohn, Bonnie Ludka, Bas Hoonhout, Steph Gilooly, Brandon Montemuro, Marion Tessier, Simion Moons, Kara Koetje, Salme Cook, Josh Humberston, John Turner, Kate von Krusenstiern, Sarah Blagdon, Sierd de Vries, and other past and present UNH OE, ME, and CCOM graduate students and faculty as well as TUDelft Hydraulic Engineering graduate students and faculty.

My Ph.D. could not have been completed without funding from the Department of Defense National Defense Science and Engineering Graduate Fellowship Program for three years of personal support, and The PADI Foundation grant that funded much of the field

experiment data collection in the Netherlands. Additionally, UNH Mechanical and Ocean Engineering and TUDelft Hydraulic Engineering have financially supported me at times while working toward my Ph.D. I would also like to acknowledge the UNH Marine School and the UNH Graduate School for financially supporting much of my travel to present my work at national and international conferences.

Finally, I am very grateful to my friends and family for their emotional support, ability to have fun, and laugh over the last four and a half years. Thank you to my mom, dad, and sister, Kim, Jim, and Ashley Wengrove, my adventure and life partner, Drummond Biles, and my close friends from childhood through graduate school from around the country and the world. My sanity at times depended on you, thank you.

TABLE OF CONTENTS

LIST OF TABLES

Table **Page**

LIST OF FIGURES

Figure **Page**

ABSTRACT

Bedform Geometry and Bedload Sediment Flux in Coastal Wave, Current, and Combined Wave-Current Flows

by

Meagan E. Wengrove

University of New Hampshire, May, 2018

Ripples and megaripples aggregate our coastlines, inlets, and rivers. This dissertation provides evidence for the contribution of small scale bedform migration to the evolution of larger coastal morphology. Using the connection between scales as a justification for continued research into the dynamics of growth and sediment flux associated with the mobility of ripples and megaripples in our coastal areas, this dissertation examines the dynamics between current dominant, wave dominant, and combined wave-current dominant bedforms on the multi-ripple and intra-ripple scales. Finally, this dissertation proposes that the bedload sediment flux is correlated with the total kinetic energy in the flow field ($Q_b = f(E_{k_{wc}})$) as well as the bed shear stress ($Q_b = f(\tau_b)$). However, the results provide evidence to suggest that the kinetic energy formulation may provide higher skill than shear stress based models when detailed boundary layer measurements are unavailable.

On the multi-ripple scale, bedforms are shown to have an adjustment time scale for growth or decay that is a function of the total kinetic energy in the flow. The relationship between the bedform volumetric growth or decay and the bedload sediment flux is modeled using a time varying sediment continuity analysis. Additionally, findings show that the bedload sediment transport associated with bedform migration is a function of the total kinetic energy in the flow field. The bedload sediment transport is shown to be robustly modeled using a modification of the energetics set of bedload transport equations regardless of whether the flow is current dominant, wave dominant, or combined wave-current flow, such that the structure for a combined roughness and bedload transport model is outlined supporting $Q_b = f(E_{k_{wc}})$. The unified model may be applicable to predicting large scale coastal change without dependence on a robust estimate of the bed shear stress.

On the intra-ripple scale, dynamics of bedload transport were investigated in both mean flows and oscillatory flows at the mobile sediment layer of the ripple crest. The mobile bed layer was shown to have a decay in applied stress with up to an 80% reduction in shear stress between the top of the mobile layer and the immobile layer, and a sign change of the applied shear stress at the immobile surface in oscillatory flow. At some of the smallest scales of sediment transport, findings have implications for understanding the mechanisms of bedload transport under waves and currents as well as the shear structure within the mobile layer. A momentum integral method formulated to estimate the bed/wall shear stress was validated and extended to investigate the gradients of momentum through the mobile layer as well as through separated flows and flows around complex geometries. The technique will be useful to investigations with detailed measurements or simulations of the boundary layer momentum structure.

CHAPTER 1

INTRODUCTION

1.1 Motivation and Background

Nearshore coastal regions (e.g. beaches between the intertidal zone and the offshore sandbar and coastal inlets) are morphologically dynamic areas that are vulnerable to the impacts of storms, which are projected to increase in intensity with pressures of climate change (IPCC, 2014; DoD, 2018). Within these coastal systems, flow fields are complicated by combined wave and current forcing; where at times flows could be wave dominant (the flow kinetic energy is in majority due to wave propagation), current dominant (the flow kinetic energy is in majority due to mean flows, e.g. tides, longshore currents), or combined wave-current flows, defined in this dissertation with the fraction of hydrodynamic kinetic energy due to waves between 25% and 75% of the total flow energy (Grant and Madsen, 1979; Lacy et al., 2007). Additionally, the nearshore morphology is often superimposed with a range of scales of bedforms, like sand bars, sand ripples, mega-ripples, and dunes, adding the complication of morphologic scale and timescales associated with adjustment to the overall system dynamics (Clarke and Warner, 2004; Passchier and Kleinhans, 2005). In response to wave and current forcing bedforms in the nearshore zone transform in shape and can also migrate and thereby transport sediment (Bagnold, 1946; Grant and Madsen, 1979; Engelund and Fredsøe, 1982; Charru et al., 2013). Bedload sediment flux from bedform migration is a potentially large, yet unquantified, sediment source to system evolution (Clarke and Warner, 2004). However, bedform shape response to combined flows and bedload sediment flux within the nearshore zone in general are poorly characterized and predicted (Traykovski, 2007; Soulsby et al., 2012; van der A et al., 2013).

Ultimately, morphologic adjustment is a function of both the sediment transport rate, Q, and the roughness variability, r (Figure 1.1). There are a number of existing empirical and analytical models used to estimate bedform geometry, bed shear stress, and the resulting bedload sediment flux in the nearshore, where hydrodynamics are generally complicated by wave or combined wave-current flows (e.g. van Rijn (1993), van Rijn et al. (2004), van Rijn (2007), van der A et al. (2013), (Soulsby, 1997), Meyer-Peter and Muller (1948), Styles and Glenn (2000),Soulsby and Damgaard (2005), Soulsby and Clarke (2005)). Yet, when employed within regional scale coastal change models (e.g. ROMS COAWST, Delft3D, FVCOM) and compared to field measurements, these empirical and analytical models under-predict morphologic change and sediment transport rates, especially in high energy and combined flow events (Bosboom et al., 2014).

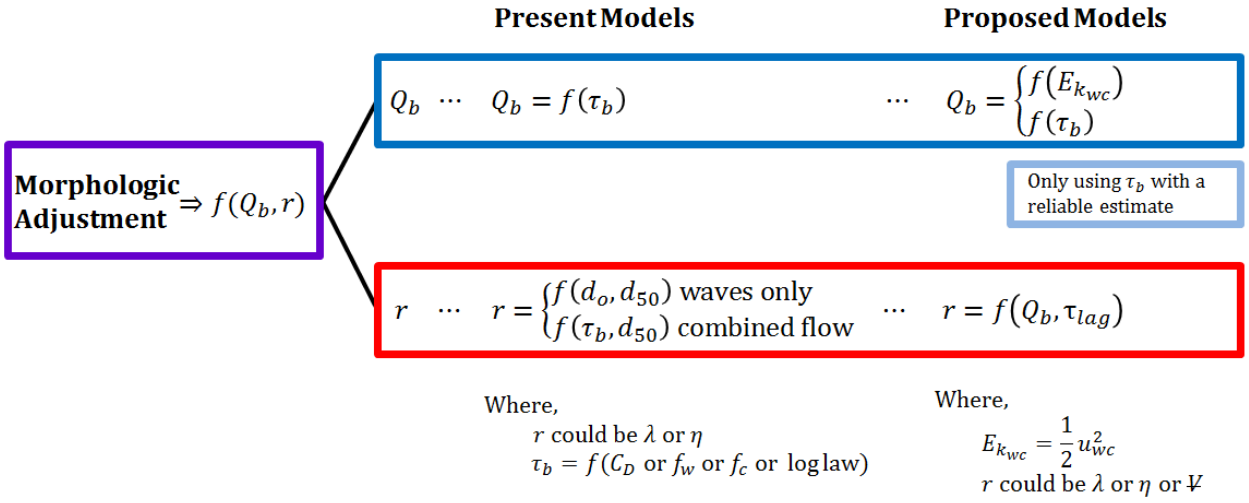

Figure 1.1: Schematic of key relationships for morphologic adjustment. Purple outlines the topic of Chapter 2. Red outlines the topic of Chapter 3. Dark blue outlines the topic of Chapter 4. Light blue outlines the topic of Chapter 5. A list of symbols can be found as Appendix A.

Generally, such models use sediment transport modules that relate bedload sediment flux, Q_b, to bed shear stress, τ_b, ($Q_b = f(\tau_b)$) to predict morphologic change (Lesser et al., 2004; Warner et al., 2008) (Figure 1.1), where bed shear stress estimates are dependent

upon both imposed flow conditions and boundary roughness (e.g. bedform geometry, grain size) (Engelund and Fredsøe, 1982; Charru et al., 2013). Although the applied bed shear stress is ultimately the force that mobilizes sediment, in the nearshore zone where boundary layer flows are complicated by combined flows and the presence of bedforms, τ_b is very difficult to estimate. Many sediment transport models attempt to estimate τ_b either by assuming a logarithmic shape to the boundary layer velocity profile using a law of the wall relation to estimate stress, or use current and wave friction factors or drag coefficients to estimate stress (Nielsen, 1992). In most nearshore regions, the logarithmic shape assumption is invalid because the shape of the wave or combined wave-current boundary layer is not logarithmic (Jonsson and Carlsen, 1976). Additionally, depending upon the friction factor or drag coefficient used, bed stress estimates can vary by orders of magnitude (Nielsen, 1992).

Additionally, within such sediment transport models, bedform geometry or roughness is generally characterized using only wave statistic scaling, or scaled with estimates of τ_b in combined flows. Characterizing bedform height (η) and wavelength (λ) using wave statistics is generally accurate within wave dominant flows (Clifton and Dingler, 1984). However, within combined flows the scaling relations breakdown and, again, methods used to estimate τ_b generally make assumptions of flow field characteristics that may not represent the physics.

1.2 Dissertation Propositions

This dissertation aims to demonstrate that small scale bedform adjustment is important to large scale morphologic evolution (Chapter 2), which motivates the further understanding of mechanisms for bedform adjustment in the complicated combined wave-current flows that influence many of our nearshore regions (Figure 1.1). Following, Chapter 3, 4, and 5 provide evidence for using the flow field kinetic energy, $Q_b = f(E_{k_{wc}})$, in place of $Q_b = f(\tau_b)$ to estimate sediment transport rates and thereby bedform roughness volumes; proposing that $Q_b = f(E_{k_{wc}})$ may be more robust and suitable to natural and numerical environments where detailed boundary layer measurements are unavailable. Fundamentally, contributions

of field and numerical observations of bedform evolution were made that allow for increased understanding of the mechanisms that cause transformation and migration of bedforms in nearshore environments. Practically, contributions are made in the form of methods to predict morphologic roughness volume, shear, and transport in response to wave and combined wave-current flow fields.

1.3 Dissertation Organization

The dissertation is in the form of four journal publications that address the mechanisms of morphologic adjustment from the localized system scale (Chapter 2) to the detailed scale of the mobile sediment layer over individual ripples (Chapter 5). The framework for this dissertation is summarized with the morphologic adjustment schematic (Figure 1.1) along with the following outline and summary of chapter content. Each chapter begins by introducing the background and methodology used for the content of that chapter, additionally the language and tense used within each chapter is consistent to that of the journal that it was or will be submitted and coordinate systems used within the chapter are defined in the methodology. Finally, this dissertation presents a conclusion and future work that remarks on the connections and continuity between chapters.

- Chapter 2 motivates the importance of the topic of this dissertation research by working to answer the question, do sand ripples actually matter to morphologic change? A unique set of field observations are used to show for the first time that it may be that sand ripples are feeding larger morphologic features (sandbars) in the surfzone. Chapter 2 provides a foundation and justification for study of the subsequent chapters of this dissertation (purple shading in Figure 1.1).

- Chapter 3 addresses the mechanisms for morphologic roughness adjustment in wave dominant, current dominant, and combined wave-current flows. Using field observations Chapter 3 demonstrates that the sediment transport potential of and the duration of time that the bed is exposed to a particular flow field can be used to estimate bedform

roughness volume with the time integrated sediment continuity equation. Additionally, two of the most relevant existing roughness prediction models are evaluated (red shading in Figure 1.1).

- Chapter 4 addresses the prediction of bedload sediment flux in the nearshore region. Field observations are used to show that bedload sediment flux can be accurately represented with the total energy in the flow field in all of wave dominant, current dominant, and combined wave-current flows. Chapter 4 additionally evaluates a set of existing bedload transport models for combined wave-current flows that are both a function of the estimated bed stress, τ_b, and the kinetic energy in the flow field, $E_{k_{wc}}$. In many field scale measurement campaigns, as well as with system scale morphologic adjustment models, high resolution boundary layer statistics are difficult to measure or model, so Chapter 4 uses field observations to support the idea that in these environments it may be more accurate to consider $Q_b = f(E_{k_{wc}})$ rather than $Q_b = f(\tau_b)$ (dark blue shading in Figure 1.1).

- Chapter 5 focuses on the idea that if high resolution measurements or numerics of the boundary layer gradients are captured, then, $Q_b = f(\tau_b)$ may hold. With respect to bed shear stress, in general, stress approximations used within wave and combined flows make assumptions regarding the physics of the boundary layer shape, and therefore can be inaccurate, or vary widely based upon the used approximation. In order to accurately estimate the bed shear stress, *a priori* assumptions of boundary layer shape should not be made, especially relevant to wave and combined flow boundary layers. Results show that over mobile sediment beds the effective bed stress at the top of the mobile sediment layer can be larger in magnitude for both unidirectional and oscillatory flows and even opposite in sign for oscillatory flow from the immobile sediment layer bed stress. Therefore Chapter 5 suggests that bed shear stress should only be be estimated within unsteady, non-fully developed, or oscillatory flow fields when measurement or

model resolution can capture near bed boundary layer gradients until a representative constitutive relationship for momentum gradients in the mobile layer is developed. In addition to showing numerical evidence that estimating bed shear stress over sediment beds is not trivial, Chapter 5 introduces a momentum integral method for estimating bed shear stress in unidirectional and oscillatory flows (light blue shading in Figure 1.1).

CHAPTER 2

SAND RIPPLES: SMALL-SCALE FEATURES FEEDING LARGE-SCALE MORPHOLOGY

2.1 Abstract

Do sand ripples contribute to larger morphologic change? Field observations of bedform migration and sandbar evolution in the surfzone provide strong evidence for the case that sand ripples may aid in the net volumetric change of larger morphologic features, like a sandbar, which is approximately 100x larger than the sand ripples. The small-scale sand features were found to transport $\sim$ 450 averaged sized wheel barrows of sand through the surfzone every single day. Using the sediment continuity equation, we show that sediment transport associated with sand ripple migration is consistent with the net volumetric change of a local transverse sandbar sandbar over time. Our results suggest that there is a link between small-scale morphologic mobility and large-scale coastal evolution in the surfzone, and should be considered for understanding morphodynamics on the large scale.

For reference see: Chapter 3, Chapter 4, and Appendix B

2.2 Introduction

Nearshore coastal regions (e.g. beaches between the shoreline and the seaward sandbar and coastal inlets) are morphologically dynamic areas where large populations recreate, work, and live (CEM, 2002; Pendleton and Kildow, 2006; Elko et al., 2014). Public and private institutions have taken interest in prediction of coastal morphodynamics with the goal of limiting vulnerability of population centers and military assets, especially with the imminent pressures of sea level rise, increased storm intensity, and climate change (IPCC, 2014; DoD,

2018). Within these coastal cells a range of morphologic scales co-exist from entire shorelines O(1 km to 100 km) to sandbars and sand waves O(50 m to 1000 m) to sand ripples and megaripples O(0.01 m to 50 m). There is a longstanding debate as to whether smaller scales of morphology are mechanisms for larger coastal evolution, or if these perturbation features are only peripheral to net morphologic adjustment (Bagnold, 1946; Dalrymple and Rhodes, 1995; Passchier and Kleinhans, 2005; Winter et al., 2008; Murray et al., 2009). A debate that reflects on a community-wide knowledge gap that points to a lack of understanding for the feedback mechanisms between geomorphology developing on different temporal and spatial scales (Terwindt and Wijnberg, 1991; Sherman, 1995; Summerfield, 2005; Lefebvre et al., 2013). So, we ask, do sand ripples of order centimeters significantly contribute to larger morphologic change?

On the latter side of the debate, arguing that small-scale morphology is peripheral to net morphologic profile change, asserts that basing full coastal system analysis on its building blocks (i.e. sand ripples) may not be representative of system change (Murray et al., 2009). Small scale bedforms are thought to be in a state of superposition with the larger morphology and translate over large morphology but have no effect on the larger scale morphodynamics (Allen and Collision, 1974; Dalrymple and Rhodes, 1995; Winter et al., 2008). Similarly, a long standing coastal cross shore profile envelope model contends that the coastal profile is in or adjusting towards a state of equilibrium and does not significantly vary with small-scale morphology (e.g. bedforms and sandbars) (Dean, 1991).

In contrast, equilibrium beach profile models are shown to perform poorly in the surfzone, where migrating bedforms and evolving sandbars are most prevalent (Ludka et al., 2015), suggesting that medium- and small-scale bedforms may be responsible for net morphologic change in that region. Furthermore, at the medium-scale, in support of smaller scale features feeding larger coastal change, it is shown that sandbar welding (the process where a sandbar migrates toward the coast and attaches to the shoreline) is a significant source of sediment to prograding beaches (Aagaard et al., 2004; Price and Ruessink, 2011; Ruggiero

et al., 2016). Moreover, at the ripple and megaripple scale, it has been shown that the presence of bedforms affect both the magnitude and direction of sediment flux in the nearshore region (Saulter et al., 2003; Aagaard et al., 2000; Wengrove et al., 2018b). Additionally, in estuarian systems there is evidence of megaripples driving sand wave migration (Dalrymple, 1984) and in river systems it is shown that bedload transport and transport due to bedform migration are nearly the same (Dietrich and Smith, 1984). Although, in the surfzone the link between bedform induced transport and larger scale morphologic change has not yet been proven, there is evidence to show that sand ripples, mega-ripples, and dunes aggregate coastal systems (Clarke and Warner, 2004), suggesting that the cumulative prevalence of sand ripples and megaripples may contribute significantly to the net sediment flux.

In this work, we link sediment flux between the ripple scale and larger coastal evolution in the surfzone. Field observations show evidence for small-scale bedforms (0.20 - 2.5 m) contributing to the evolution of a local shore attached transverse sandbar (50 m wide, 150 m long) and net erosion patters of the region between the shoreline and the shore parallel sand bar. Our results have implications to fundamental feedback mechanisms for morphologic evolution on various space and time scales, a relationship that is not singular to underwater geomorphology.

2.3 The Spectrum of Morphologic Scales

In coastal systems there exists a spectrum of morphologic scales. In a typical coastal system the largest scale of morphology is the coastline, medium-scales are the sandbars, and small-scales are the sand ripples and megaripples. For our analysis, the largest morphologic scale in our system is the Sand Engine system on the Delfland coast of the Netherlands.

The curved Sand Engine 'meganourishment' was installed in 2011 by depositing 21.5 million cubic meters of sand on the coast. For context, the Sand Engine is a *Building with Nature* campaign, where it uses naturally existing waves and currents to push the nourishment alongshore into erosive areas of of the coast, such that the nourishment is

meant to diffuse over time and last for a period of over 20 years (where typical nourishments installed to protect the coast and create recreational beach width only last for 4-5 years) (de Schipper et al., 2016). Moving forward, the system has dramatically changed shape over time (Stive et al., 2013; de Schipper et al., 2016). In 2011 it stretched 2 km in the alongshore and 1 km into the North Sea (Figure 2.1a upper panel), and in 2014 it stretched 4 km alongshore and 800 m in the cross shore (Figure 2.1a lower panel) (Radermacher et al., 2017; Wengrove et al., 2018b). On the largest scales considered, the morphology of the Sand Engine evolved significantly.

At medium-scales, shore parallel and transverse (shore perpendicular) sandbars at the tip of the Sand Engine were observed during a field experiment in 2014. A series of large-scale bathymetric surveys, obtained with a jet ski equipped with an echo sounder and GPS positioning were measured on day of year 256 [23 Sept.], 284 [11 Oct.], and 291 [18 Oct.], and were used to capture medium-scale sandbar dynamics. These sandbars had observable bathymetric changes over periods of days to months (Figure 2.1b). Over a period of just 4 weeks (23 Sept. 2014 [day of year 256] to 18 Oct. 2014 [day of year 291]) the transverse sandbar (highlighted in Figure 2.1b) migrated 50 m toward the northeast (Figure 2.1b Δz panel).

Our overarching effort was focused on the dynamic nature of the small-scale morphology at the seaward tip of the Sand Engine and its response to combined wave-current flow forcing (Wengrove et al., 2018b,a). Field data of the small-scale bedform dynamics were also collected at the tip of the Sand Engine during the 2014 experiment. Bedforms were shown to range in wavelength between 12 cm to 2.5 m with heights between 2 cm and 0.4 m, with migration rates up to 6 cm/min. dependent on the hydrodynamic energy in the overlying waves and currents (Wengrove et al., 2017, 2018b,a). During the four week experiment two sonars were deployed offset in the cross shore direction by 66 m between the seaward sandbar (50 m further seaward) and the shoreline (20 m further shoreward). Additionally, the stations were offset by 7 m in the alongshore direction and positioned southwest of

a migrating transverse sandbar (Figure 2.1b; see Wengrove et al. (2017), Wengrove et al. (2018b) for details of field and analysis methods). The further seaward station was deployed for 2 weeks (day of year 275 to 291), while the further shoreward station was deployed for 4 weeks (day of year 269 to 296). The sonars collected a time series of imagery of bedforms with sampling frequency capable of quantifying bedform migration and transformation. Images captured over a 4 hour period show a snapshot of the dynamic nature of the sand ripples (Figure 2.1c) (Wengrove et al., 2017, 2018b,a).

Overall, Figure 2.1 shows the range of temporal and spatial scales of morphology present at the Sand Engine. The meganourishment is dynamic on periods ranging from minutes to years and spatial scales ranging from cm to km. Our work shows evidence for the sand ripples and megaripples migrating through the surfzone (Figure 2.1c) having influence on the evolution of the transverse migrating sandbar (Figure 2.1b).

2.4 How much sand do bedforms move?

The amount of sand that bedforms move is dependent upon the bedform migration rate and the bedform height (Traykovski et al., 1999; Wengrove et al., 2018a), but is also characteristic of the individual system sand grain size distribution and density, as well as hydrodynamic wave forcing, current forcing, and water depth. During the 4 week experiment, the observations revealed that bedforms were found to move as much as 1.7 m^3/m and an average of 0.26 m^3/m of sand per day (Figure 2.2).

With the two stations positioned in the cross shore direction, a simple estimation of sediment flux mobilized by bedform migration between the shoreline and the sandbar was approximated with two basic assumptions. The first is that there are bedforms in the region between the sandbar and the shoreline (Clarke and Warner, 2004). The next assumption is that the amount of sand moving through the cross shore array (see Figure 2.1b from the shoreline through both stations to the sandbar) can be estimated by integrating transport rates estimated from observations of bedform migration. The approximation yields that

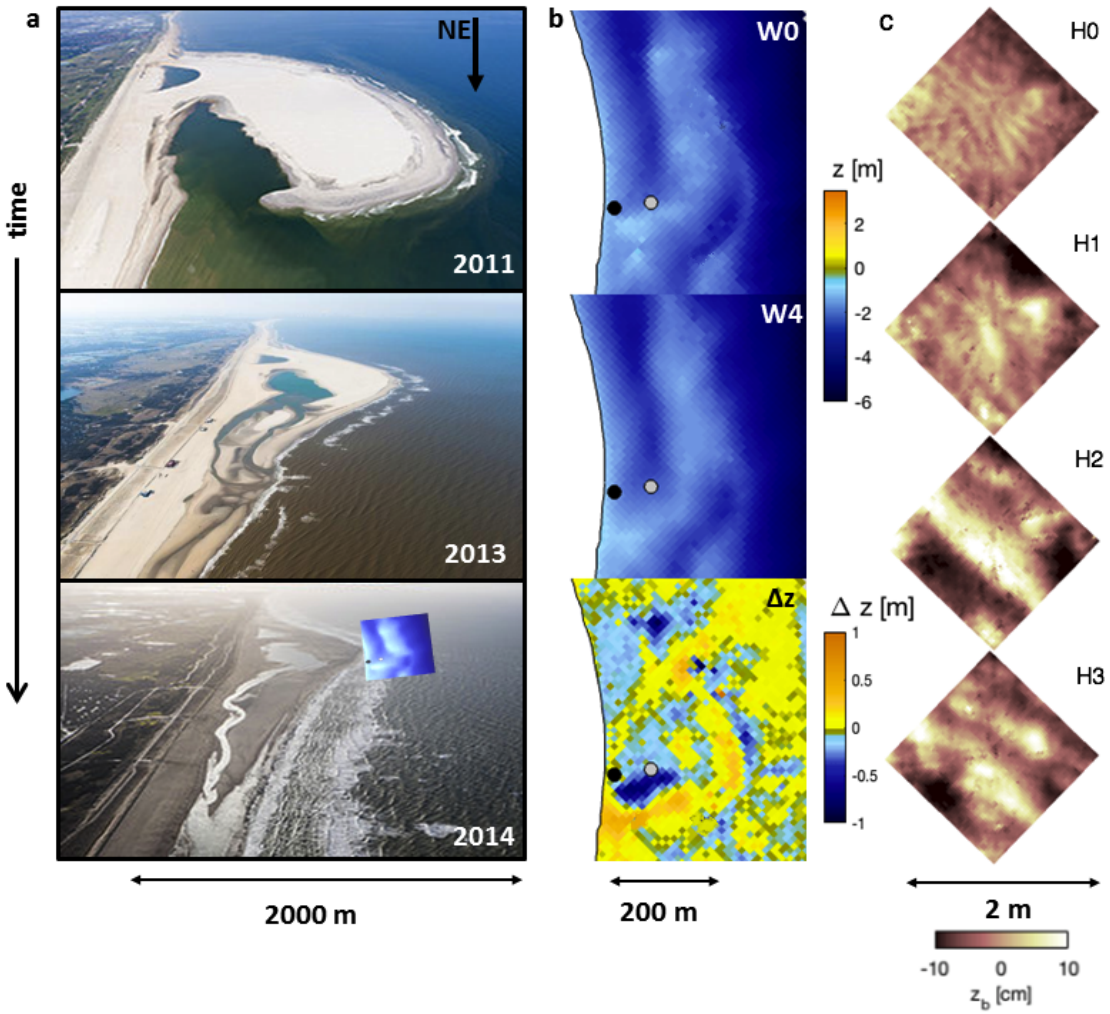

Figure 2.1: Scales of morphology and their evolution through time at the Sand Engine meganourishment. Panel a) shows the full nourishment evolution from 2011 through 2014. Panel b) highlights the transverse sandbar evolution from bathymetric surveys over a four week (W0 to W3) period during the 2014 experiment (top two panels), with the bottom panel showing the change between the upper panels, blue is erosion and orange is accretion. The solid black line to the left of each panel is the approximate position of the low water shoreline. The location of the bathymetric surveys is at the tip of the Sand Engine, shown in panel (a-2014). The deployed sonar stations are shown with black (shoreward) and grey (seaward) dots. Panel c) shows an hourly time series of measured bedform elevation (z_b) sampled at the shoreward sonar station highlighted in panel (b). When looking at the images, it is as if you are looking down at the bedforms from above and observing them change from very small wavelengths driven by waves (H0), to wavelengths over 1 m driven by combined wave-current flows (H3), with the shoreline to the left of the images. Scale bars for all panels are shown at the bottom of the figure, time is indicated running from the top to the bottom panel on the left side of the figure, and for all panels the geographic orientation is shown in panel (a-2011), with the northeast direction pointing downward. The predominant flood tidal current is directed toward the northeast.

there is on average 33 m^3 of sand per day passing through this 130 m transect between the shoreline and the shore parallel sandbar (that is ∼450 average sized wheelbarrows every single day) and about 45% of this volume was directed alongshore toward the northeast in the direction of the transverse sandbar. Such that, qualitatively, the bedload sediment flux due to the bedform migration is in the same direction as the transverse sandbar evolution.

If we assume that bedforms aggregate through the full sandbar system area, we can look at how much sand the bedforms may be responsible for moving. The net bed level change within the two pairs of considered bathymetries shows approximately a 5% net loss in sand within the sandbar system over the duration of time between surveys (that is $\sim$ 186 m^3 between 11 Oct. and 18 Oct. and $\sim$ 664 m^3 between 23 Sept. and 18 Oct.). If the small scale bedform volumetric flux in the cross shore and alongshore directions are applied along the length of the cross shore and alongshore borders of the sandbar system, respectively, then we find that the bedforms transport approximately 80% of the net sand lost to the system over the duration between the survey pairs (that is $\sim$ 120 m^3 between 11 Oct. and 18 Oct. and $\sim$ 628 m^3 between 23 Sept. and 18 Oct.). Such a relationship demonstrates that the sediment flux due to bedform migration is consistent with the volume of sand lost to the transverse sandbar during the survey periods.

2.5 The Net Flux

The sediment continuity equation is used to quantify the relationship between net bedform sediment flux and the transverse sandbar evolution. The sediment continuity equation is a balance between the spatial sediment flux gradient (the sediment divergence) and the temporal vertical bed level gradient,

$$\frac{dq}{dx} + \frac{dq}{dy} = -n\frac{dz_b}{dt}, \tag{2.1}$$

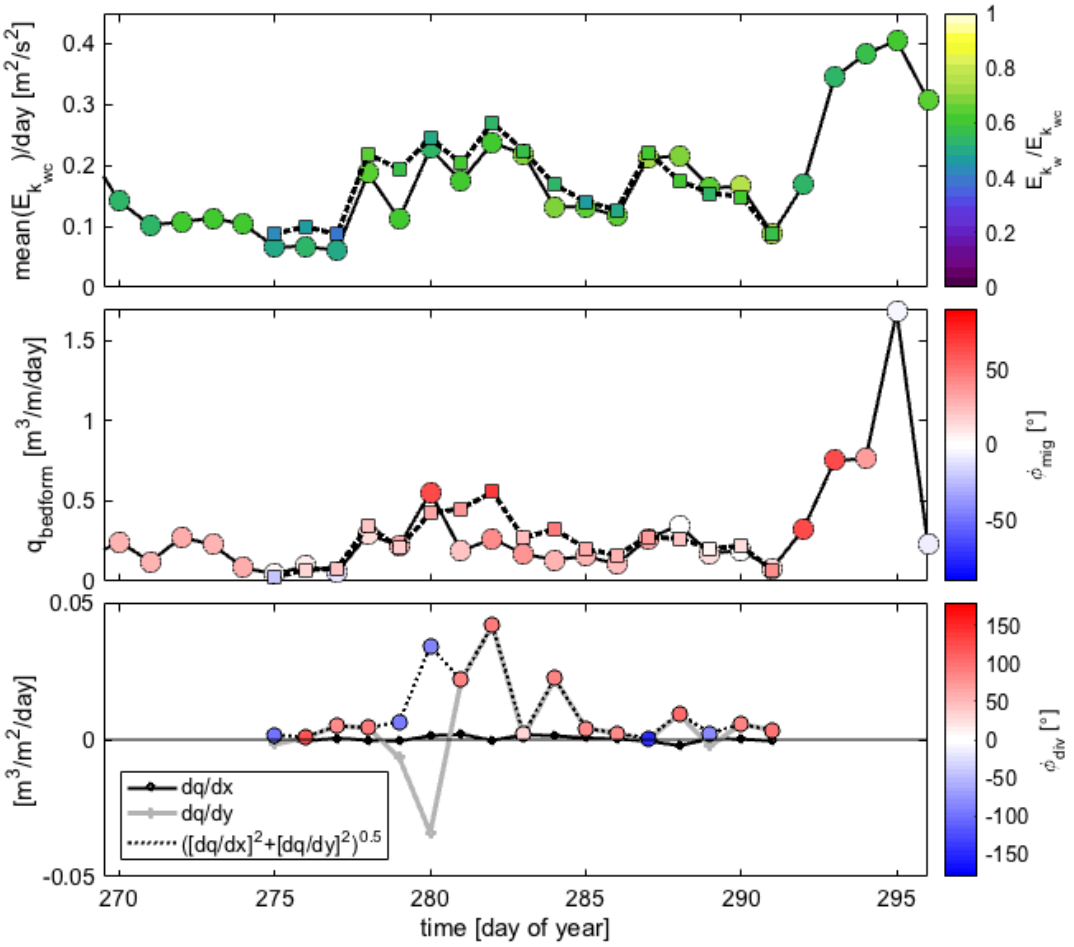

Figure 2.2: Time series of relevant hydrodynamic and sediment quantities. Panel a) shows the daily averaged total kinetic energy in the combined waves and currents ($E_{k_{wc}} = \frac{1}{2}u_{wc}^2$, where u_{wc} is the combined wave current velocity), used as a surrogate for strength of the orbital velocity of waves and mean current magnitudes, and colored by the fraction of kinetic energy due to waves. Panel b) shows the daily averaged magnitude of the bedform sediment flux calculated from bedform observations and is colored by the bedform migration direction, where +90° is directed alongshore toward the northeast and -90° is directed alongshore toward the southwest. Panel c) shows the daily averaged magnitude and direction of the cross shore sediment divergence (black), alongshore sediment divergence (grey) and divergence magnitude colored by direction with orientation consistent with (b). For (a) and (b) the circle markers are the shoreward sonar station and the square markers are the seaward sonar station from Figures 2.1 and 2.3.

where q is the volumetric sediment flux, x is the cross shore and y is the alongshore direction (either or both can be used in the analysis), z_b is the bed level, t is time, and $n = 0.7$ is the assumed sediment packing factor.

The cross shore and alongshore daily averaged sediment flux time series is shown in Figure 2.2b for each station as well as with vectors in Figure 2.3. In general the daily averaged sediment flux was directed just northeast (40°) of shore normal for most days, with the larger flux rates occurring during spring flood tides (day of year 269-274, 279-285, 293-295) and during storm conditions (day of year 278, 280, 287, 294). Generally, both stations follow the same trends with magnitude and direction of sediment flux, with the exception of the storm event between day of year 280-283, during which time the wave driven alongshore current was stronger at the further seaward station.

The estimated cross shore sediment divergence (dq/dx) is small (Figure 2.2c), signifying that in the cross shore direction the sand that passed through the seaward station also passed through the shoreward station. However, in the alongshore direction (dq/dy) there was a larger gradient in transport, showing that more sand passed through the seaward station than the shoreward station. The net combined cross shore and alongshore time integrated divergence between the two stations had a magnitude of 0.08 $\pm$ 0.010 m^3/m^2 and was oriented in the direction of the transverse sandbar evolution (Figure 2.3). The significance of the divergence magnitude in light of (1) is that there was a net 0.08 m bed level change over the two week period (consistent with observations of bed level change at both stations), and the sediment eroded between the two stations was moved toward the northeast, again in the direction that the transverse sandbar migrated.

To take this analysis a step further the sediment continuity equation, (1), is used to compare the alongshore sediment divergence to the net bed level change of the transverse sandbar system. The set of bathymetric surveys taken 7 days apart on 11 Oct. 2014 (day of year 284) and 18 Oct. 2014 (day of year 291) while both sonar stations were in the water, show signature of the sandbar evolving in the northeast (alongshore) direction. Over

this week the time integrated alongshore divergence (dq/dy) between the two stations was -0.035 $\pm$ 0.010 m^3/m^2, and the spatially integrated bed level change of the transverse sandbar system normalized by the system area had a comparable net erosion of -0.047 $\pm$ 0.012 m^3/m^2. The spatial extent of the transverse sandbar system was defined with in the cross shore by the position of the seaward and shoreward sonar station locations and in the alongshore with southwestern border as the southwestern side of the sandbar erosional area and as the northeastern side of the sandbar accretional area. The error was estimated following (de Zeeuw et al., 2016). Furthermore, if this same analysis is completed for the bathymetric surveys taken between 23 Sept. 2014 (day of year 256) and 18. Oct. 2014 (day of year 291) the time integrated alongshore divergence was -0.059 $\pm$ 0.010 m^3/m^2 and the spatially integrated bed level change of the transverse sandbar system normalized by the system area was -0.063 $\pm$ 0.011 m^3/m^2, again, very closely comparable erosion depths. For the latter, the sonar stations were not deployed for the entire period between the bathymetric surveys, so an assumption of temporal comparability in the alongshore divergence was made for the calculation. While it is tempting to use this approach to estimate shoreline change in the cross shore direction, it may not be possible to extrapolate this analysis to the shoreline because of the high role of sheet flow and suspended sediment processes in that region.

The alongshore sediment continuity equation analysis relates the time integral of the sediment divergence to the normalized spatial bed level change of the transverse sandbar system. The sediment lost between the seaward and shoreward sonar stations was the same in magnitude as the net spatially averaged sand lost over the transverse sandbar system. Additionally, the gradient in transport was directed in the alongshore direction toward the northeast, in the same direction as the transverse sandbar evolution (Figure 2.3).

To comprehend the finding, we consider an ideal sandbar that does not gain or lose sand nor changes shape as it migrates. If this sandbar purely migrates, the net volumetric change of sand to the system will be zero, such that

$$\frac{\Delta Vol._{sb}}{A_{sb}} = \Delta z_b = 0, \tag{2.2}$$

where, $\Delta Vol._{sb}$ and A_{sb} are the change in sandbar volume and the planar area of the sandbar system, respectively, and Δz_b is the net bed level change. Our results show that small scale ripples have the ability to add or remove sand from the system over time, such that

$$\frac{\Delta Vol._{sb}}{A_{sb}} + -n \int \frac{dq_{bedforms}}{dy} dt = \Delta z_b \neq 0, \tag{2.3}$$

where, $q_{bedforms}$ is the volumetric transport rate from migrating bedforms through the two sonar stations separated in the alongshore by dy. The first term is the ideal sandbar net bed level change from (2) and the second term is the variability introduced from bedform migration through the system. Analysis shows that volumetric flux from the bedform migration is consistent with the net change in the volumetric sandbar evolution. It may be that the small scale bedforms not only migrate through the sandbar system, but also interact with the sandbar along the way, in this case removing sediment from the system.

The finding that sediment transport divergence associated with small-scale bedforms shown to be consistent with the evolution of larger scale morphology is independent of the region chosen to demonstrate the net bed level change. Previously the alongshore extents of the analysis region of bed level change were chosen to be that of the edges of the erosional and accretional masses, but we can also show that the result is independent of the analysis region chosen. Figure 2.4 shows the net average bed level change between the 23 Sept. and 18 Oct. surveys with incremental increases to the analysis region in the alongshore direction, and the new analysis regions were shifted alongshore ± 300 m of the sonar sampling stations. With the smallest box (shore parallel length of 50 m) the irregularity of coastal morphology are apparent as the box moves alongshore; however, when the box is centered on the transverse sandbar feature, there is an approximate 0.06 m of net erosion, consistent with previously presented findings. As the box size gets larger, it becomes less sensitive to shore parallel change and the trend of ∼0.06 m of net erosion prevails for the transverse sandbar, as seen by the flat region surrounding the center of the transverse sandbar erosional and accretional

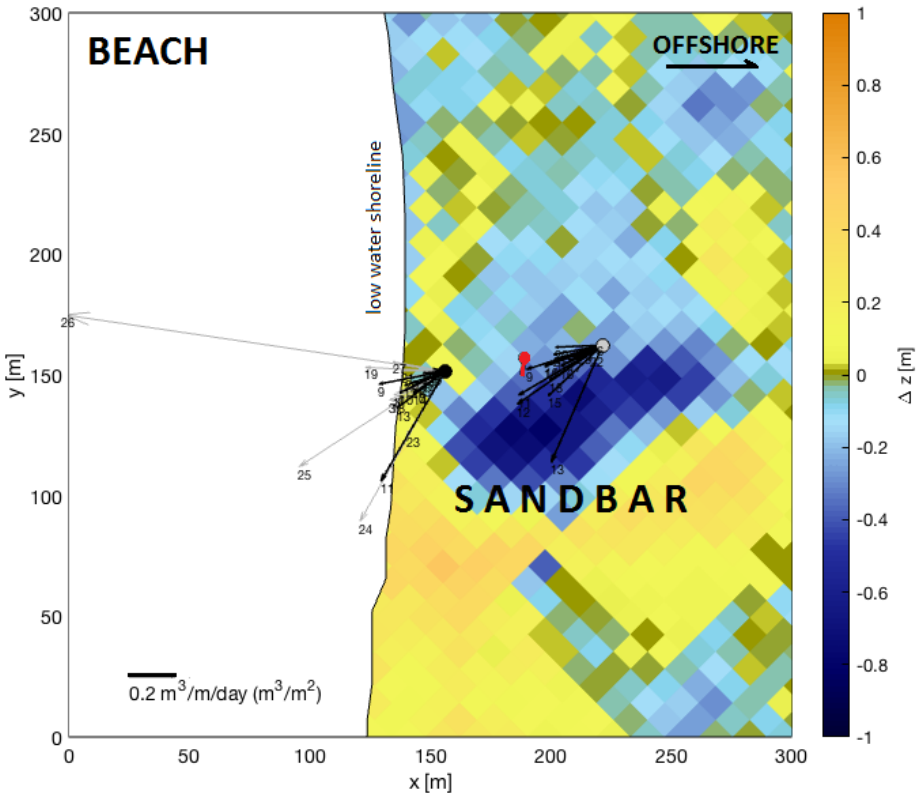

Figure 2.3: Bathymetric difference survey between 23 Sept. 2014 (day of year 256) and 18. Oct. 2018 (day of year 291) overlaid with daily averaged sediment flux vectors for each sonar station. The yellow and orange are areas of accretion and the blues are areas of erosion. The black vectors highlight the period of time when both sonar stations were deployed, and the grey vectors on the shoreward station show the remainder of measurements for that site deployment. The vectors are numbered according to their time position on Figure 2.2, with 1 being the first point in the time series. The red vector located between the two stations shows the magnitude and direction of the time integrated sediment divergence vector over the two week period while both stations were in the water (integrated from day of year 275 to 291 in Figure 2.2). A scale bar in the lower left corner indicates transport magnitude and (sediment divergence magnitude). Northeast is directed in the negative y direction.

volumes. With the largest box size, we can see that within ± 300 m from the sonar array, there continues to be an average net erosion of 0.06 m. The net erosional trend regardless of bed level analysis region demonstrates that bedform mobility may actually influence bedload transport and net morphologic change on larger scales than a ripple or a sandbar alone.

2.6 Conclusion

We present evidence for sand ripples feeding larger coastal morphologic change in the surfzone. We show through the sediment continuity equation that sand ripples transport as much sand as a local transverse sandbar system lost during the same period of time. Our results suggest that sediment transport divergence patterns observed through sand ripple migrations are consistent with larger patterns of net change in coastal evolution. Globally, our results suggest that if sand ripples can change coastlines, then there is possibility for feedback evolutions between scales in other geophysical systems.

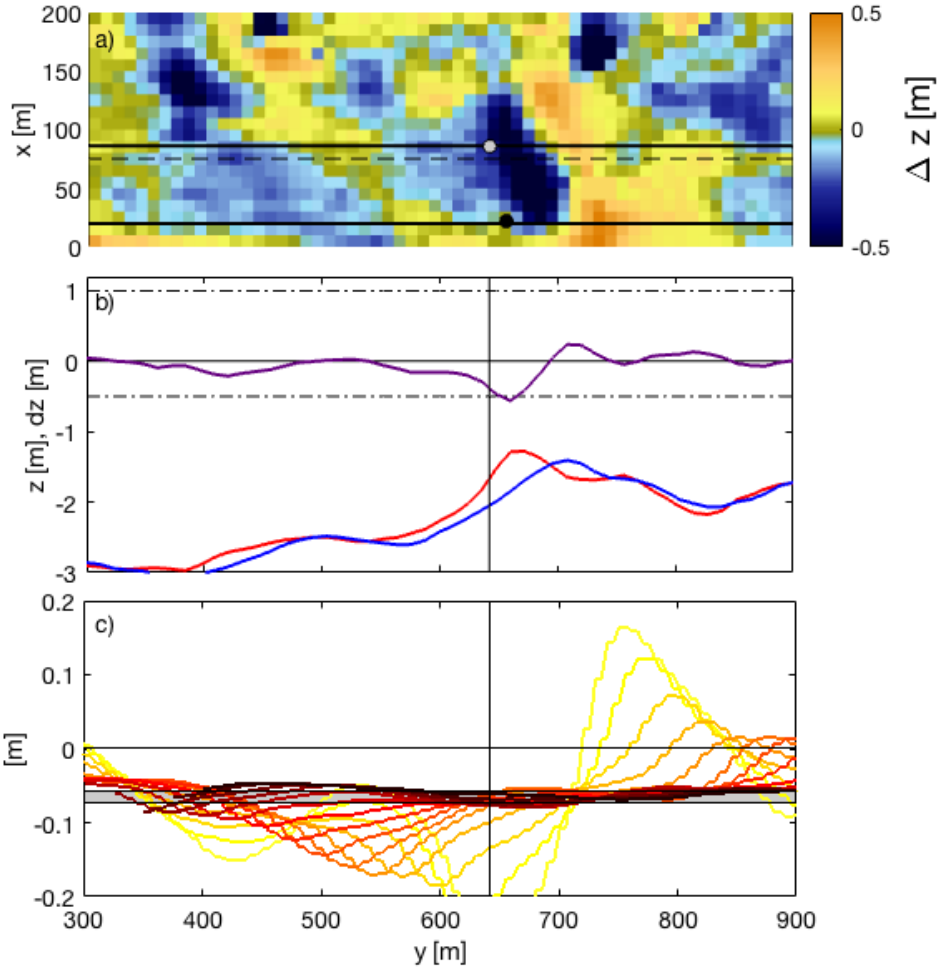

Figure 2.4: Alongshore analysis showing consistent patterns in bed level erosion. Panel a) shows a bathymetric difference survey between 23 Sept. 2014 (day of year 256) and 18. Oct. 2018 (day of year 291) with the shoreline curvature removed. The yellow and orange are areas of accretion and the blues are areas of erosion. The shore is at x = 0, the dots show the sonar sampling stations, the black solid lines are the shore parallel extents of the analysis region shown in panel c, and the black dashed line is the alongshore transect highlighting the transverse sandbar profiles shown in panel b. Panel b) shows the transverse sandbar profiles from 23 Sept. (red) and 18 Oct. (blue), and the difference between them (purple). The vertical black line shows the alongshore position of the sonar sampling stations. The horizontal solid black line shows the mean water level, the lower dashed black line shows the mean low water level, and the upper black dashed line shows the mean high water level, with respect to the red and blue sandbar profiles. Panel c) shows $\Delta Vol./\Delta A$ with with incremental increases to the analysis region in the alongshore direction (color) and 5 m shifts to the analysis region in the alongshore direction (y position). Yellow indicates a box size of 100 m with incremental increases of 50 m and line shade to a maximum box size of 800 m, shown in black (dark red is a box size of ∼600 m and light orange is ∼300 m). The gray shaded region shows the range of the maximum and minimum mean net bed level change found over the alongshore shifted analyses for each box size.

CHAPTER 3

OBSERVATIONS OF TIME DEPENDENT BEDFORM TRANSFORMATION IN COMBINED WAVE-CURRENT FLOWS

3.1 Abstract

Although combined wave-current flows in the nearshore coastal zone are common, there are few observations of bedform response and inherent geometric scaling in combined flows. Our effort presents observations of bedform dynamics that were strongly influenced by waves, currents, and combined wave-current flow at two sampling locations separated by 60 m in the cross shore. Observations were collected in 2014 at the Sand Engine mega-nourishment in The Netherlands. The bedforms had wavelengths ranging from 14 cm to over 2 m and transformed shape and orientation within, at times, as little as 20 minutes and up to 6 hours. The dynamic set of observations was used to evaluate the sediment transport continuity equation (Exner equation), relating changes in bedform volume to bedload sediment transport. Analysis shows that bedform volume was a function of the integrated transport rate over the bedform development time period. The bedform development time period (time lag of bedform growth/adjustment) may be estimated using the Exner equation and is compared with observations of bedform growth and decay made during the field experiment. Results show that this continuity principle held for wave, current, and combined wave-current generated bedforms.

For reference see: Appendix B, Appendix C, and Appendix F

3.2 Introduction

Time varying wave, current, and combined wave-current flows are characteristic of most nearshore regions (e.g. Grant and Madsen (1979); Passchier and Kleinhans (2005); Soulsby and Clarke (2005)). These complex hydrodynamic environments are additionally complicated with small scale bed roughness (e.g. sand ripples and megaripples) that have a two way feedback with the local hydrodynamics, apparent within nearshore modeling (Wikramanayake and Madsen, 1994; Lesser et al., 2004; Ganju and Sherwood, 2010). Previous research demonstrates that characteristic bedform roughness lengths (bedform wavelength and height) scale with the hydrodynamic forcing applied to the seabed under waves or currents (e.g. Fredsøe (1984); Clifton and Dingler (1984); Wiberg and Harris (1994); Traykovski et al. (1999); Hay and Mudge (2005)). However, there have been very few studies of bedform scaling and orientation in response to dynamically changing forcing that includes combined wave-current flows (Li and Amos, 1998; Hay and Mudge, 2005; Lacy et al., 2007; Soulsby et al., 2012; Nelson and Voulgaris, 2015).

For combined wave-current flows, most of the literature addresses the transition of bedforms between flow states with observations of relatively small bedforms with wavelengths of less than 0.5 m under relatively low energy wave conditions or with waves plus weak mean flow (e.g. Grant and Madsen (1979); Li and Amos (1998); Soulsby and Clarke (2005); Lacy et al. (2007); Soulsby et al. (2012)). Results of these efforts show that combined flow bedforms are less steep than wave dominant bedforms, and generally orient in a pattern influenced by the maximum gross bedform normal transport direction (Gallagher et al., 1998; Lacy et al., 2007). Additionally there are a few efforts that observe larger scale bedforms, like megaripples, forming in response to wave dominant flows or combined flows, but these efforts do not address characteristics of bedform response to transition periods (Gallagher et al. (1998); Gallagher (2003); Larsen et al. (2015)).

Observations of bedforms under wave dominant or current dominant flows suggests that bedform building is a time dependent process (e.g. Davis et al. (2004); Testik et al. (2005); Doucette and O'Donoghue (2006); Austin et al. (2007); Traykovski (2007); Soulsby et al. (2012); Nelson and Voulgaris (2015)). The bedform shape and volume is dependent on present hydrodynamic conditions, as well as past forcing. Time-dependent bedform models that estimate roughness length scales use a departure from equilibrium approach (e.g. Traykovski (2007); Soulsby et al. (2012)) that assumes bedform length scales are being driven toward equilibrium with the present hydrodynamic conditions. The assumption is generally valid for waves (Davis et al., 2004; Testik et al., 2005; Doucette and O'Donoghue, 2006; Traykovski, 2007); however, present equilibrium theory may not capture the physics of bedform adjustment in combined wave-current flows because the time constants associated with current models may not be appropriate to represent dynamics in combined flows (Austin et al., 2007).

In our effort, we present observations of ripple and megaripple formation in response to high energy combined flows with, at times, the addition of a strong current. Forcing conditions ranged from wave dominant flow, to combined wave-current flow, to mean current flow. Bedform transition periods and growth cycles were observed in response to the variable flow conditions. Additionally, the results demonstrate that the sediment continuity equation, or Exner equation, captures bedform building as a time dependent process, suggesting that the sediment continuity equation may be used to model dynamic roughness in the nearshore, especially relevant when considering combined wave-current flows.

3.3 Methods

3.3.1 Experiment and Instrumentation

Data was collected during a campaign at the Sand Engine mega-nourishment as a part of the MEGA-Perturbation EXperiment (MEGAPEX) in the fall of 2014 on the Delfland Coast of the Netherlands (Radermacher et al., 2017). Since the installment of the 21.5 million

cubic meters of sand in 2011, the Sand Engine has dramatically changed shape (Stive et al., 2013); in 2011 it stretched 2 km in the alongshore and 1 km into the North Sea, and in 2014 it stretched 4 km alongshore and 800 m in the cross shore (Radermacher et al., 2017). The large scale morphology is considered very dynamic with observable bathymetric changes over periods of days to months. Our effort investigates the dynamic nature of the small scale morphology at the seaward tip of the Sand Engine.

Local small scale morphology and hydrodynamics were observed between the shoreline and the shore-parallel sandbar that were 136 m apart at two cross shore stations, S1 and S2, at the tip of the Sand Engine (Figure 3.1a). S1 was located 20 m seaward of the low tide shoreline and S2 was located 66 m further offshore and 50 m shoreward of the subtidal sandbar. Morphology was sampled at each location with a stationary sweeping and rotating 1 MHz Imagenex 881a pencil beam sonar with a 3 m diameter footprint. S1 was sampled every 20 minutes with a 1.4° sweep step and a 2.4° rotation step from 26 Sept. to 23 Oct. 2014 (day of year 269-296), and S2 was sampled every 2 hours with a 1.4° sweep step and a 1.4° rotation step from 2 Oct. to 18 Oct. (day of year 275 to 291). Hydrodynamic forcing was measured at S1 using a downward looking high resolution acoustic Doppler current profiler (ADCP) positioned 0.4 m above the seabed and burst sampled for 20 minutes every hour at 4 Hz, and at S2 using an acoustic Doppler velocimeter (ADV) positioned 1 m above the seabed and burst sampled for 20 minutes every hour at 64 Hz (Figure 3.1b). The mean lower low water depth at S1 was -1.0 m NAP (Normaal Amsterdam Peil, approximately mean sea level) and at S2 was -1.7 m NAP and the median sediment grain size at both sites was 350 μm. The tidal range was approximately 1.5 m. Large scale bathymetry was measured with an echo sounder during regular jet ski surveys. The large scale coordinate system used throughout this paper is with respect to degrees from shore-normal, with 0° being onshore (-x), +90° rotating counterclockwise from shore normal, and -90° rotating clockwise from shore normal.

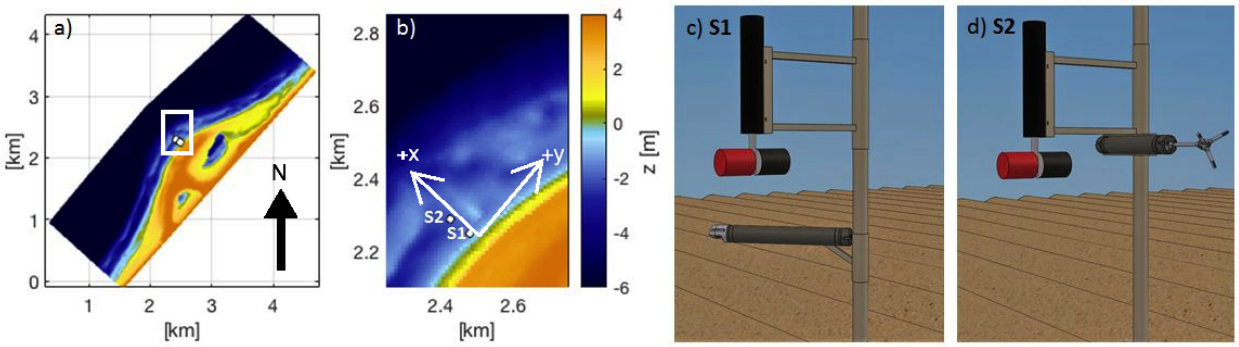

Figure 3.1: a) September 2014 bathymetry of Sand Engine mega-nourishment, Delfland, The Netherlands. b) Inset marked on panel a shows the sampling locations S1 and S2 indicated with white circles. Site S1 is close to the shoreline, and site S2 is close to the shore-parallel sandbar. The coordinate system used in this research is defined relative to the low tide shoreline, where shore parallel (alongshore) is y with +y being toward the Northeast, and shore normal (cross shore) is x with +x directed offshore. c) and d) Instrument array. Station S1 included an Imagenex 881a pencil beam sonar located 0.7 m from the bed and an ADCP located 0.4 m from the bed, and station S2 included an Imagenex 881a pencil beam sonar 1 m from the bed and an ADV 1 m from the bed.

3.3.2 Hydrodynamics

The local flow at each monitoring station was decomposed into current velocities, with magnitude U and direction ϕ_c, and wave orbital velocities, with magnitude u_o and direction ϕ_w, over 10 minute averaged time intervals. The current velocity is defined by,

$$U = |\overline{u}|, \tag{3.1}$$

where, u is the resultant of the horizontal flow velocity vectors, $\boldsymbol{u}$ and $\boldsymbol{v}$. And the orbital velocity,

$$u_o = \sqrt{2} u_{std}, \tag{3.2}$$

where, $u_{std} = \overline{[(u-U)^2]^{0.5}}$ (Traykovski et al., 1999). The wave period is defined with,

$$T = \frac{2\pi}{S_{m_2}/S_{m_1}}, \tag{3.3}$$

where, S is the spectra of the pressure signal, and the subscripts m_1 and m_2 refer to the first (mean) and second (variance) moments of the spectra (Madsen et al., 1988). The wave orbital diameter was defined with

$$d_o = 2\frac{u_o}{2\pi/T}. \tag{3.4}$$

The combined wave current velocity (Lacy et al., 2007) relates the wave orbital and current velocities with a third term representing the combined effect depending on the angle between the orbital and current velocities, where

$$u_{wc} = [u_o^2 + U^2 + 2u_o U \cos|\phi_w - \phi_c|]^{0.5}. \tag{3.5}$$

Finally, the kinetic energy in the combined wave-current flows is defined as

$$E_{k_{wc}} = \frac{1}{2} u_{wc}^2. \tag{3.6}$$

We distinguish in our observations between wave dominant, current dominant and combined flow conditions using a fraction of energy approach to assess the contribution of waves and/or currents to sediment flux. $E_{k_{wc}}$ is defined as the total kinetic energy in the flow field including both waves and currents. $E_{k_w}/E_{k_{wc}}$ is defined as the fraction of kinetic energy due to waves, so a value of 1 would be purely wave driven flow, and a value of 0 would be purely current driven flow. Previous literature has distinguished wave dominant flows from combined flows based on a ratio of wave induced to current induced friction velocity, where purely wave ripples occur at a friction velocity ratio of 0.5 or greater (Li and Amos, 1998; Lacy et al., 2007). To put this limit in terms of energy, this threshold of 0.5 is squared. Therefore we define, $E_{k_w}/E_{k_{wc}} > 0.75$ to be wave dominant, $0.75 \geq E_{k_w}/E_{k_{wc}} \geq 0.25$ for combined wave-current flow, and $0.25 > E_{k_w}/E_{k_{wc}}$ to be current dominant. An energy approach is used instead of the friction velocity since is it fairly difficult to estimate the friction velocity in combined flow conditions, so using energy mitigates propagation of error through analysis. Additionally, the flow energy was either measured or using linear wave theory for the wave contribution and a log layer approximation for the mean flow contribution, attenuated through the water column to be estimated approximately 10 cm above the crest of the bedforms.

3.3.3 Measured Bedform Statistics

Statistics of bedform wavelength (λ), bedform height (η), and bedform orientation (ϕ_r) are determined through analysis of sonar return data. Bottom position within each sonar dataset was found by identifying the high intensity return region for each sonar ping using two methods. The first is a weighted mean sum (WMS) method and the second is a bearing direction indicator (BDI) method (SeaBeam, 2000). WMS applies a weighted mean sum to each sonar ping, where the location of the highest WMS for each beam is the location of the bed, this method works well for return data with high grazing angles (data within 30° of the sonar nadir). The BDI applies a parabolic fit to the high intensity return for all the

beams intersecting the same section of bed within one sweep over multiple pings, the BDI method is suited to intensity returns at low grazing angles since the multiple ping fit gives higher confidence in the bed location. WMS was used to detect the bed within the inner 1 m diameter at bed level and BDI was used to detect the bed from the 1 m diameter range to the sonar sampling extent at bed level (see Wengrove et al. (2017) for more detail).

With a time series of 2D local bathymetries (Figures 3.2f-h and 3.3f-h), the dominant ripple wavelengths, heights, and orientations were determined with normalized 2D spatial wavenumber spectral analysis (Maier and Hay, 2009; Becker et al., 2007). The 2D spatial spectra, S (m^3), have axes of wavenumber, k_x (cross shore) and k_y (alongshore) (1/m). The spectra were normalized by premultiplying S by the wavenumber k_x and k_y, where $\hat{S} = Sk_xk_y$ (Alamo and Jimenez, 2003). The benefit of a normalized spectra is that the multiplication by wavenumber essentially whitens the spectra and enhances the dominant energy peaks for analysis. The energy distribution of the dominant peaks in the spectra indicate the dominant bedform wave number and orientation. Bedform height can be found by integrating the spectrum, analogous to a significant ocean wave height calculation from temporal spectral analysis (Traykovski, 2007; Penko et al., 2017) (see (Wengrove et al., 2017) for more detail). The bedform wavelength is defined as bedform-normal distance from crest to crest, and the bedform height is defined as vertical distance between bedform trough and crest.

The uncertainty associated with the spatial resolution of the pencil beam sonar measurements were related to range resolution, beam width, and sweep and rotation step angles. During the course of the experiment the water temperature stayed relatively constant with time, a sound speed of 1502 m/s was used to convert sonar time returns into range estimates. The range resolution of the pencil beam is 2 mm for a sampling range of 1 m to 4 m. The beam width operating at 1 MHz is 1.4° conical beam, so 1 m away from the transducer (within 30° of the sonar nadir) the resolution limit is 2.5 cm, while at the profiling extent or approximately 2 m way from the transducer, the resolution limit becomes 5.0 cm. Finally,

with respect to spatial sampling step angle, for S1, directly under the sonar the spatial resolution was 2 cm x 4 cm and at the profiling extent the spatial resolution was 5 cm x 8 cm. For S2, directly under the sonar the spatial resolution was 2 cm x 2 cm and at the profiling extent the spatial resolution was 5 cm x 5 cm. With these limitations, the smallest bedform wavelength that could be resolved within the inner 30° of the sonar nadir was approximately 12 cm, and at the profiling extent was approximately 25 cm. However, bedform height, could be resolved within 2 cm.

Uncertainties associated with the temporal resolution of the bedform migration involve the timescale for the sonar sensor rotations. Bedload sediment transport processes with a time scale less than a full sweep-rotation time window were not resolved; for S1 this was 10 minutes and for S2 this was 15 minutes. Additionally, processes that occured with a time scale of less than the time between subsequent sonar scans, dt, were not resolved, this was 20 minutes for S1 and 2 hours for S2. However, the low noise floor of the spectra of the time series of observed bedform wavelengths over the month long deployment at S1 showed that there were no sign of aliasing with a dt of 20 minutes (not shown), but this was not the case at S2 with a dt of 2 hours.

3.3.4 Sediment Continuity Equation

If we assume a function for transport,

$$\mathbf{q}_b = q_b \cos(\omega t - k x_b - k\delta_{x_b}), \tag{3.7}$$

where $\mathbf{q}_b$ is the bedload sediment flux [$m^3/m/s$], q_b is the scalar transport, ω is the angular frequency, k is the bedform wave number, δ_{x_b} is the phase offset between the bedform shape and the function for transport, x_b is the direction normal to the bedform crest, and t is time. Additionally, we assume the bed level can be descried by,

$$z_b(x_b, t) = \eta \cos(\omega t - k x_b). \tag{3.8}$$

where, z_b is the bed level and η is the bedform height.

The sediment continuity equation, or the Exner equation, relates the sediment flux gradient per unit width to the rate of bed level change (Nielsen, 1992), and is commonly expressed with

$$-n\frac{dz_b}{dt} \equiv \frac{dq}{dx_b}, \tag{3.9}$$

where, n is the sediment packing (~ 0.7 for sand). For the case of bedform migration or transformation with no local accretion or erosion, the bed elevation, z_b, can be expressed by the local bedform geometry ($z_b = \eta$). By substituting (3.7) and (3.8) into (3.9) the q_b can be expressed as a function of the rate of bedform migration,

$$\frac{q_b}{\cos(k\delta_{x_b})} = nV_{mig}\eta, \tag{3.10}$$

where $\boldsymbol{V}_{mig}$ is the migration rate, or the rate of growth or decay of the bedform,

$$\frac{q_b}{\sin(k\delta_{x_b})} = \frac{n}{k}\frac{\partial\eta}{\partial t}, \tag{3.11}$$

where $\frac{\partial\eta}{\partial t}$ is the bedform growth or decay (Nielsen, 1992). Both (3.10) and (3.11) are theoretically equivalent, and by substituting them into each other, an expression for δ_{x_b}/λ is described by,

$$\delta_{x_b}/\lambda = \frac{\tan^{-1}([\frac{\partial\hat{\eta}}{\partial t}/k]/[\eta V_{mig.}])}{2\pi}. \tag{3.12}$$

The bedform volumetric change as a function of sediment flux is found by rearranging (3.11), expanding the bedform growth term with the product rule, and defining $\frac{1}{2}n\frac{\partial\eta\lambda}{\partial t} = \frac{\partial Vol._b}{\partial t}$. By integrating the manipulation from $t-\tau$ to τ, an expression for the bedform volumetric change is given as

$$\Delta Vol._b - \int_{t-\tau}^{t} \frac{n}{2}\frac{\eta \partial \lambda}{\partial t} dt = \int_{t-\tau}^{t} \pi q_b \sin(2\pi \delta_{x_b}/\lambda) dt, \tag{3.13}$$

where, the first term, $\Delta Vol._b$, is the change in bedform volume over some time since it started to grow or decay, $\tau - t$, to the present time, t, the second term is related to the bedform stretching over time, and the third term is the portion of the time integrated sediment flux related to bedform growth or decay. The second term is 2% of the third term when the result is integrated over $\tau - t$, and so is considered to be negligible when interested in multi-ripple scale volumetric change, but may be important to the intra-ripple scale, so (3.13) becomes,

$$\Delta Vol._b = \int_{t-\tau}^{t} \pi q_b \sin(2\pi \delta_{x_b}/\lambda) dt. \tag{3.14}$$

3.3.5 Existing Time-Dependent Bedform Geometry Models

In laboratory settings Davis et al. (2004), Smith and Sleath (2005), Testik et al. (2005), and Doucette and O'Donoghue (2006) explored the time dependent nature of bedforms between equilibrium conditions, as well as the associated time scale for bedforms to reach an asymptotic equilibrium state with imposed wave forcing conditions. These studies give estimates for bedform temporal adjustment to equilibrium based on sediment transport rates, with each showing that it takes time for bedforms to evolve and grow between equilibrium states. In field settings, Traykovski (2007), Soulsby et al. (2012), and Nelson and Voulgaris (2015) also take a departure from equilibrium approach by relating a change in geometry over a period of time to a departure from equilibrium geometry model that imposes a parameterized time scale of change. Our effort further considers the wave-only spectral time dependent model of Traykovski (2007), and the wave or current dominant time dependent model of Soulsby et al. (2012); each summarized as follows:

Bedform evolution can be characterized with a time varying spectrum of bedform geometries defined by (Traykovski, 2007),

$$\frac{d\eta_{T07}(k)}{dt} = \frac{\eta_{eq}(k) - \eta_{T07}(k)}{T_{adj}(k)}, \tag{3.15}$$

where k is the associated bedform wavenumber ($2\pi/\lambda$), η_{eq} is the equilibrium ripple spectra modeled by a Gaussian distribution with inputs of a proposed equilibrium ripple height and ripple wavelength, and $T_{adj}(k)$ is an adjustment timescale for each wavenumber based on the wavenumber dependent cross sectional area of the bedform and the total bedform sediment flux, q (Meyer-Peter and Muller, 1948). A numerical integration scheme results in a time series of wavenumber dependent ripple heights, where modeled $\eta_{m_{T07}}$ is found by integrating with respect to wavenumber (analogous to a significant wave height calculation) as discussed previously, and modeled $\lambda_{m_{T07}}$ is defined by $2\pi/k$ of the peak spectral energy band for each time step. The model gives high skill predictions of ripple geometry in a predominantly wave environment, where the model skill is the correlation coefficient squared.

Soulsby et al. (2012) proposed a time-dependent bedform evolution model that uses a Shields parameter criterion to decide whether ripples are wave- or current- generated. A departure from equilibrium approach allows ripples to evolve based on an adjustment time scale. The model is defined by

$$\frac{dx_{SWM12}}{dt} = a(t) - b(t)x_{SWM12}(t), \tag{3.16}$$

where x_{SWM12} is either the modeled $\eta_{m_{SWM12}}$ or $\lambda_{m_{SWM12}}$ that is found through a numerical integration. Additionally, $a(t) = x_{eq}\beta/T_r$ and $b(t) = \beta/T_r + bio/T_b$, where x_{eq} is an equilibrium length and β is a rate of change parameter based on waves or current dominant forcing. T_r is a rate of change characteristic time scale that is equal to the wave period for wave forcing conditions and the time taken for an equilibrium ripple to be changed by the total bedload transport rate for current forcing. bio and T_b are a parameter and a time scale related to biological degradation of the bedforms. The model has high skill in prediction of wave dominant flow or current dominant flow bedforms of less than 0.5 m in wavelength;

however it does not predict megaripples and does not account for combined wave-current flows.

3.4 Results

3.4.1 Observations of Bedform Geometry

Time series of hydrodynamic and bedform geometry observations are shown in Figures 3.2 and 3.3 for S1 and S2, respectively. S1 was deployed for a spring-neap-spring-neap-spring tidal cycle, including 4 storm events (day of year 278, 280, 287, 294). S2 was deployed for a neap-spring-neap tidal cycle with 3 storm events (day of year 278, 280, 287). At both locations the currents were strongly tidally influenced with stronger currents during flood tide, as the tidal flow runs parallel to the Delfland coast. Additionally, wave orbital velocities were tidally modulated due to waves breaking on an shore-parallel sandbar during low water, and more shoreward during high water (see Figure 3.1).

Bedform geometry was observed to vary substantially at each station over the period of investigation with a clear dependence on the type of hydrodynamic forcing (Figures 3.2 and 3.3). The hydrodynamic kinetic energy shaded by the fraction of energy due to waves ($E_{k_w}/E_{k_{wc}}$) highlights occurrences of current dominated flows (low $E_{k_w}/E_{k_{wc}}$), and wave dominated flows (high $E_{k_w}/E_{k_{wc}}$). During non-storm conditions semidiurnal peaks in the energy were associated with the tide as evident with low $E_{k_w}/E_{k_{wc}}$. At S2 larger wavelength bedforms corresponded with instances of increased flow, and occurred generally under current or combined flow dominant kinetic energy. However, at S1 data showed that large wavelength bedforms can correspond with instances of large kinetic energy that was either current dominated or high wave energy dominated conditions (i.e. storms). Additionally, bedform steepness was generally characteristic of wave orbital ripple steepness ($\eta/\lambda \approx 0.16$) during wave energy dominated conditions, and dune steepness ($\eta/\lambda \approx 0.06$) during current energy dominated conditions (Wiberg and Harris, 1994; Fredsøe and Deigaard, 1992). Figure

3.4 shows a truncated time series from Figure 3.2 to highlight the growth of one bedform over time with corresponding sonar images to show bed change.

3.4.2 Bedform Characterization

The distribution of the relative frequency of occurrence during each deployment of λ, η, and η/λ (Figure 3.5a-c for each site S1 and S2) shows that smaller wavelength bedforms occurred more often, and generally bedforms were in the range of steepness of wave orbital ripples ($\eta/\lambda \approx 0.16$). However, the histogram of λ also shows that for each site, bedforms of wavelengths longer than 0.5 m occurred between 29-33% of the time, and bedforms with a steepness of less than that of wave orbital ripples occur approximately 29-35% of the time for each site. The observed bedforms were predominantly 2D, but during transition periods, bedforms became 3D; the degree of three dimensionality is shown through spread of dominant bedform orientation, as indicated with a shaded grey band (Figure 3.4).

Ripples observed in wave dominated environments are characterized as orbital ripples, suborbital ripples, and anorbital ripples (Clifton and Dingler, 1984; Wiberg and Harris, 1994). Where the wavelength of orbital ripples scales with the orbital excursion of the waves, anorbital ripples have a wavelength independent of orbital excursion and are thought to scale with the grain size, and suborbital ripples are some combination of the two regimes (Clifton and Dingler, 1984; Wiberg and Harris, 1994). The Clifton and Dingler (1984) classification diagram is shown as Figure 3.6a overlaid with observations from S1 and S2. The wave dominated bedforms, with large $E_{k_w}/E_{k_{wc}}$, generally were classified as orbital or slightly suborbital (falling on the dark grey bar in Figure 3.6a and are consistent with Clifton and Dingler (1984)). However, ripples with larger wavelengths correspond to periods with smaller $E_{k_w}/E_{k_{wc}}$ (Figure 3.6a blue shading) and fall in an unclassified region by Clifton and Dingler (1984). The unclassified bedforms did not show evidence of being relic (Figure 3.6a). Considering such attributes, we consider the bedforms that fall into this unclassified

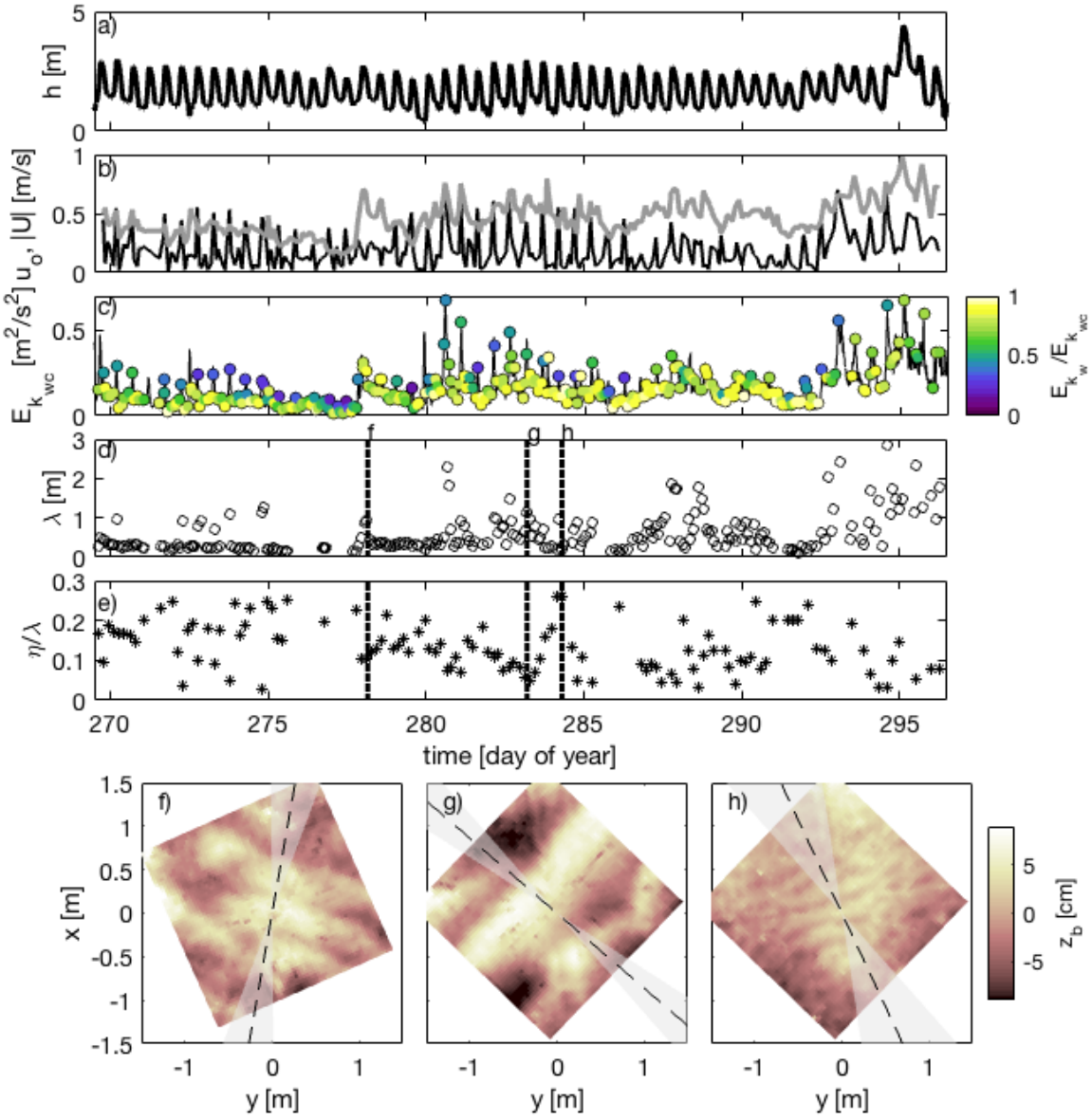

Figure 3.2: Time series of observations at S1, where panel a) shows depth (h), b) shows amplitude of wave orbital velocity, u_o, in grey and mean velocity, U, in black, c) shows total kinetic energy, E_{kwc} shaded by fraction of kinetic energy due to waves, d) shows ripple wavelength, λ, e) and shows ripple steepness, η/λ. The vertical dashed lines in panels d and e indicate occurrences of local bathymetries shown as panels f-h. Panels f-h) show 2D bathymetries, where y is shore parallel, and x is shore-normal, with -x directed onshore, and is shaded by bedform height. Finally, dashed lines and shaded overlay in panels f-h indicate bedform orientation and orientation uncertainty, respectively.

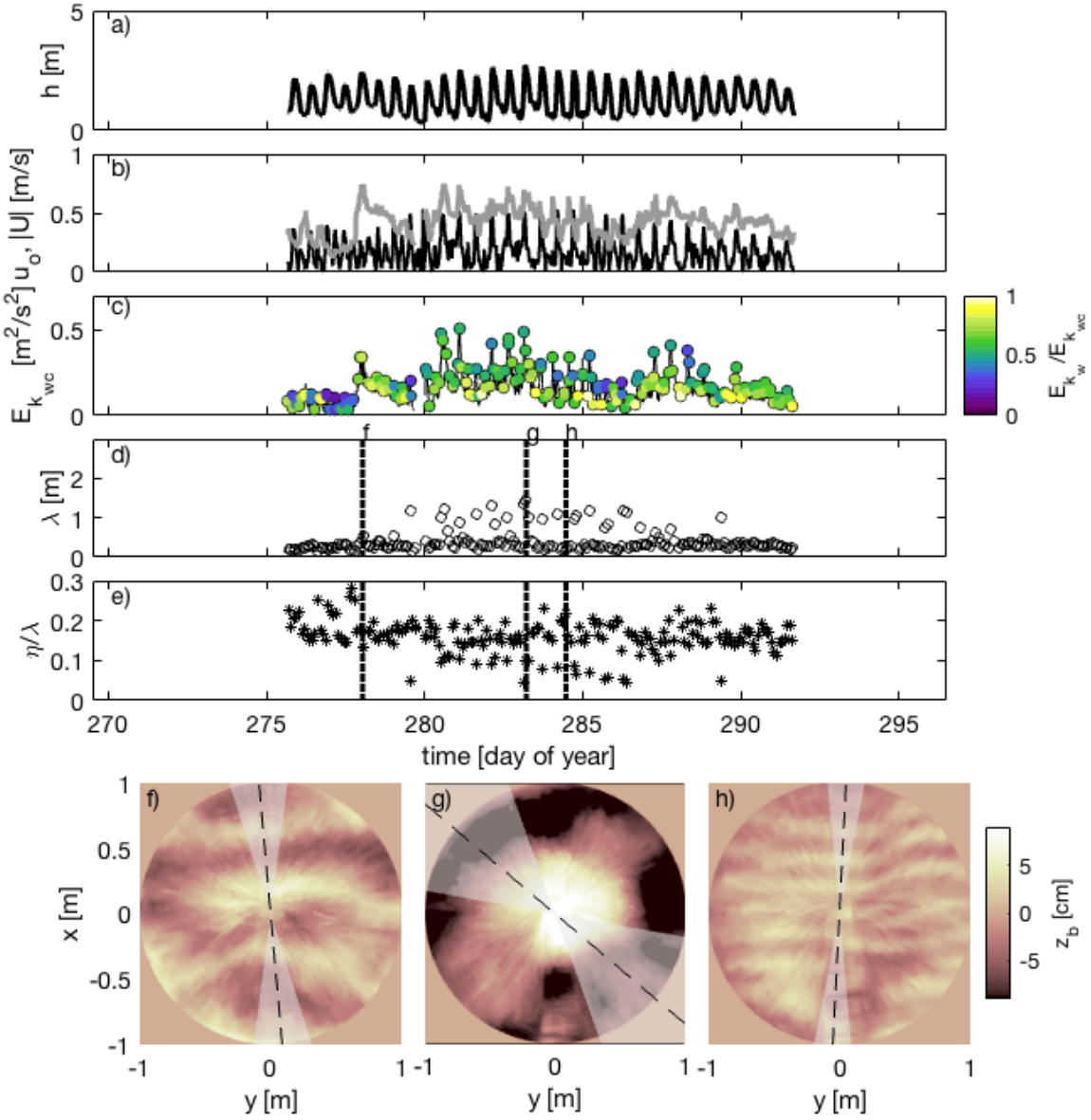

Figure 3.3: Time series of observations at S2, where panel a) shows depth (h), b) shows amplitude of wave orbital velocity, u_o, in grey and mean velocity, U, in black, c) shows total kinetic energy, $E_{k_{wc}}$ shaded by fraction of kinetic energy due to waves, d) shows ripple wavelength, λ, e) and shows ripple steepness, η/λ. The vertical dashed lines in panels d and e indicate occurrences of local bathymetries shown as panels f-h. Panels f-h) show 2D bathymetries, where y is shore parallel, and x is shore-normal, with -x directed onshore, and is shaded by bedform height. Finally, dashed lines and shaded overlay in panels f-h indicate bedform orientation and orientation uncertainty, respectively.

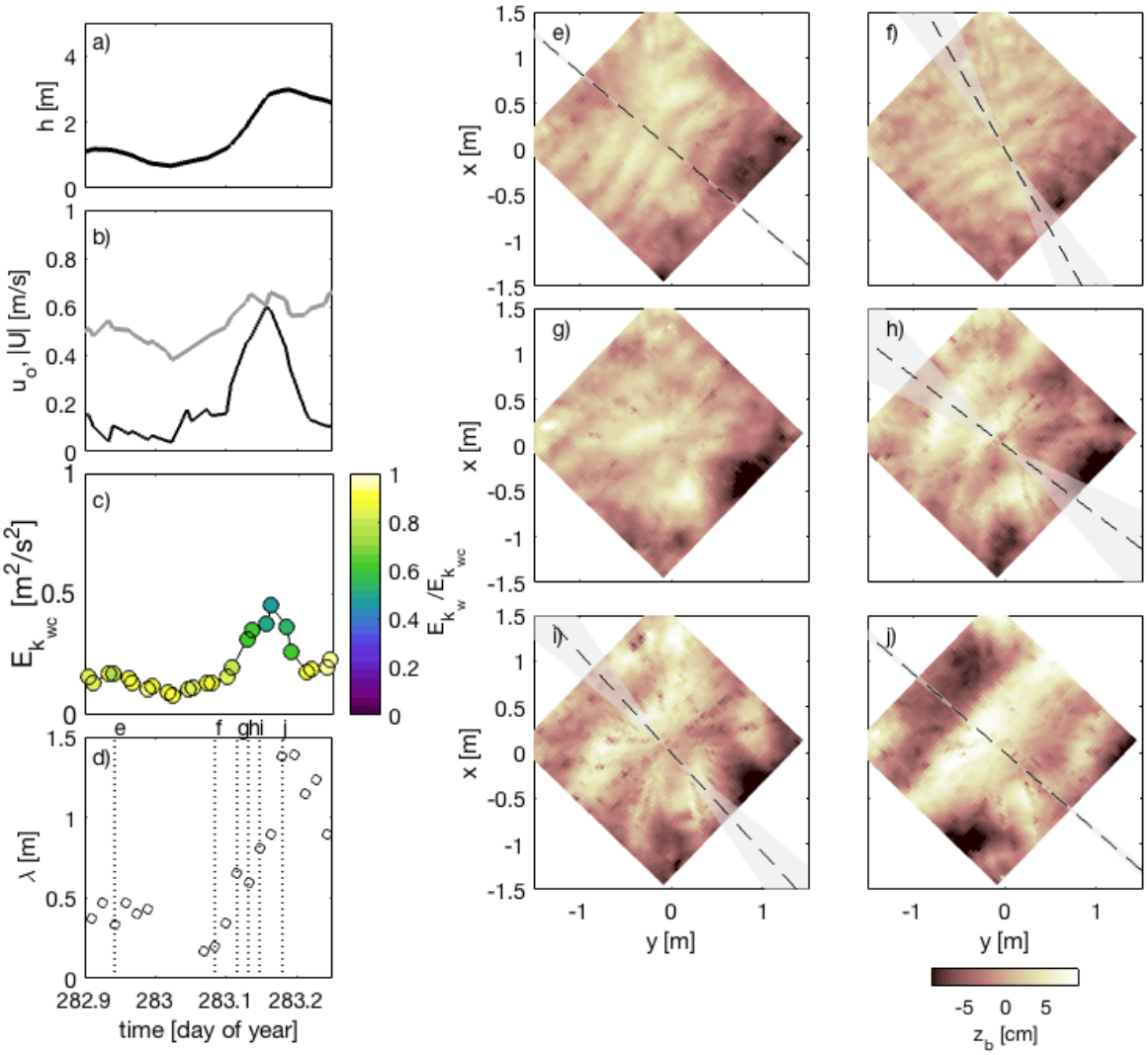

Figure 3.4: Time series of observations at S1 for one tidal cycle, where panel a) shows depth (h), b) shows amplitude of wave orbital velocity, u_o, in grey and mean velocity, U, in black, c) shows total kinetic energy, $E_{k_{wc}}$ shaded by fraction of kinetic energy due to waves, and d) shows ripple wavelength, λ. The vertical dashed lines in panel d indicate occurrences of local bathymetries shown as panels e-j. Panels e-j) show 2D bathymetries, where y is shore parallel, and x is shore-normal, with -x directed onshore, and is shaded by bedform height. Finally, dashed lines and shaded overlay in e-j indicate bedform orientation and orientation uncertainty, respectively.

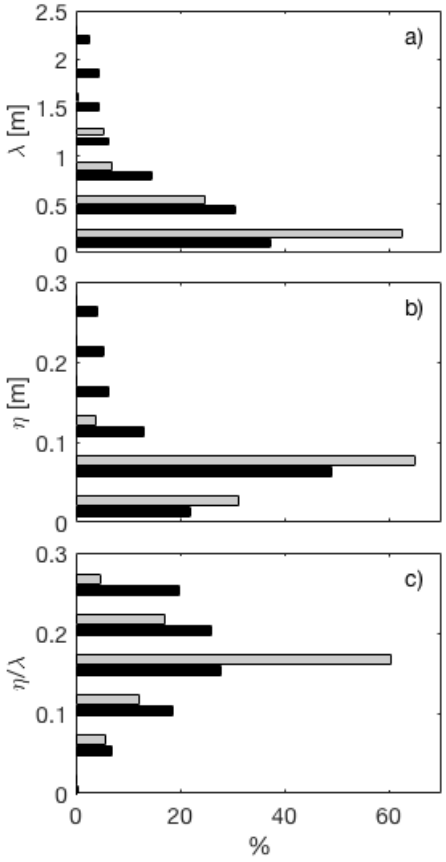

Figure 3.5: Histograms of bedform a) wavelength (λ), b) amplitude (η), and c) steepness (η/λ) at both stations, where S1 is in black and S2 is in grey.

region by Clifton and Dingler (1984) as either combined wave-current or current dominant bedforms and were formed by the onset of strong currents.

Figure 3.6b shows the distribution of observed bedform wavelength as a function of wavelength, $E_{k_w}/E_{k_{wc}}$, u_o, and U for both S1 and S2 sites. S1 and S2 were influenced strongly by tidal currents particularly with the occurrence of large U at relatively small u_o, when wave-driven alongshore currents were weak (see Hay and Mudge (2005) Figure 11 for a reference case with small tidal currents). Additionally, larger wavelength bedforms were shown to occur with large $\boldsymbol{u_o}$ and/or large $\boldsymbol{U}$, indicating that bedforms may have been formed by waves, currents, and with combined wave-current forcing contributions, shown by the shading of $E_{k_w}/E_{k_{wc}}$.

3.4.3 Observations of Bedform Orientation

The bedforms at S1 and S2 were very dynamic, and during transitional periods they were not aligned and orient over a range of directions between 5° and 90°. The bandwidth range was determined by the spacing between peaks in 2D spatial spectra with the same wavenumber, and is indicated by a shaded grey band in Figure 3.7 and a shaded grey band on each 2D bathymetry plot (Figures 3.2-3.4). The bedforms generally did not align with the current or the wave direction, but rather a combination of both depending on flow dominance. The bedforms sometimes align with the wave direction when $E_{k_w}/E_{k_{wc}}$ was large, notably during low tide, and with the current direction when $E_{k_w}/E_{k_{wc}}$ was small (Figure 3.7b, c). However, the bedforms did not always align with the dominant flow direction (e.g. Figure 3.7b and c day of year 281.2).

Figure 3.8 shows the bedform orientation in relation to the current magnitude and direction, the wave orbital magnitude and direction, the bedform wavelength, and $E_{k_w}/E_{k_{wc}}$. The strongest correlation between the four metrics displayed is the bedform orientation in relation to the current magnitude (panel a). It is clear that as bedforms became more current influenced (low $E_{k_w}/E_{k_{wc}}$) they not only got larger in wavelength, but the bedforms tended

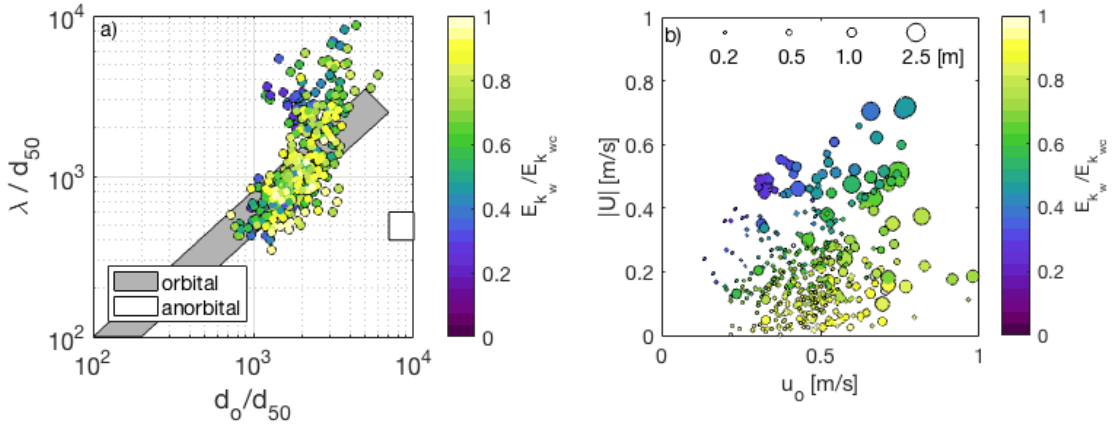

Figure 3.6: Bedform classification scatter plot diagrams. Panel a) shows the Clifton and Dingler (1984) classification diagram (dark gray are classified as orbital ripples and white as anorbital ripples, with the region in-between classified as suborbital ripples) overlaid with observations from S1 and S2, shaded by fraction of kinetic energy due to waves. Panel b) shows the distribution of observed bedform wavelengths based on orbital velocity and current velocity flow contributions, shaded by fraction of energy due to waves, where the marker size indicates bedform wavelength (with larger markers indicating larger λ as shown at the top of the panel).

to orient between 30° and 70°, which was approaching the direction of the prevailing flood tidal currents oriented toward the northeast (90° counterclockwise from shore-normal in Figure 3.1). However, the bedform orientation in relation to the orbital velocity magnitude did not show a clear trend (panel c), indicating that the magnitude of the waves alone did not have a large effect on bedform orientation.

When considering the bedform orientation in relation to the current and wave directions (Figure 3.8b, d), the bedforms generally did not align with either the current or wave direction. A $rmse_{range}$ error analysis is used to determine how well the bedform orientation observations fit the wave and current directions. The metric is a modified $rmse$ calculation, where the difference between the measured and modeled orientations are set to zero if the wave or current direction falls anywhere within the bedform orientation bandwidth range, and the differences are calculated to the center of the range if the wave or current direction falls outside. Additionally, circular statistics were used to calculate the $rmse_{range}$. The bedform orientation $rmse_{range}$ statistics (given in the caption of Figure 3.8) show that the bedform orientation was neither predominantly influenced by waves or currents; however, the $rmse_{range}$ with respect to wave direction was almost 1/2 of $rmse_{range}$ with respect to the current direction. Although not reflected in the $rmse_{range}$ calculation, there was also a qualitative trend with combined flow and current dominated bedforms (3.8b), where the bedforms with an $E_{k_w}/E_{k_{wc}} < 0.75$ tend to lie closer to the 1:1 line than the wave dominated bedforms, possibly indicating that the current dominated and combined flow bedform directions were influenced by the current direction, especially evident with larger wavelength bedforms. Overall, the generally large $rmse_{range}$ values indicate that the bedform orientation was not a function of the independent wave and current directions alone, but rather a concurrent combination (consistent with Gallagher et al. (1998) and Lacy et al. (2007)).

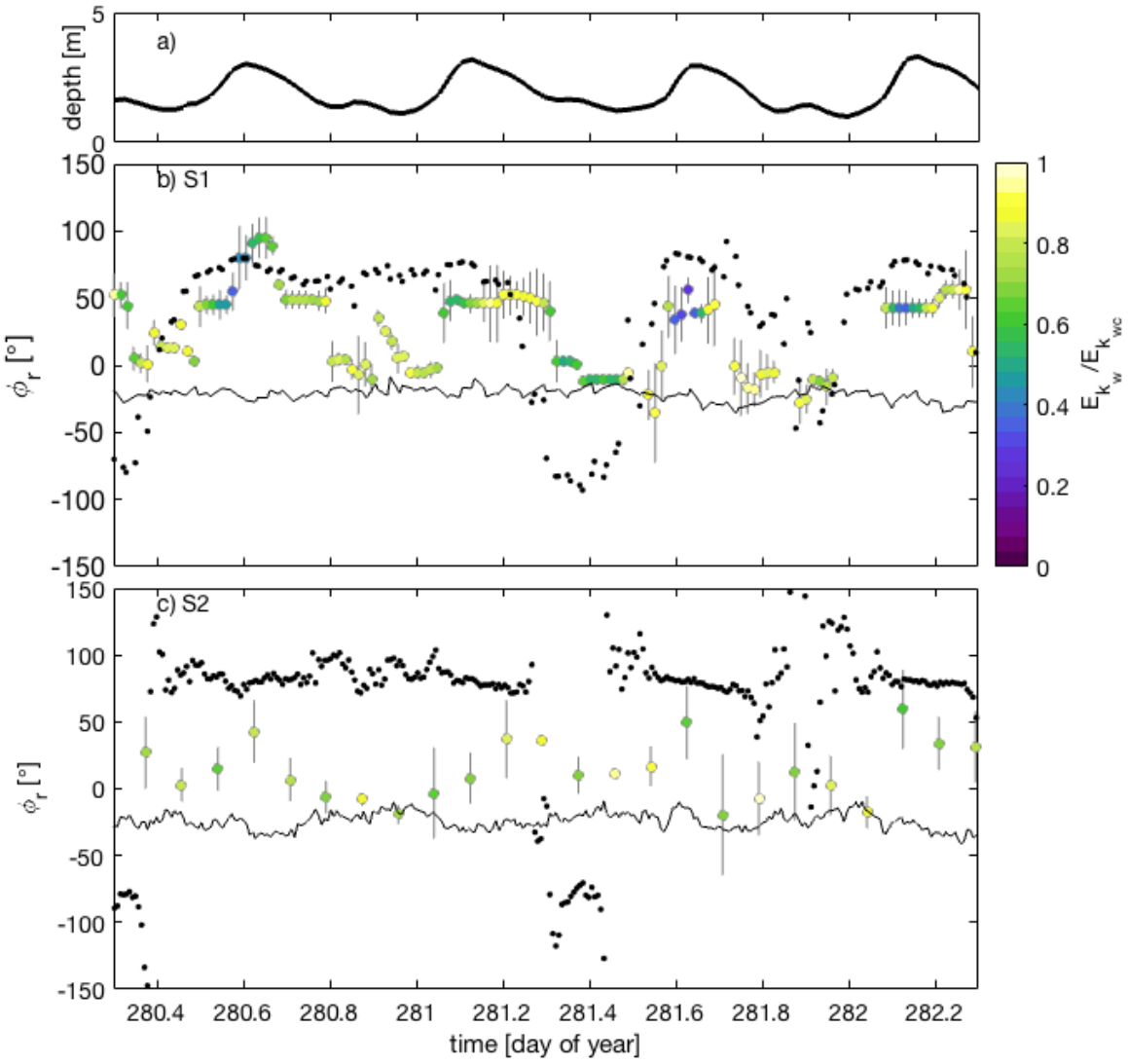

Figure 3.7: Observed bedform direction and concurrent flow directions. Panel a) shows a time series of depth at S1. Panel b) S1 and c) S2, show time series of range of observed bedform orientation colored by fraction of kinetic energy due to waves (circles with range bars), observed current direction (black dots), and observed wave direction (thin black line).

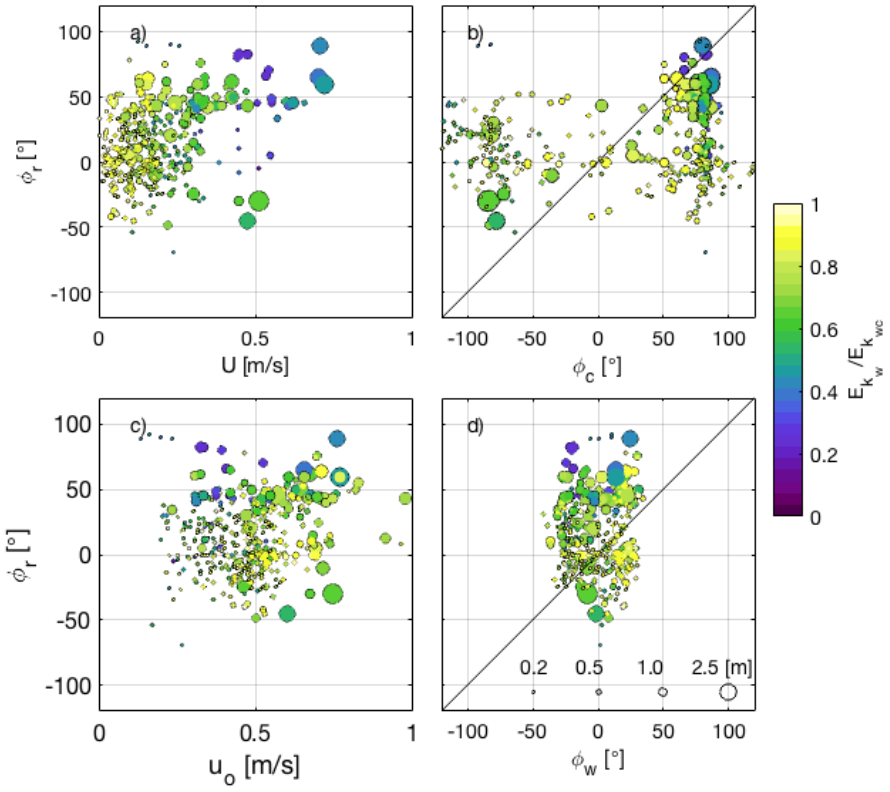

Figure 3.8: Observed bedform directions plotted against a) current magnitude, b) current direction [$rmse_{range} = 40°$, c) wave orbital magnitude, d) wave orbital direction [$rmse_{range} = 23°$. *rmse* is calculated between the observed bedform range and the model as described in the text. Markers are colored by the fraction kinetic of energy due to waves and the size of the marker scales with the bedform wavelength as indicated in the bottom of panel d.

3.5 Discussion

3.5.1 Time-evolving Bedform Geometry and the Sediment Continuity Equation

The relationship between hydrodynamic forcing and bedform wavelength over one tidal cycle is shown in Figure 3.4. The bedform wavelength grew with increased duration of forcing, especially with respect to combined wave-current bedforms; demonstrating that λ at any instance in time was not only dependent on the present hydrodynamic forcing, but also on past hydrodynamic conditions over some lag time, τ.

The bedform will grow/decay and/or migrate based upon the position of peak transport with respect to the bedform crest. When the non-dimensional phase offset, δ_{x_b}/λ, is 0.25 the bedform will only grow, when δ_{x_b}/λ is 0 the bedform will only migrate, and when δ_{x_b}/λ is -0.25 the bedform will only decay. The bedform wavelength begins to increase with the onset of increases in $E_{k_{wc}}$ and during this periods the bedform grows and migrates, but when the bedform growth dominates δ_{x_b}/λ will be large, and when bedform migration dominates δ_{x_b}/λ will be close to zero (Figure 3.9 and Figure 3.10). Generally, the largest periods of bedform growth or decay have small migrations, and the largest periods of migration have small growth or decay (Figure 3.10). The sediment transport grows with either increased migration or increased growth, and decays with decreased migration or decay in bedform volume, additionally, q_b can be estimated from either (3.10) and (3.11) and give similar magnitudes (Figure 3.9e).

The results of the continuity analysis given by (3.14) are shown as Figure 3.11 and 3.12. Figure 3.11 shows the observed change in bedform volume and the integral of the sediment flux term calculated using (3.10) with three different methods to estimate the lag time for bedform growth, τ. The bedform volume was calculated by taking the average cross section of the ripple profile in the direction of the bedform orientation and then used the measured ripple wavelength from the 2D spectra to find the mean bedform volume for each time step.

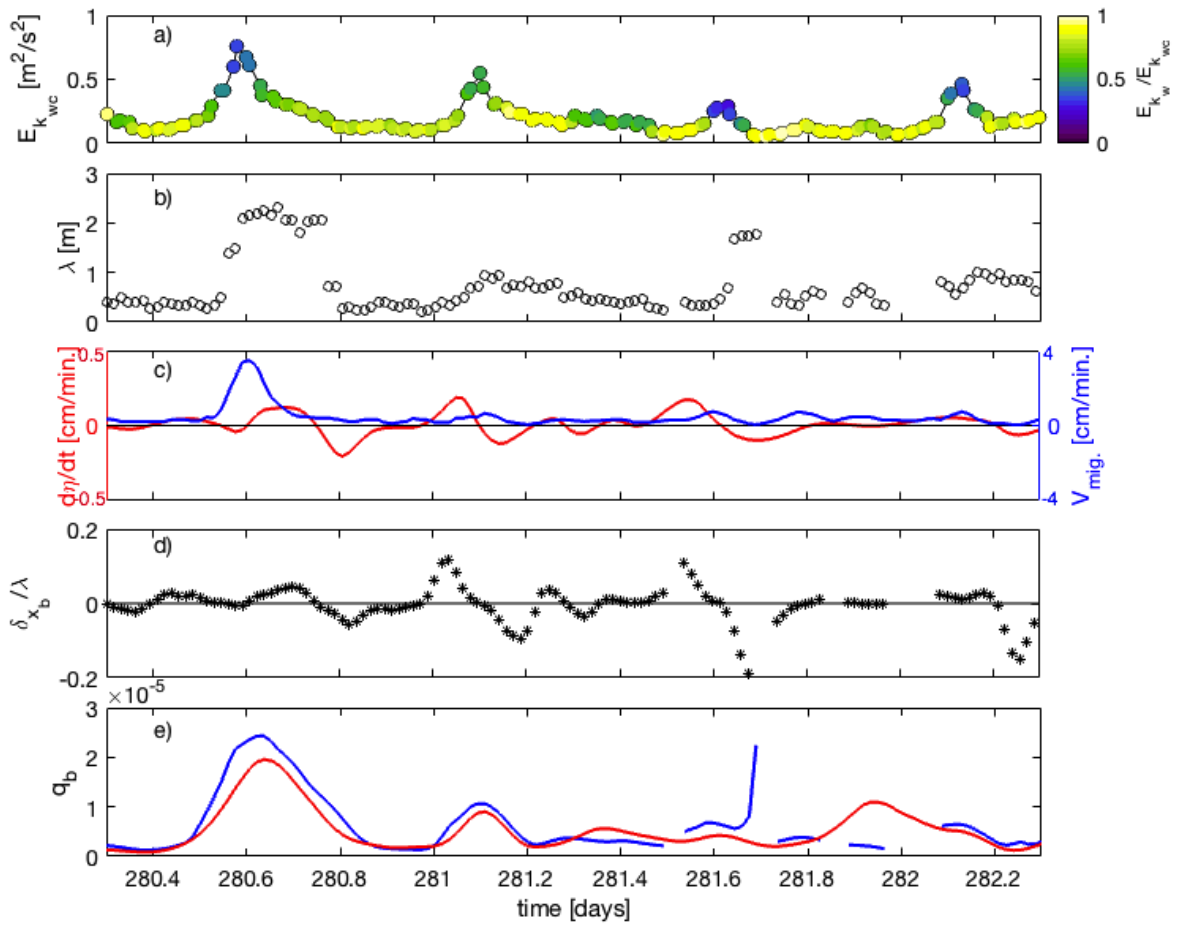

Figure 3.9: Time series of indicators for bedform growth, decay, and migration. Panel a) shows the wave-current energy time series colored by fraction of kinetic energy due to waves at S1. Panel b) shows a short time series of bedform wave length. Panel c) shows the bedform growth/decay rate in red and the bedform migration rate in blue. Panel c) shows the non-dimensional phase offset between the sediment transport and bed shape, when δ_{x_b}/λ is positive the bedform will grow, negative will decay, and 0 will migrate. Panel e) shows the bedload sediment transport estimated with equations (3.10) (blue) and (3.11) (red).

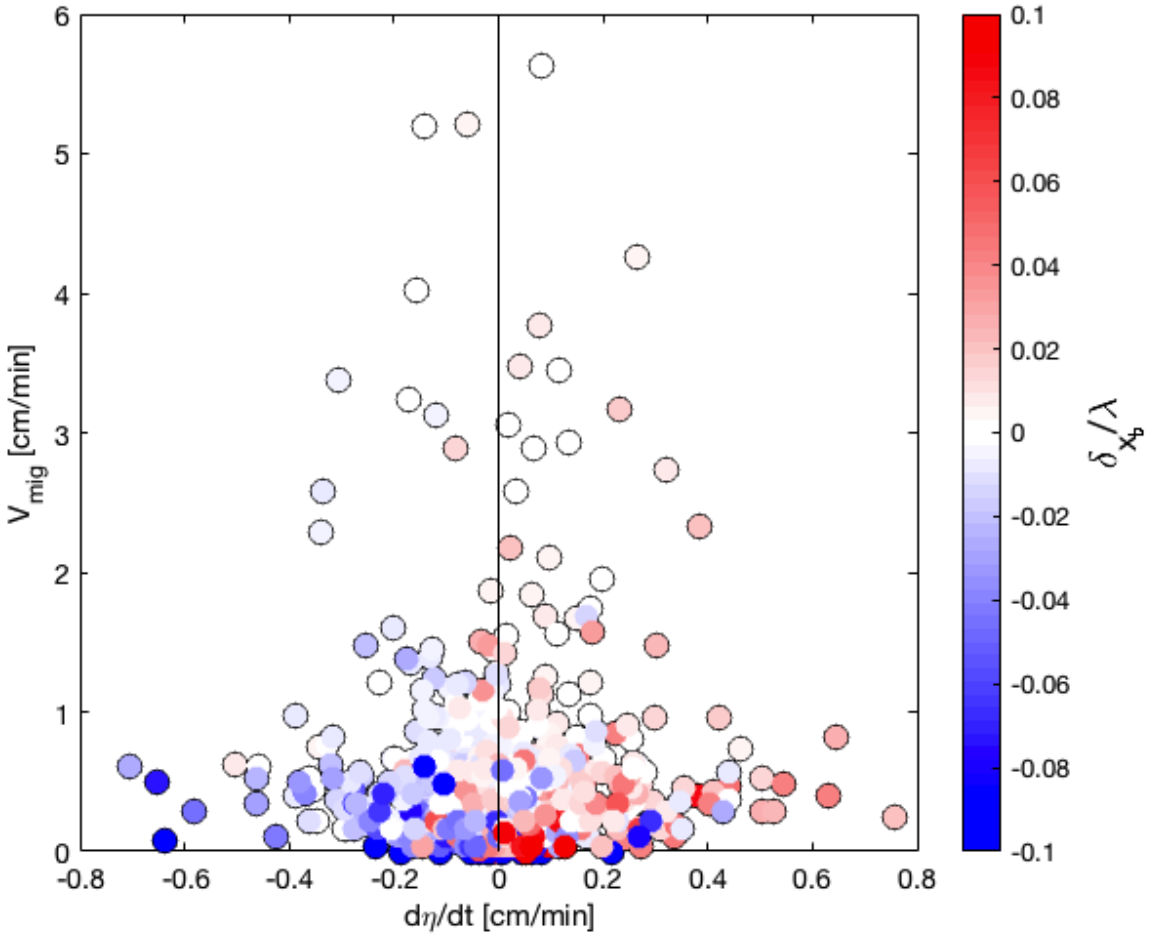

Figure 3.10: Scatter plot of bedform growth/decay and migration rate, colored by the non-dimensional phase offset between the sediment transport and bed shape, δ_{x_b} is estimated with (3.12). When δ_{x_b}/λ is positive the bedform will grow, negative will decay, and 0 will migrate.

To find τ, the first method sets $\tau = dt$, or one sample time step (for S1 dt = 20 min. and for S2 dt = 2 hr.; denoted τ dt in Figures 3.11 and 3.12). The second method sets $\tau = \tau_{zerocrossing}$, or the adjustment time found with observations of bedform growth or decay by the time between subsequent upward and downward zero crossings in $dVol._b/dt$. An upward zero crossing indicates the initiation of bedform growth, and a downward zero crossing indicates the start of bedform decay. If the bedform reaches an equilibrium condition with the flow, and stops growing, or it begins to relax to scale with a different flow field (stops growing or starts decaying), the lag time was set to dt. An example of an individual bedform growing over time at S1 is shown in Figure 3.4, in this case the maximum bedform lag time, τ_{max}, was approximately 2.4 hours or 0.1 days. The observed bedform adjustment times using this method showed that within wave dominant conditions, the bedform adjustment time was fairly quick, within 20 minutes to 1 hour the bedforms began to come into equilibrium with the flow field; however, with the addition of currents, the adjustment time became much longer, approximately 2.5 hours to 6 hours and the bedforms may have never adjusted into equilibrium with the flow forcing. The third method to find τ uses $\tau = \frac{n\eta\lambda}{2q_b}$ (Traykovski, 2007). The method assumes that the sediment flux during bedform growth is uniform with respect to time. Since (3.14) estimates the change in bedform volume as a function of the sediment transport, it is viable even through quiescent conditions, but with the dynamic qualities of these data, this is untested.

Observations captured many instances of bedform building and decay over time (e.g. Figure 3.4). When $\tau = dt$ (3.14) greatly underestimates the change in bedform volume, especially for S1 where dt is much shorter (Figure 3.11 and 3.12); especially apparent during instances of increased changes in bedform volume, which suggests bedform building or decay is a time dependent process. Additionally, at S1, τ was estimated using the bedform zero-crossing method and at S1 and S2 τ was estimated using the expression for τ in from Traykovski (2007). However, at S2, the bedform zero-crossing method could not be used

because the sampling rate between subsequent sonar images was too slow to capture bedform building.

At both S1 and S2 it is clearly evident that (3.14) has higher skill using a variable τ. Figure 3.11b and Figure 3.12 demonstrates that τ estimated directly from the bedform zero-crossing method ($rmse = 0.02$ m^3, $r^2 = 0.40$ for S1) or calculated using $\tau = \frac{n\eta\lambda}{2q_b}$ ($rmse = 0.02$ m^3, $r^2 = 0.53$ for S1 and S2) represents the range of measured bedform volumes much better than $\tau = dt$ ($rmse = 0.04$ m^3, $r^2 = 0.23$ for S1 and S2). The potential for using the sediment continuity equation combined with a variable bedform adjustment time to analytically model time varying change in bedform volume (i.e. roughness) is a significant contribution of this effort. With increased understanding of the driving forces behind transitions in bedform growth/decay and migration (i.e. model for δ_{x_b}/λ), the volumetric growth and decay in morphology could be robustly modeled with skill within wave dominant, current dominant, and combined flow forcing.

3.5.2 Existing Time-Dependent Bedform Geometry Model Comparisons

Previous work primarily focuses on approximating bedform geometry (λ and η) from the overlying flow field instead of bedform volume ($Vol._b$) as was predicted with the sediment continuity equation in the previous section. In essence, bedform geometry is a broken down description of bedform volume. The leading time dependent bedform geometry models for prediction of bedform wavelength and height are Traykovski (2007) and Soulsby et al. (2012). Each model was evaluated using the data collected at S1 and S2 for both the entire dataset as well as a subset of the data that represents data with which the model was developed (Figure 3.13).

The Traykovski (2007) model is formulated for waves only, so with the smaller, orbital ripples, it performed with twice the r^2 and the model $rmse$ decreased by 2/3 or better for both λ and η, when compared with the full dataset, which includes combined flow and current generated bedforms (Figure 3.13a, c). However, the concept behind the adjustment

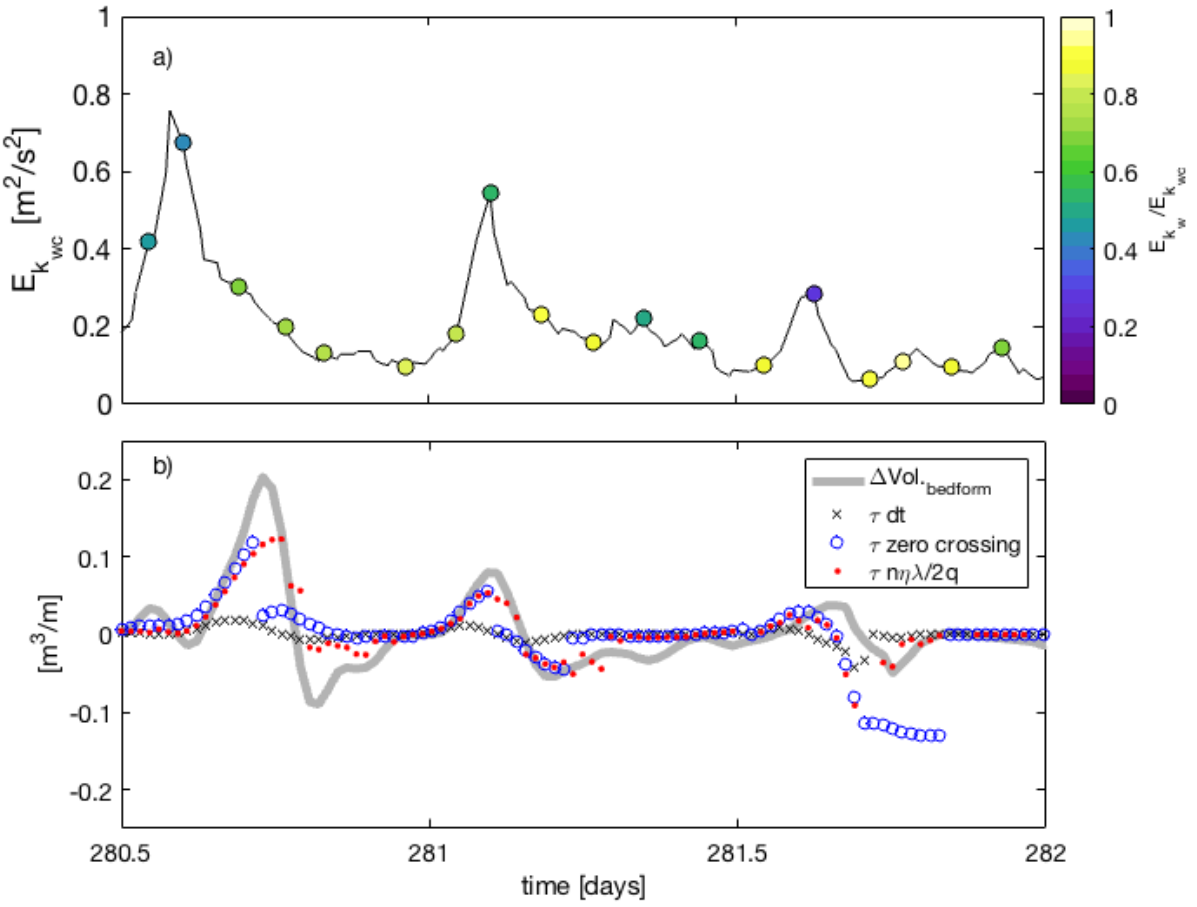

Figure 3.11: Time series of bedform volume represented by the sediment continuity equation. Panel a) shows the wave-current energy time series colored by fraction of kinetic energy due to waves at S1. Panel b) shows a short time series of $\Delta Vol._b$, where the thick grey line is the RHS of (3.14) and the markers represent the LHS of (3.14) using various approximations of the bedform lag time, τ, estimated as follows. The black $\times$ use a $\tau = dt$, the blue $\circ$ use a τ directly estimated from the bedform zero-crossing method, and the red $\bullet$ use a τ estimated from ($\tau = \frac{n\eta\lambda}{2q_b}$).

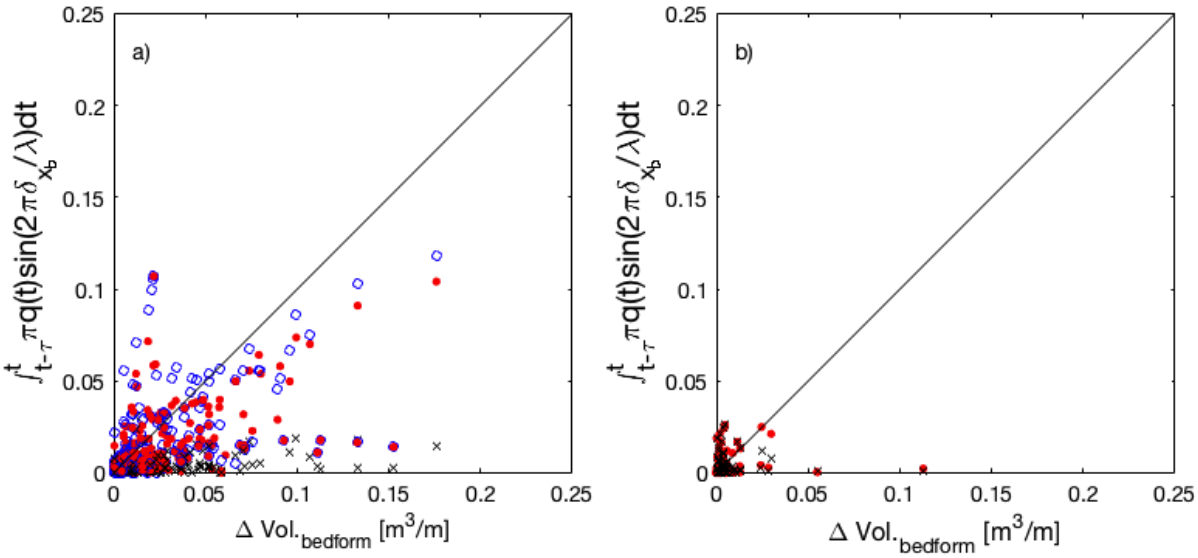

Figure 3.12: Scatter plot of the change in bedform unit volume vs. the time integrated transport (LHS vs. RHS of (3.14)) for the full data set collected at a) S1, and b) S2. The change in bedform volume (x axis) is plotted against the time integrated sediment flux using different approximations of the bedform lag time, τ (y axis). The black $\times$ use a $\tau = dt$, the blue $\circ$ use a τ directly estimated from the bedform zero-crossing method, and the red $\bullet$ use a τ estimated from ($\tau = \frac{n\eta\lambda}{2q_b}$). The solid black line is a 1 to 1 line.

timescale, T_{adj} of the Traykovski (2007) model is valid for both wave and current generated bedforms as shown in Figure 3.12.

The Soulsby et al. (2012) model is applicable to either wave or current generated bedforms, but it generally fails to predict megaripple scale bedforms. If the model is used to predict bedforms with wavelengths less than 0.5 m (regardless of flow dominance), the model r^2 stays the same, but the model $rmse$ decreases by 2/3 or better, suggesting a model bias. The Soulsby et al. (2012) model may poorly predict larger volume bedforms partially because it excludes the effects of combined flows that are prevalent at S1 and S2. Additionally, the estimated equilibrium bedform geometry model used by Soulsby et al. (2012) considerably under-predicts ($\lambda_{eq} \sim 0.3$ m) the observed bedform wavelengths (λ = 1-2.5 m) during combined flows. Finally, in Soulsby et al. (2012) the criterion distinguishing between wave or current generated bedforms is based on the Shields parameter, and depending on the approximation used for bed stress, under predicted mobility during combined flow conditions at the S1 and S2 sites.

The adjustment characteristic to an equilibrium length scale in Traykovski (2007) and Soulsby et al. (2012) seems reasonable; however, in practice may hinder the model skill (especially during combined flow conditions). The equilibrium geometry parameterizations may not be appropriate to all bedform generation conditions, especially combined wave-current bedforms. Additionally, the transition from wave generated to current generated is abrupt in the Soulsby et al. (2012) model, and does not allow for combined flow bedform generation.

Although these models have some limitations, their incorporation of time dependent growth is relevant to bedform building, even in combined wave-current flows. Most bedforms in our dataset never actually came into complete equilibrium with the flow forcing, with the exclusion of wave dominated bedforms. The departure from equilibrium theory could be an explanation for the inability for bedform geometry models such as Traykovski (2007) and Soulsby et al. (2012) to predict bedform wavelength and height in combined flows.

Although both of these models are time dependent, they also are based on an equilibrium approach. Equilibrium theory may not be representative of the physics of combined flow bedform growth, or at least, present equilibrium theory may not be consistent with the stability condition of combined wave-current bedforms.

3.6 Conclusions

Observations of bedform response to wave, current, and high energy combined wave-current dominant flows are presented. The observations may be one of the only datasets that capture both ripple and megaripple response to hydrodynamic conditions consisting of wave forcing plus strong currents (>0.5 m/s) collected within and near the surf zone. Dynamic bedform geometry transitions in response to shifts in flow conditions are resolved, and observations also show that bedform volume - when exposed to current and combined wave-current forcing - continuously build until the flow changes.

Bedform transformation and growth are shown to be a highly time dependent sediment transport process. With hydrodynamic transitions, the bedform scaling did not respond immediately; instead, the bedform adjustment lagged behind in response to the new forcing condition. Within wave dominant conditions, the bedform adjustment time was fairly quick; within 20 minutes to 1 hour the bedforms began to come into equilibrium with the flow field. However, when strong currents were present, the adjustment time became much longer, ranging between 2.5 hours to 6 hours and the bedforms never actually came into complete equilibrium with the flow forcing. The departure from equilibrium conditions captured in this dataset may be responsible for the inability for existing bedform geometry models to predict bedform wavelength and height in the measured combined flows. Demonstrating that current equilibrium theory may not be representative of combined flow bedform growth or, at least not consistent with the stability condition for combined wave-current bedforms.

Aside from our dynamic set of observations of bedform response to combined wave-current flows, our effort demonstrates that bedform volume at any given time was dependent on both

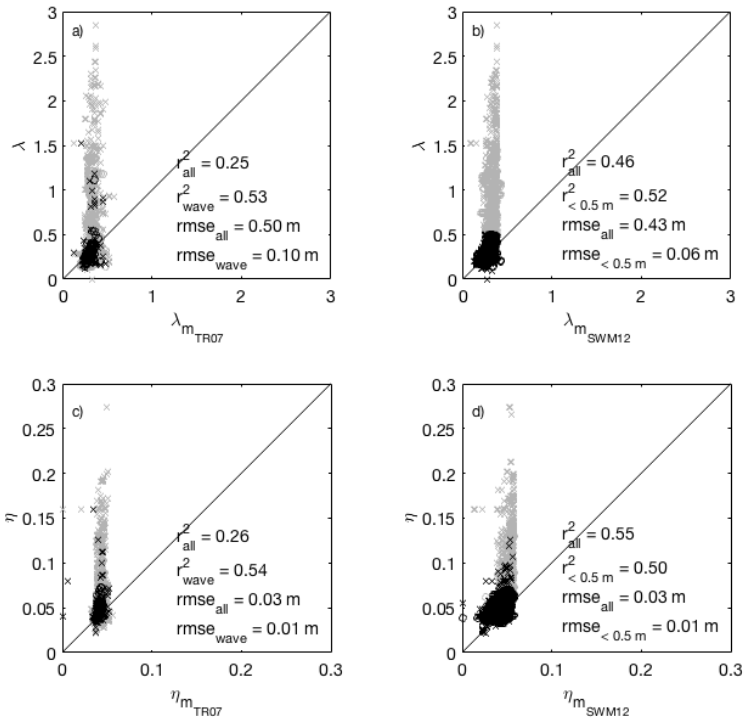

Figure 3.13: Observed vs. modeled bedform λ (panels a) and b)) and η (panels c) and d)) for site S1 in $\times$ and S2 in o. The grey markers show all data, and the black markers show the subset of data that the model was designed and tested on. a,c) plot the Traykovski (2007) model from (3.15), where the data in black are for wave dominant flows only, b,d) plot the Soulsby et al. (2012) model from (3.16), where the data in black are for bedforms less than 0.5 m in wavelength only. The model $rmse$ and r^2 are indicted in the lower right corner of each panel.

the sediment transport rate and the time duration that the bedform was exposed to the flow field. Measured changes in bedform volume were additionally shown to be characterized with the sediment continuity equation, or Exner equation, integrated over the bedform adjustment time of growth, which to our knowledge is a new contribution that builds upon past efforts. The sediment continuity equation while accounting for bedform adjustment/growth times may be a viable method for temporal and spacial morphologic change predictions of bedforms, especially in combined wave-current flows and with bedforms of a larger scale.

CHAPTER 4

OBSERVATIONS OF BEDFORM MIGRATION AND BEDLOAD SEDIMENT TRANSPORT IN COMBINED WAVE-CURRENT FLOWS

4.1 Abstract

Bedload transport is an important mechanism for sediment flux in the coastal nearshore. Yet few studies examine the relationship between bedform evolution and net sediment transport. Our work contributes concurrent observations of bedform mobility and bedload transport in response to current dominant, wave dominant, and combined wave-current flows in the nearshore. Findings show that bedload sediment flux from migrating bedforms during combined wave-current conditions account for at least 20% more bedload transport when compared with wave dominant flows and at least 80% more than current dominant flows. Bedforms were observed to transport the most sediment during periods with strong currents, with high energy skewed waves, and while bedform orientation and transport direction were aligned. Eleven bedload transport models formulated to be used in combined flows (both shear and energetics based), were compared with sediment flux estimated from measured bedform migration. Results show that regardless of flow type, bedform migration rates are directly proportional to the total kinetic energy contained in the flow field. Such that an energetics type sediment transport model may be most representative for our data.

For reference see: Chapter 3, Appendix B, Appendix C, Appendix D, and Appendix E

4.2 Introduction

Subaqueous coastal change is driven by sediment mobility in response to currents, waves, and combined wave-current flows. Sediment transport is broadly considered in two classifications,

bedload and suspended load transport (van Rijn, 1993). Bedload transport is characterized by sediment that is mobilized, but still rolling or bouncing along the bed through grain-grain interactions, while under suspended load transport sediment is entrained by turbulence into the flow field (Julien, 1998; Jaffe and Rubin, 1996). Due to the quick bedload response to localized flow, evolution of bottom morphology may depend more strongly on bedload than suspended load transport (Soulsby and Damgaard, 2005). The focus of our effort was on bedload transport associated with migrating bedforms in the nearshore region.

There are several bedload transport regimes. The lowest energy state is incipient motion, where grains are just starting to move (Nielsen, 1992). During the highest energy states, sheet flow becomes the dominant regime where several layers of sediment are mobilized simultaneously, potentially resulting in bed flattening (Zala Flores and Sleath, 1998; Lanckriet et al., 2012). Our interests were on the intermediate energy states, where bedforms form and migrate in response to waves, currents, or combined wave-current flows (Gallagher et al., 1998; Traykovski et al., 1999). In the nearshore, mobile bedforms are common in the surfzone, as well as in tidal inlets; regions that may only occasionally reach high-energy sheet flow transport conditions, making intermediate energy states and associated bedform mobility important to understanding coastal bathymetric adjustment.

Bedload transport via bedform migration can occur within mean current, wave, and combined wave-current flow conditions. In mean current dominant flows, bedform migration occurs by grains being pushed up the stoss side of the bedform and deposited on the lee side by the current (Fredsøe and Deigaard, 1992; van Rijn, 1993). In wave dominant flows, migration of bedforms is thought to occur due to wave streaming and wave velocity skewness and/or wave velocity asymmetry (Davies and Villaret, 1999; Nielsen and Callaghan, 2003). In combined flows, bedload transport typically is thought to occur by sediment being mobilized by waves and then advected by currents within the botom boundary layer (Amos et al., 1999).

There are many observations of bedform response to wave dominant or current dominant flows (e.g. Nielsen (1992), van Rijn (1993), Traykovski et al. (1999), Soulsby et al. (2012)); however, there are limited observations of bedform response to combined flows, especially in a field environment (Amos et al., 1999; Smyth and Li, 2005; van Rijn, 2007; Perillo et al., 2014). Existing datasets of bedform response to combined flows in the laboratory (e.g. Lacy et al. (2007); Catano-Lopera and Garcia (2006); Perillo et al. (2014)) and in the field (e.g. Li and Amos (1998); Amos et al. (1999); Gallagher et al. (1998); Passchier and Kleinhans (2005); Soulsby et al. (2012)) focus on bedform generation, roughness geometry, and orientation, but less frequently discuss bedload transport associated with the migration of combined flow bedforms. Additionally, the models that are developed to predict bedload transport within combined wave-current flows have not been widely compared to bedload sediment flux observations associated with bedform migration (Grant and Madsen, 1979; Soulsby, 1997; Li and Amos, 1998; Fredsøe et al., 1999; Styles and Glenn, 2000; van Rijn, 2007; Soulsby and Damgaard, 2005; Soulsby and Clarke, 2005).

Our effort captured bedform transformation and migration in response to waves, currents, and combined wave-current flows at two cross shore stations between the shore-parallel sandbar and the shoreline. Bedforms were exposed to storms and spring-neap tidal cycles, which generated a variety of flow conditions and transitions. The observed highly dynamic and non-equilibrium bedform response to these flow conditions are a strength of our dataset. Our efforts address: 1) bedform shape and mobility dependence on wave dominant, current dominant, and/or combined wave-current flows; 2) quantification of the sediment flux magnitude and sediment transport direction associated with bedform mobility within wave dominant, current dominant, and combined wave-current dominant flows; and 3) the strengths and limitations of existing models used to predict bedload transport in combined flows.

4.3 Methods

4.3.1 Experiment and Instrumentation

Data was collected during a field campaign at the Sand Engine mega-nourishment as part of MEGAPEX in the fall of 2014. Details of the experiment and instrumentation are described in Wengrove et al. (2018b). There were two instrument stations: S1 located 20 m from the shoreline, and S2 located 66 m further seaward along the same cross shore transect and 50 m shoreward of the approximately shore parallel sandbar. At each station there was a pencil beam sonar used to measure local bedform shape and mobility, as well as an acoustic Doppler instrument to measure the local velocity field. Additionally, large scale bathymetry was measured with regular surveys measured with an echo-sounder and GPS mounted on a jet-ski throughout the experiment. The coordinate system adopted herein is defined with respect to degrees from shore-normal, with 0° being onshore ($-x$), $+90°$ rotating counterclockwise from shore normal (towards the northeast, $+y$), and -90° rotating clockwise from shore normal (towards the southwest, $-y$).

4.3.2 Wave Dominant, Current Dominant, and Combined Flows

We distinguish in our observations between wave dominant, current dominant and combined flow conditions using a fraction of energy approach to assess the contribution of waves and/or currents to sediment flux. $E_{k_{wc}}$ is defined as the total kinetic energy in the flow field including both waves and currents. $E_{k_w}/E_{k_{wc}}$ is defined as the fraction of kinetic energy due to waves, so a value of 1 would be purely wave driven flow, and a value of 0 would be purely current driven flow. Previous literature has distinguished wave dominant flows from combined flows based on a ratio of wave induced to current induced friction velocity, where purely wave ripples occur at a friction velocity ratio of 0.5 or greater (Li and Amos, 1998; Lacy et al., 2007). To put this limit in terms of energy, this threshold of 0.5 is squared.

Therefore we define, $E_{k_w}/E_{k_{wc}}$ >0.75 to be wave dominant, 0.75≥ $E_{k_w}/E_{k_{wc}}$ ≥0.25 for combined wave-current flow, and 0.25> $E_{k_w}/E_{k_{wc}}$ to be current dominant. An energy approach is used instead of the friction velocity since is it fairly difficult to estimate the friction velocity in combined flow conditions, so using energy mitigates propagation of error through analysis. Additionally, the flow energy was either measured or using linear wave theory for the wave contribution and a log layer approximation for the mean flow contribution, attenuated through the water column to be estimated approximately 10 cm above the crest of the bedforms. Further details of hydrodynamic calculations including current velocity and direction (U, ϕ_c), orbital velocity and direction (u_o, ϕ_w), wave-current velocity (u_{wc}), and kinetic energy (E_k) can be found in Wengrove et al. (2018b) and Wengrove et al. (2017).

4.3.3 Bedform Migration and Sediment Flux

A time series of bedform migration magnitude and direction was estimated using subsequent local 2D bathymetric pairs from the pencil beam sonar. Each pair of bathymetries was processed with either a 2D cross correlation as defined in Wengrove et al. (2017) or a motion estimator process (MEP) least squares error approach (Perkovic et al., 2009). The 2D cross correlation is a measure of similarity of the two bathymetries based on the displacement of one relative to the other, highlighting shifts (or bedform migrations) between bathymetries. If there are bedforms with multiple wavelengths within the sonar view window then the 2D cross correlation method works well. However, when the bedforms get large, there may only be one wavelength in view; in this case, the MEP method is a more robust method because the least-squares analysis is much less sensitive for smaller viewing windows relative to bedform wavelength. Once the bedform displacement, $d_{xy} = (\boldsymbol{d}_x^2 + \boldsymbol{d}_y^2)^{0.5}$, is found between each subsequent bathymetric pair, the bedform migration rate and migration direction were found by $V_{mig.} = d_{xy}/t_s$ and $\phi_{mig.} = a\tan(\boldsymbol{d}_y/\boldsymbol{d}_x)$, respectively, where t_s is the sampling time between bathymetric pairs (Wengrove et al., 2017).

The transformation of bedform migration rate to volumetric bedload transport, $\boldsymbol{q}$, has been characterized with magnitude,

$$q_{bedform} = nV_{mig}\eta, \tag{4.1}$$

and direction (ϕ_{mig}), where n is the volume fraction of sediment and η is the bedform height (Traykovski et al., 1999; Amos et al., 1999). The formulation assumes that when the bedform migrates, the entire bedform is transported, and that the sand transport is equivalent to the trapezoid defined by the moving ripple face through time (Amos et al., 1999). The method described in (4.1) effectively yields the maximum bedform transport rate. Details of bedform statistics obtained from 2D wavenumber spectra of the sonar imagery data including bedform wavelength (λ), height (η), and orientation (ϕ_r) can be found in Wengrove et al. (2018b) and Wengrove et al. (2017). Finally, bedform dimensionality (2D/3D) was determined from the bedform directional spread in the 2D wavenumber spectra (Wengrove et al., 2018b), where the delineation between 2D and 3D was defined with a spread of $< 20°$.

4.3.4 Prediction of Bedload Transport Magnitude

Since direct measurements of bedload transport are difficult or time consuming to obtain, it is generally inferred from the velocity field using measured and modeled data. There are two broad approaches to infer sediment flux from velocity measurements. The first assumes that $q_b = f(\tau_b \text{ or } \theta)$, indicating that bedload flux is a function of dimensional or non-dimensional bed stress (Shields, 1936), and the second assumes that $q_b = f(u^n)$, a family of equations referred to as energetics models (Bagnold, 1966). Table 1 lists eleven models that are commonly used to estimate bedload sediment transport within the nearshore. In Table 1, the model reference is listed next to the model foundation, which indicates whether the model is shear stress based or energetics based; within the shear stress based models, the various formulations are further categorized a dependent or independent approach, where the dependent models require an outside measurement or approximation of bed stress, and

the independent models take an all-in-one approach where the shear stress model is imbedded in the transport formulation. The remainder of this section introduces each family of transport models with an example as well as provides insight into where each is currently being employed.

Within the family of models that assumes $q_b = f(\tau_b \text{ or } \theta)$, there are many dependent semi-empirical models for bedload transport that assume an external bed stress measurement or formulation (Soulsby, 1997). This family of models is widely used within field and laboratory data analysis because direct measurements of bed shear inferred from boundary layer gradients can be used within these models. The most common of these semi-empirical models is the Meyer-Peter and Muller (1948) model,

$$q_{b_{MPM}} = 8(\theta - \theta_{crit})^{1.5} \rho_s d_{50} ((s-1) g d_{50})^{0.5}, \tag{4.2}$$

where θ_{crit} is the critical Shields parameter for sediment mobility, ρ_s is the sediment density, d_{50} is the median grain size, s is the sediment specific gravity, and g is the acceleration due to gravity. The Meyer-Peter Muller model is shown to estimate bedload flux well when there is reasonable confidence in estimates of bed stress (Rodriguez-Abudo and Foster, 2014). There are several excess stress models (that subtract the θ_{crit} from θ (as in 4.2)), but have varying gain factors and power exponents (Soulsby, 1997; Nielsen, 1992). If direct stress measurements are unavailable, these transport models can be paired with external formulations to estimate bed stress. Some example formulations to estimate the bed stress in combined flows include Styles and Glenn (2000), Madsen (1994), Soulsby and Clarke (2005), and Nielsen (1992) combined with Li and Amos (1998). The bed stress in all of these models is estimated using current and wave friction factors. Meyer-Peter and Muller (1948) is used widely with various bed stress approximations to estimate bedload transport. Soulsby and Damgaard (2005) is an example of another excess stress based transport model that is specifically formulated for use in combined wave-current flows incorporating the Soulsby and Clarke (2005) bed stress approximation.

The independent style of transport models still assume $q_b = f(\tau_b \text{ or } \theta)$, but they take an all-in-one approach with imbedded stress submodels and friction factors, such as van Rijn (1993), van Rijn et al. (2004), van Rijn (2007), Soulsby/van Rijn or Soulsby (Soulsby, 1997), and van der A et al. (2013). Each of these models, excluding the van der A et al. (2013) assume that intra-wave dynamics are steady, while van der A et al. (2013) is a semi-unsteady transport model. One bedload transport model is the Soulsby/van Rijn model (Soulsby, 1997), in which

$$q_{b_{SVR97}} = A_b U \alpha^{2.4}(1 - 1.6tan\beta), \tag{4.3}$$

where,

$$A_b = \frac{0.005h(D/h)^1.2}{[(s-1)gd_{50}]^{1.2}},$$

$$\alpha = [U^2 + (0.018/C_D)u_{rms}^2]^{0.5} - U_{cr},$$

$$U_{cr} = 0.19d_{50}^{0.1}log(4h/0.0005),$$

$$C_D = \Big(\frac{0.4}{log(h/z_o) - 1}\Big)^2$$

h is the water depth, U is the current velocity, u_{rms} is the root mean square wave velocity, β is beach slope, $z_o = 0.006$ m is the roughness height, α is a parameterization for the turbulent kinetic energy in the flow, and C_D is a drag coefficient based on the logarithmic boundary layer shape.

The sediment transport modules imbedded in large scale coastal change models such as Delft3D (Lesser et al., 2004), XBeach (Roelvink et al., 2015), and COAWST (Warner et al., 2008) use stress-based transport approximations (either a dependent or independent approach). The van Rijn (1993), van Rijn et al. (2004), van Rijn (2007), van der A et al. (2013) approaches are used in Delft3D, XBeach implements the Soulsby/van Rijn (Soulsby, 1997) formulation, while COAWST uses the Meyer-Peter and Muller (1948) transport model with Styles and Glenn (2000) bed stress or Soulsby and Damgaard (2005) transport model with Soulsby and Clarke (2005) bed stress.

The energetics family of transport models assume that the sediment flux is a function of the imposed freestream flow field, or $q_b = f(u^n)$ (Bagnold, 1966). These types of models are based on the energetics approach (Bowen, 1980; Bailard and Inman, 1981), where, unlike an excess stress model, the energetics models directly relate bedload transport to higher moments of the velocity field including skewness and asymmetry. Hsu et al. (2006) modified the energetics models to include transport from both waves and currents,

$$q_{b_{HEG06}} = k_w \frac{e_b}{\tan\phi_{rep.}} |u_o|^2 u_o + k_c \frac{e_b}{\tan\phi_{rep.}} \sqrt{U^2 + u_o^2}^2 U, \tag{4.4}$$

where $k_w = \frac{0.0046}{(s-1)g}$ and $k_c = \frac{0.0053}{(s-1)g}$ are friction coefficients calibrated for sandbar mobility and $e_b = 0.135$ is a numerical coefficient based on the efficiency of the transport mode, and $\phi_{rep.} = 30^\circ$ is the friction angle of the sediment based on the angle of repose. Energetics based models are often used to estimate cross-shore sediment transport, specifically related to sandbar evolution, but to our knowledge have not been used to estimate bedload transport due to bedform migration (Zhao and Kirby, 2005). Each of these models are compared herein to transport estimates derived from observations of bedform migration.

4.3.5 Prediction of Bedload Transport Direction

When bedforms migrate, they transport their mass in a direction oriented in someway to the prevailing flow direction. The maximum gross bedform normal transport (MGBNT) is a method to estimate the bedform migration direction from the direction of the flow field, a quantity that does not distinguish wave and current directions (Gallagher et al., 1998; Lacy et al., 2007). The MGBNT is defined by the combined influence of the transport directions over the timescale of the bedform development; that is bedforms align to maximize their gross normal transport. The MGBNT occurs at an angle, α, in which the transport $\boldsymbol{T}$ is maximized.

$$\boldsymbol{T} = \sum_i \boldsymbol{D}_i |sin(\gamma_i - \alpha)| \tag{4.5}$$

Table 4.1: Bedload transport models

model reference	*foundation*	*abbreviation*
van Rijn et al. (2004)	$q_b = f(\tau_b)$, independent q_b	VR04
van Rijn (2007)	$q_b = f(\tau_b)$, independent q_b	VR07
Soulsby (Soulsby, 1997)	$q_b = f(\tau_b)$, independent q_b	S97
Soulsby-van Rijn (Soulsby, 1997)	$q_b = f(\tau_b)$, independent q_b	SVR97
Meyer-Peter and Muller (1948) + Madsen (1994)	$q_b = f(\tau_b)$, dependent q_b+τ_b	MPM-M94
Meyer-Peter and Muller (1948) + Nielsen (1992) & Li and Amos (1998)	$q_b = f(\tau_b)$, dependent q_b+τ_b	MPM-N92LA98
Meyer-Peter and Muller (1948) + Soulsby and Clarke (2005)	$q_b = f(\tau_b)$, dependent q_b+τ_b	MPM-SC05
Meyer-Peter and Muller (1948) + Styles and Glenn (2000)	$q_b = f(\tau_b)$, dependent q_b+τ_b	MPM-SG00
Soulsby and Damgaard (2005) + Soulsby and Clarke (2005)	$q_b = f(\tau_b)$, dependent q_b+τ_b	SD05-SC05
Hsu et al. (2006)	$q_b = f(u^n)$, energetics	HEG06
van der A et al. (2013)	$q_{net} = f(\tau_b)$, independent q_{net}	VDA13

where, $\boldsymbol{D}_i$ and γ_i are the magnitude and direction of individual transport vectors (Gallagher et al., 1998). The summation window is dependent on the timescale of the bedform development/adjustment.

4.4 Results

4.4.1 Flow Forcing Bedform Shape and Migration

Observations obtained during MEGAPEX captured bedform response to wave, current, and combined wave-current flow conditions. Both ripples and megaripples were observed at S1 and S2 during the 2014 deployment. Time series of bedform variability in dimensionality, size, and migration rate with concomitant flow energy magnitude and dominance at site S1 is shown in Figure 4.1. At times bedforms were 2D or 3D (usually during flow transitions), and were observed during all flow energy conditions (Figure 4.1c,d). Megaripples were observed during periods with higher flow energy, and during energetic combined wave-current flow. Additionally, lunate megaripples were observed on three occasions at S1 (Figure 4.1c and

d, highlighted in blue). Confidence limits in observed bedform wavelength was determined by the spread in the energy density peak in the 2D wavenumber spectra (Wengrove et al., 2018b) and is evident in representative snap shots from the S1 time series of current, wave, and combined flow dominant bedform evolution (Figures 4.2-4.5). In addition to bedform shape and orientation, migration rate and migration direction also shift in response to flow forcing within current dominant (Figure 4.2), wave dominant (Figure 4.3), and combined wave-current flow conditions (Figures 4.4 and 4.5).

As flow conditions approached current dominance, the transition from wave to current dominance was gradual (e.g. with the onset of flood tidal flow). During the transition, the bedform transport direction led the bedform orientation (as shown in Figure 4.2a and e-j) by approximately 40 minutes to 1 hour, which is also approximately equal to one third of the bedform growth adjustment time, τ (Wengrove et al., 2018b). Additionally, the migration velocity began to ramp up before the bedform wavelength evolved (Figure 4.2c) to the longer and fairly small steepness ($\eta/\lambda = 0.06$) bedform shown in (Figure 4.2g-j). Such bedforms have a steepness consistent with dunes as observed by Fredsøe and Deigaard (1992). Observations of transport with a phase lead between migration direction and bedform orientation occurred frequently during the onset of spring flood tide at both sites S1 and S2.

Wave dominant flow conditions occurred during typical conditions (no storm), as well as during swell conditions (just before a storm) (Figure 4.1). Bedforms were classified as wave-orbital ripples, with wavelength and height dependent on the energy in the flow field (Wengrove et al., 2018b). Wave dominant bedforms were usually 2D in shape, as seen with the small spread in bedform direction (Figure 4.3d and e-j). Bedforms migrated further when the ripple orientation and migration direction were aligned (Figure 4.3h-j compared with panel c).

During periods of combined wave-current flow there were several instances of megaripples with wavelengths of >0.8 m and migration rates in excess of 2 cm/min. Megaripples generally transitioned from 3D to 2D over the course of their formation. Figure 4.4 shows

a representative megaripple formation during combined wave current flows at S1 (other instances of megaripples are highlighted in Figure 4.1c). When the combined flows become fairly strong, with total kinetic energy levels of greater than 0.5 m^2/s^2, lunate mega-ripples are observed migrating through the field of view (Figure 4.5f-h; at S1 occurring on three occasions). Previously observed lunate megaripples in the nearshore by Ngusaru and Hay (2004) and Hay and Mudge (2005) generally occur under weak mean currents, and have the horns of the lunate bedform migrate in the onshore direction. However, Thornton et al. (1998) observed lunate megaripples migrating in the alongshore direction, consistent with our observations where the horns of the bedform were migrating in the alongshore direction, towards the northeast, in the prevailing direction of the flood tidal current. The migration of the bedform preceded the growth of the bedform wavelength (Figure 4.5b), and this building period was shorter with higher energy flows.

Qualitatively, bedform migration magnitude had a direct relationship with the flow energy regardless of whether the flow was wave dominant, current dominant, or combined wave-current (panel b in Figures 4.2 - 4.5). Observations show that the maximum migration velocity was concomitant with a peak in the total kinetic energy and/or the period when the bedform orientation was aligned with the bedform migration direction. Signifying that the total energy contained in the flow is directly proportional to the overall contribution of bedform migration to bedload sediment flux.

4.4.2 Observations of Bedform Migration Direction

The observed bedform migration direction relative to the current and wave directions, for all data at S1 and S2 is shown in Figure 4.6. It is clear from the scatter that the bedforms were neither being forced solely by the currents ($r^2 = 0.40$, $rmse = 71°$) nor by the waves ($r^2 = 0.02$, $rmse = 37°$). Bedforms appear migrate in response to some combination of the current and wave directions, resulting in a migration direction between ϕ_c and ϕ_w.

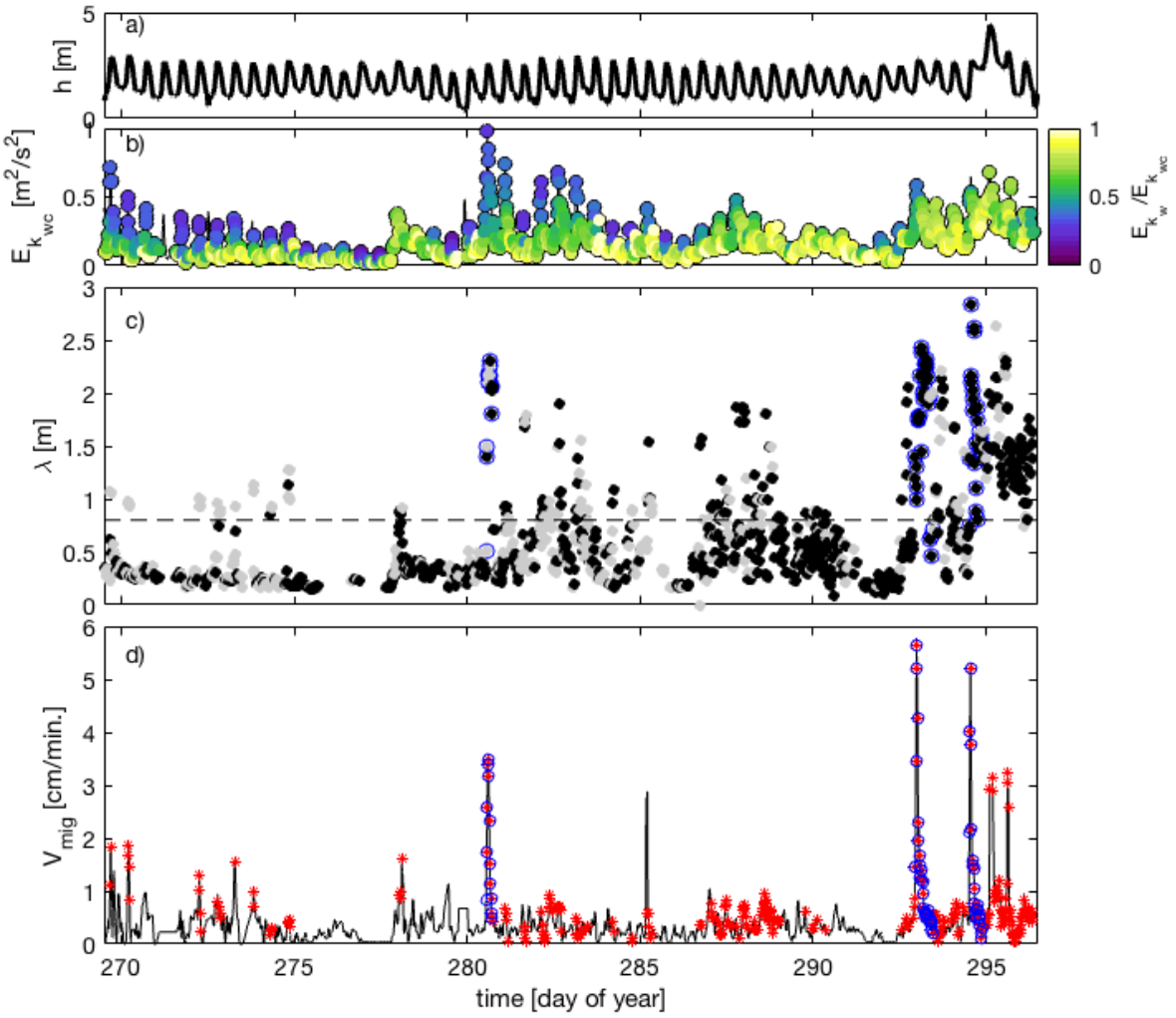

Figure 4.1: Time series showing bedform dimensionality (2D/3D) and scale (ripple/megaripple) in response to flow energy at S1. Panel a) shows the depth, h. Panel b) shows the total kinetic energy, $E_{k_{wc}}$ colored by fraction of kinetic energy due to waves $E_{k_w}/E_{k_{wc}}$. Panel c) shows bedform wavelength, λ, colored by the bedform dimensionality, 2D bedforms are in grey and 3D bedforms are in black. Bedforms with wavelengths greater than the dashed line are considered to be megaripples, with points highlighted with blue o showing observed occurrences of lunate megaripples. Panel d) shows the bedform migration rate, $V_{mig.}$ (solid black line), with red * indicating occurrences of megaripples, and blue o showing observed occurrences of lunate megaripples.

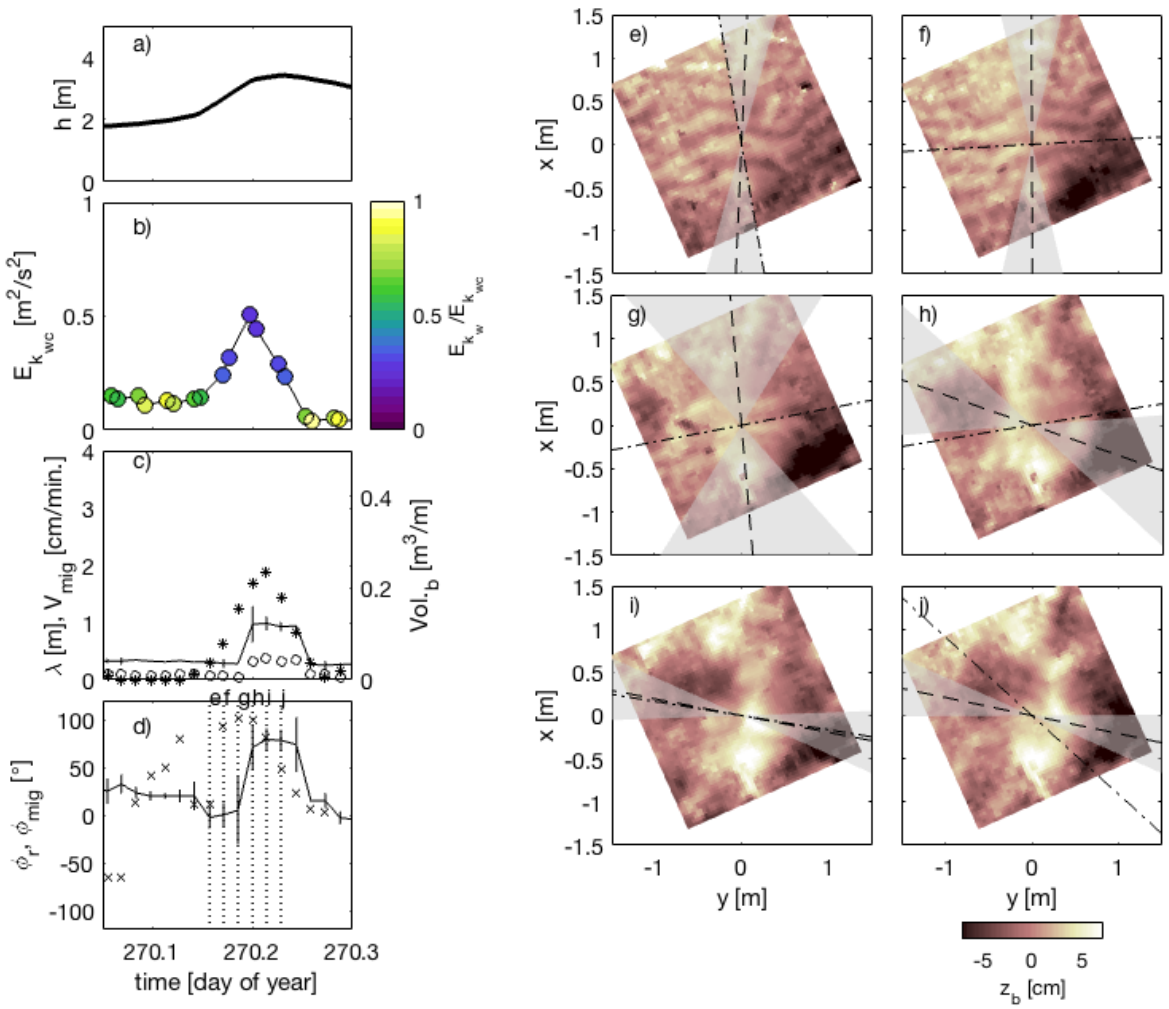

Figure 4.2: Time series of bedform adjustment with the onset of a flood tidal current at S1. Panel a) shows the depth, h. Panel b) shows the total kinetic energy, $E_{k_{wc}}$ colored by fraction of kinetic energy due to waves $E_{k_w}/E_{k_{wc}}$. Panel c) shows the bedform migration rate, $V_{mig.}$ (*), corresponding bedform wavelength λ (solid black line with vertical range bars representing wavelength uncertainty) (left axis), and bedform volume, $Vol._b$ (o) (right axis). Panel d) shows the bedform orientation, ϕ_r (solid black line with vertical range bars representing directional spread), and bedform migration direction, $\phi_{mig.}$ (×). Panels e-j) show sample local bathymetries taken at times indicated by the vertical dotted lines in (d), where the dashed line and shaded region in each panel indicate the bedform orientation (ϕ_r) and directional spread, respectively, and the dash-dot line indicates the bedform migration direction ($\phi_{mig.}$).

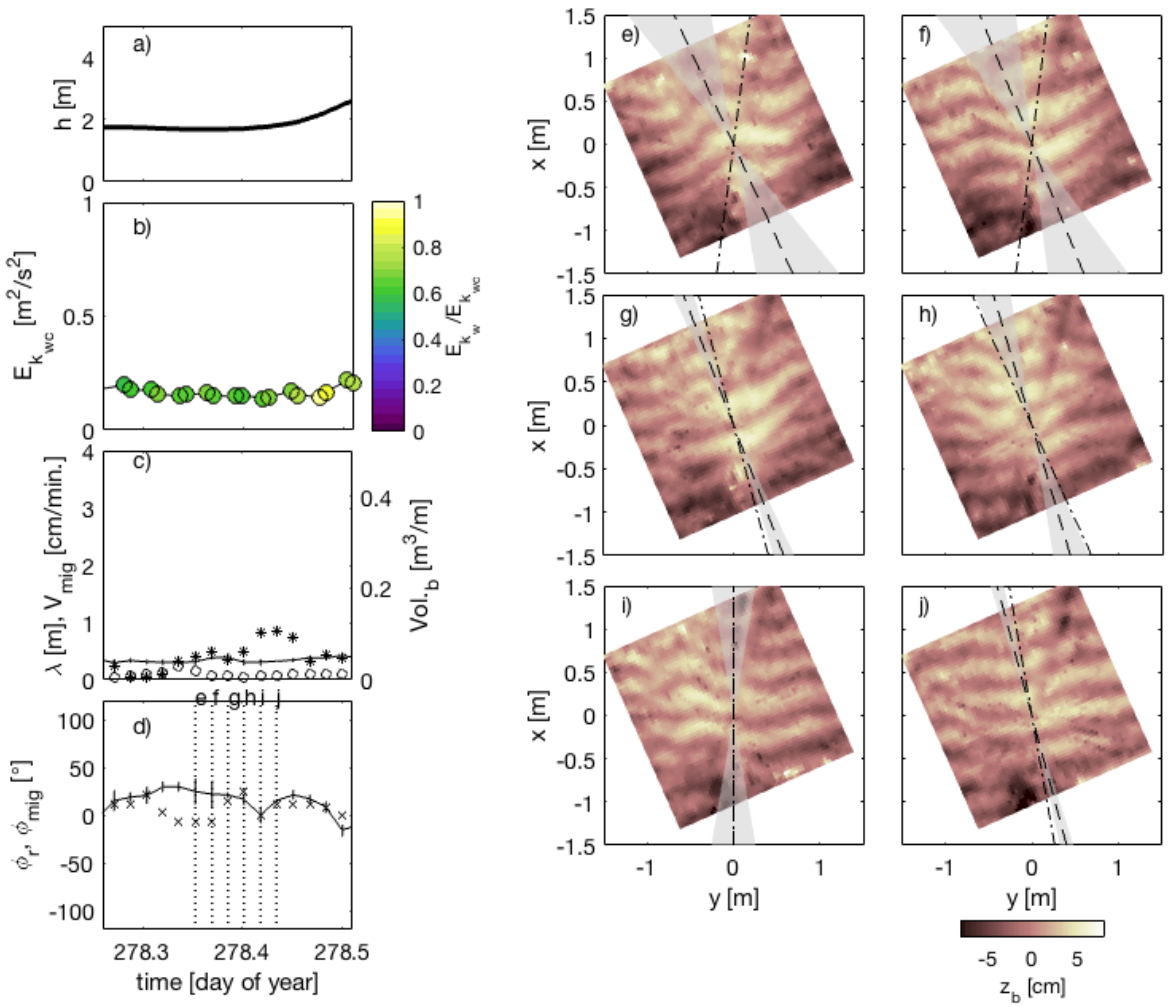

Figure 4.3: Time series of bedform adjustment in wave dominant flow at S1. Panel a) shows the depth, h. Panel b) shows the total kinetic energy, $E_{k_{wc}}$ colored by fraction of kinetic energy due to waves $E_{k_w}/E_{k_{wc}}$. Panel c) shows the bedform migration rate, $V_{mig.}$ (*), corresponding bedform wavelength λ (solid black line with vertical range bars representing wavelength uncertainty) (left axis), and bedform volume, $Vol._b$ (o) (right axis). Panel d) shows the bedform orientation, ϕ_r (solid black line with vertical range bars representing directional spread), and bedform migration direction, $\phi_{mig.}$ ($\times$). Panels e-j) show sample local bathymetries taken at times indicated by the vertical dotted lines in (d), where the dashed line and shaded region in each panel indicate the bedform orientation (ϕ_r) and directional spread, respectively, and the dash-dot line indicates the bedform migration direction ($\phi_{mig.}$).

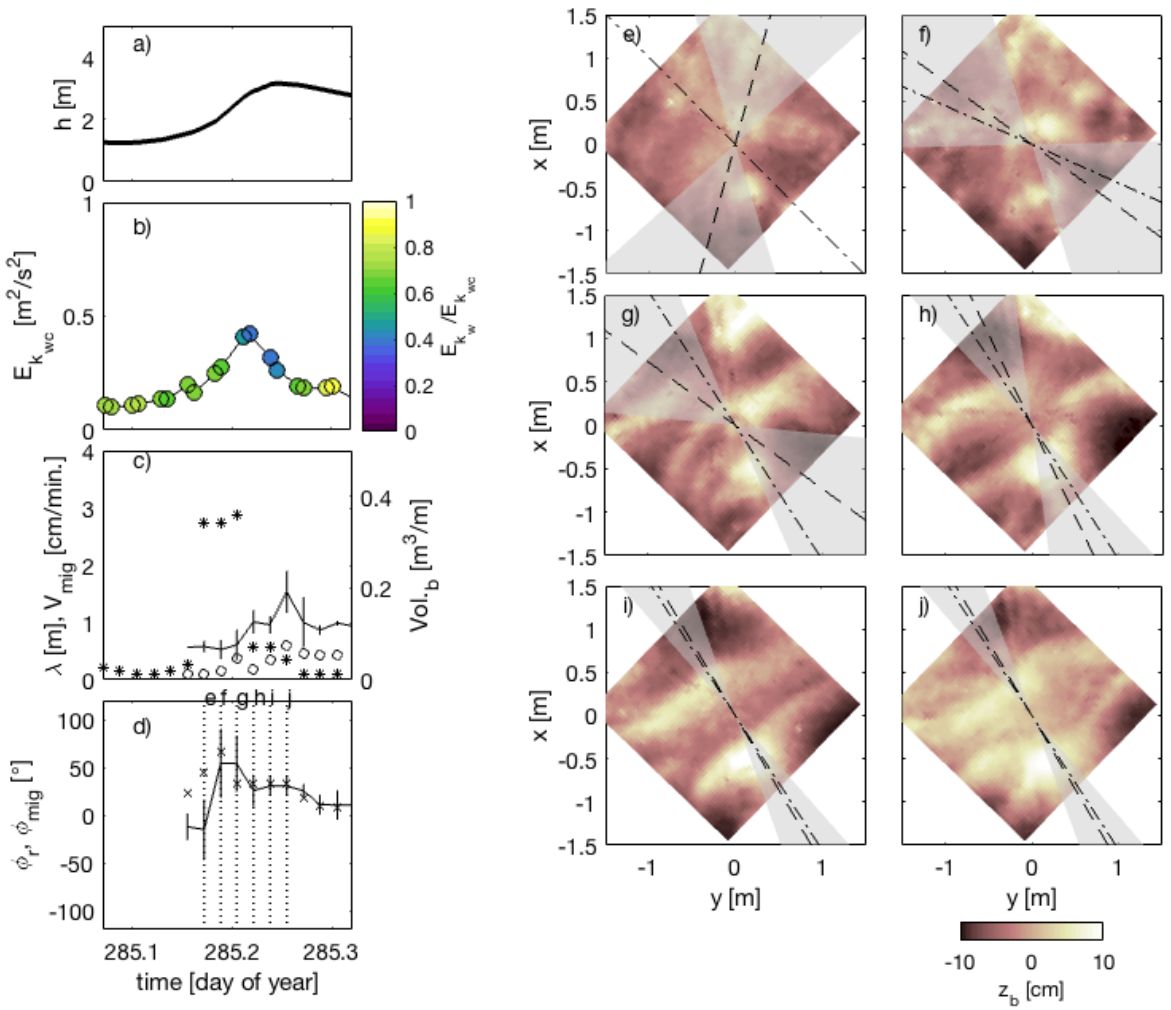

Figure 4.4: Time series of bedform adjustment during combined flow at S1 - megaripple formation. Panel a) shows the depth, h. Panel b) shows the total kinetic energy, $E_{k_{wc}}$ colored by fraction of kinetic energy due to waves $E_{k_w}/E_{k_{wc}}$. Panel c) shows the bedform migration rate, $V_{mig.}$ (*), corresponding bedform wavelength λ (solid black line with vertical range bars representing wavelength uncertainty) (left axis), and bedform volume, $Vol._b$ (o) (right axis). Panel d) shows the bedform orientation, ϕ_r (solid black line with vertical range bars representing directional spread), and bedform migration direction, $\phi_{mig.}$ (×). Panels e-j) show sample local bathymetries taken at times indicated by the vertical dotted lines in (d), where the dashed line and shaded region in each panel indicate the bedform orientation (ϕ_r) and directional spread, respectively, and the dash-dot line indicates the bedform migration direction ($\phi_{mig.}$).

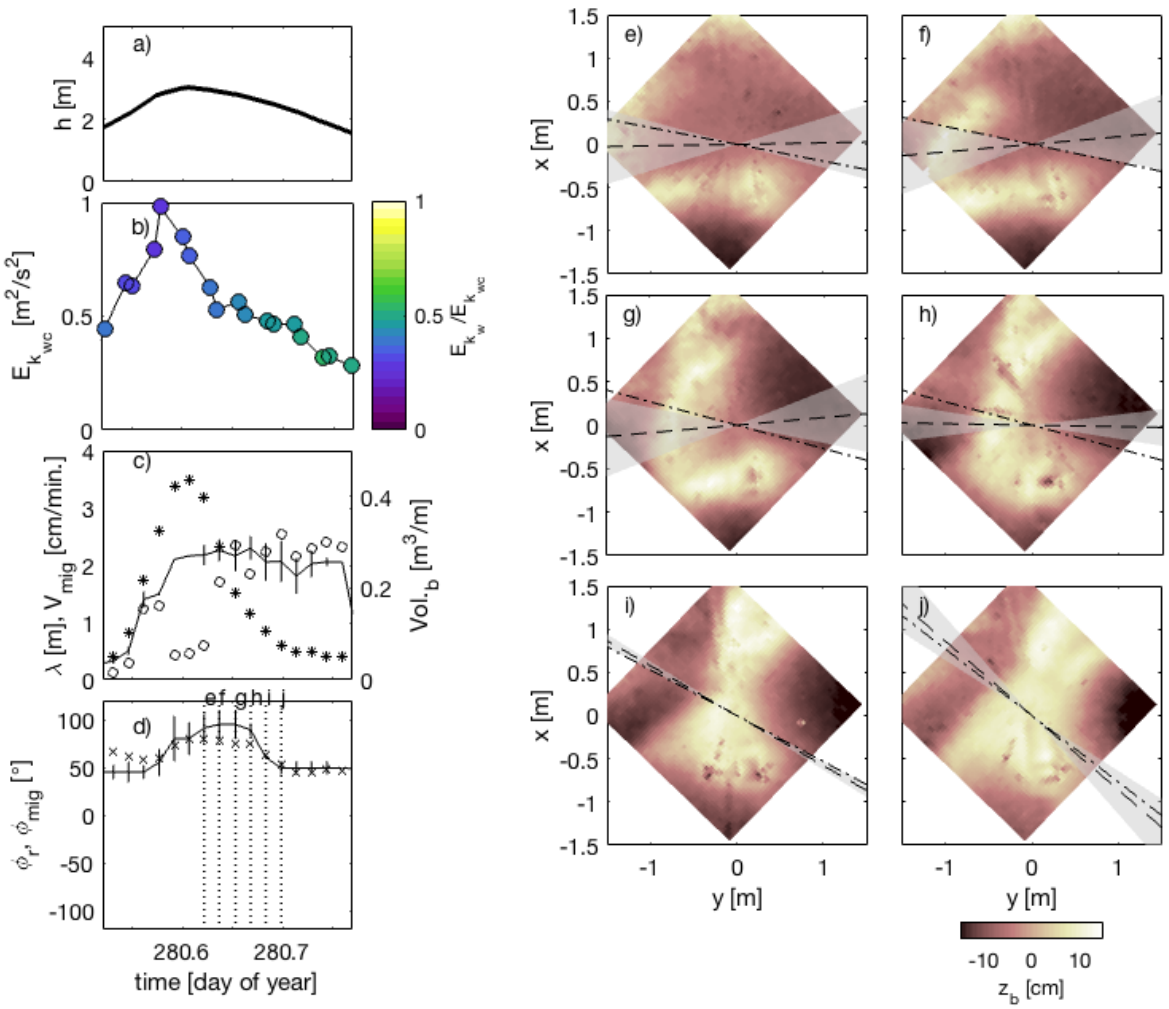

Figure 4.5: Time series of bedform adjustment during high energy combined flow at S1 - lunate megaripple formation. Panel a) shows the depth, h. Panel b) shows the total kinetic energy, $E_{k_{wc}}$ colored by fraction of kinetic energy due to waves $E_{k_w}/E_{k_{wc}}$. Panel c) shows the bedform migration rate, $V_{mig.}$ (*), corresponding bedform wavelength λ (solid black line with vertical range bars representing wavelength uncertainty) (left axis), and bedform volume, $Vol._b$ (o) (right axis). Panel d) shows the bedform orientation, ϕ_r (solid black line with vertical range bars representing directional spread), and bedform migration direction, $\phi_{mig.}$ (×). Panels e-j) show sample local bathymetries taken at times indicated by the vertical dotted lines in (d), where the dashed line and shaded region in each panel indicate the bedform orientation (ϕ_r) and directional spread, respectively, and the dash-dot line indicates the bedform migration direction ($\phi_{mig.}$).

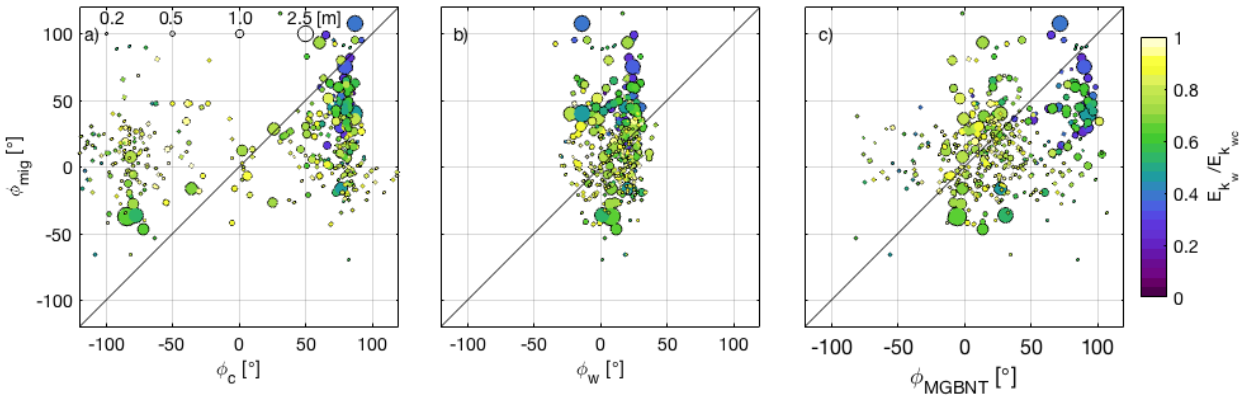

Figure 4.6: Scatter plots of bedform migration direction, $\phi_{mig.}$ (y-axis) plotted against a) the current direction, ϕ_c, b) the wave direction, ϕ_w, and c) the MGBNT direction, ϕ_{MGBNT} using a variable adjustment time τ (see Discussion). Points are colored by fraction of energy due to waves and scaled by bedform wavelength, λ, as indicated in (a). A 1:1 ratio line is plotted in black on each panel.

4.5 Discussion

4.5.1 Statistics of Bedform Migration and Implications for Transport

Bedform migration rates under wave, current, and combined wave-current flow in combination with the bedform shape characterize the bedload transport due to bedform migration. Using the bedform migration rate and height, the bedload sediment flux due to moving bedforms was calculated with (4.1). The bedform migration rate and sediment flux increased with increased total kinetic energy, regardless of whether conditions were dominated by wave, current, or combined wave-current flows with a power law relationship (Figure 4.7). Additionally, as total kinetic energy increases, so does the bedform volume, (volume is represented with marker size in Figure 4.7). Bedforms transporting the most sediment are influenced (at least somewhat) by currents (occuring when there is a low fraction of kinetic energy due to waves; green to blue colors on Figure 4.7).

There are several theories of forcing mechanisms for bedform migration, with mean currents and asymmetric velocities being the most prevalent in literature (Fredsøe and Deigaard, 1992; van Rijn, 1993; Davies and Villaret, 1999; Nielsen and Callaghan, 2003). Five characteristic indicators of the flow field (current magnitude, orbital velocity magnitude, velocity skewness, velocity asymmetry, and total kinetic energy) are compared withbedform sediment flux for current dominant (Figure 4.8a-e), wave dominant (Figure 4.8f-j), and combined wave-current flows (Figure 4.8k-o). All bedforms within current dominant flows transported less than 0.1×10^{-4} $m^3/m/s$ of sediment due to bedform migration (Figure 4.8a), suggesting that current dominant flows in our dataset were not consistent with large sediment flux. Within current dominant flows, there was not a strong relationship between sediment flux and orbital velocity, skewness, or asymmetry; however, the current dominant bedforms did transport more sediment with increased flow energy (Figure 4.8a-e). During wave dominant flows there were occurrences of sediment flux above 0.20×10^{-4} $m^3/m/s$ (Figure 4.8f-j) that occurred when the orbital velocity was large and the total kinetic energy was high, but also

with increased velocity skewness (Figure 4.8h). Data show that in order for wave dominant bedforms to transport sediment at rates over 0.20×10^{-4} $m^3/m/s$, the waves not only must be skewed, but also have a total kinetic energy over 0.4 m^2/s^2 (Figure 4.8h). This relationship was not consistent with velocity asymmetry (instances of high velocity asymmetry did not occur with increased bedload sediment flux; Figure 4.8i). It may be that velocity skewness forces migration and velocity asymmetry forces fluidization (Sleath, 1999). Finally, during combined flow conditions (Figure 4.8k-o), periods of bedload sediment flux due to bedform migration greater than 0.20×10^{-4} $m^3/m/s$ occurred when the current velocity magnitude increased above 0.5 m/s and the orbital velocity was larger than 0.5 m/s. During these events waves were sometimes (but not necessarily) skewed, and velocity asymmetry was low. In general, the observations indicate that for bedforms to migrate there needs to be either a strong current with a strong orbital velocity or skewed waves with a strong orbital velocity. Total kinetic energy in the flow field is an overarching indicator for increased bedform migration rates and bedload sediment flux due to bedform migration regardless of whether the flow is wave, current, or combined wave-current dominant.

Boxplot diagrams quantify the contributions to bedload transport driven by current dominant, wave dominant, and combined wave-current flows (Figure 4.9). Figure 4.9 shows several boxplots of relevant variables (bedform volume, bedform height, bedform migration rate) to calculate sediment flux, as well as boxplots that present the sediment flux distributions at both S1 and S2. A boxplot is a simple way to represent the distribution of data. The distribution mean (MN) and median (MD) are used as distinguishing statistics between flow conditions. Additionally, for reference, a histogram of the occurrences of current dominant, wave dominant, and combined wave-current flows both at S1 and S2 are shown in Figure 4.9a and b.

On average, at both sites, the median transport in combined flows was $0.2\ m^3/m/s$, which was 15% and 91% larger than wave dominant and mean current dominant flow, respectively. Furthermore, on average the mean transport was $0.38\ m^3/m/s$ in combined flows, which was

24% and 82% greater than wave dominant and mean current dominant flow, respectively. Bedform behavior at site S1 (closer to shore) was more heavily influenced by combined flows, where mean combined flow transport accounted for a 45% greater sediment flux than wave dominant transport. At S2, the transport was comparable between wave dominant and combined wave-current flows (note, S2 was not deployed during the larger storm events). Boxplot diagrams for S1 show distributions of the full 27 day deployment, whereas boxplot diagrams for S2 only represent the middle 16 days; distributions for only the middle 16 days at S1 show similar trends to the S2 distributions (not shown). Transport contributions from combined flows were up to 50% greater than sediment flux associated with wave dominant flows, and even more so with current dominant flows.

4.5.2 Bedform Sediment Flux Compared with Existing Bedload Transport Models

Bedload transport models rely on either a bed stress approach or an energetics approach. Eleven different bedload transport models – all formulated to work in combined flows – are compared to observations of bedload transport due to bedform migration for both site S1 and site S2 (Figure 4.10, Table 1). Models presented in panels a-d and k take an independent all-in-one approach to estimate the bedload transport and use a friction factor and drag coefficient to estimate stress, models presented in panels e-i are transport models that depend on an outside bed shear stress approximation measurement or model, and the model presented in panel j uses an energetics approach. The model abbreviations used in this section and in Figure 4.10 are given in Table 1.

Qualitatively, some models under-predicted transport from bedform migration (VR04 and VR07), many over-predicted transport (S97, SD05-SC05, MPM-M94, MPM-N92LA98, MPM-SG00, HEG06, and VDA13), and two models visually performed decently (SVR97 and MPM-SC05). Figure 4.11 shows calculated $rmse/\sigma$ and r^2 for data from both the S1 and S2 sites for three portions of the data: the whole dataset (*all data*), for *combined* flow

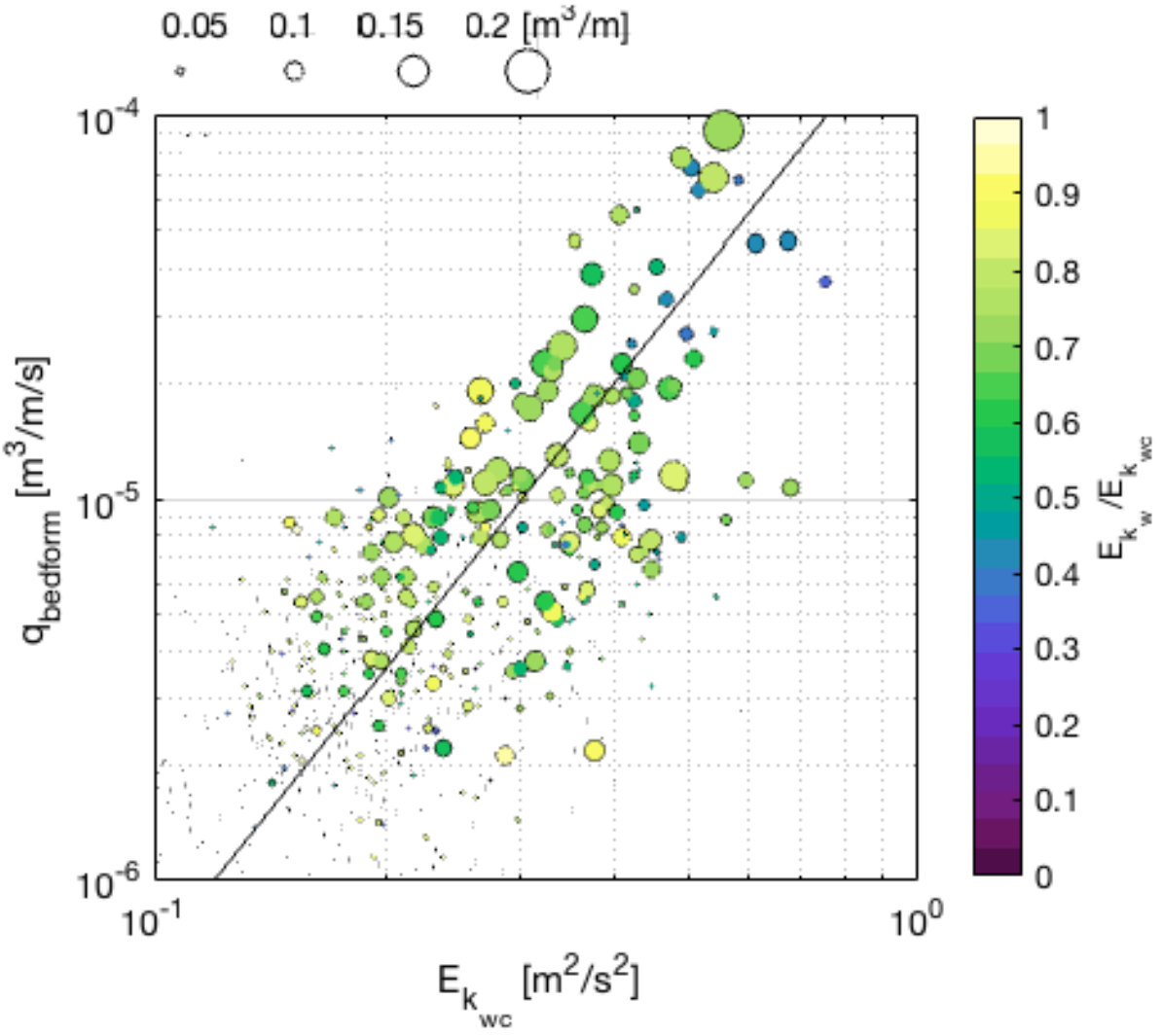

Figure 4.7: Total kinetic energy, $E_{k_{wc}}$, plotted against observed bedform sediment transport flux, $q_{bedform}$, on logarithmic scale. Data are colored by the fraction of energy due to waves, to show flow dominance. Marker size is scaled with bedform volume, $Vol._b$, as shown in the upper left hand corner. The solid black line in is a fit line described as $q_{bedform} = 2x10^{-4}E_{k_{wc}}^{2.5}$.

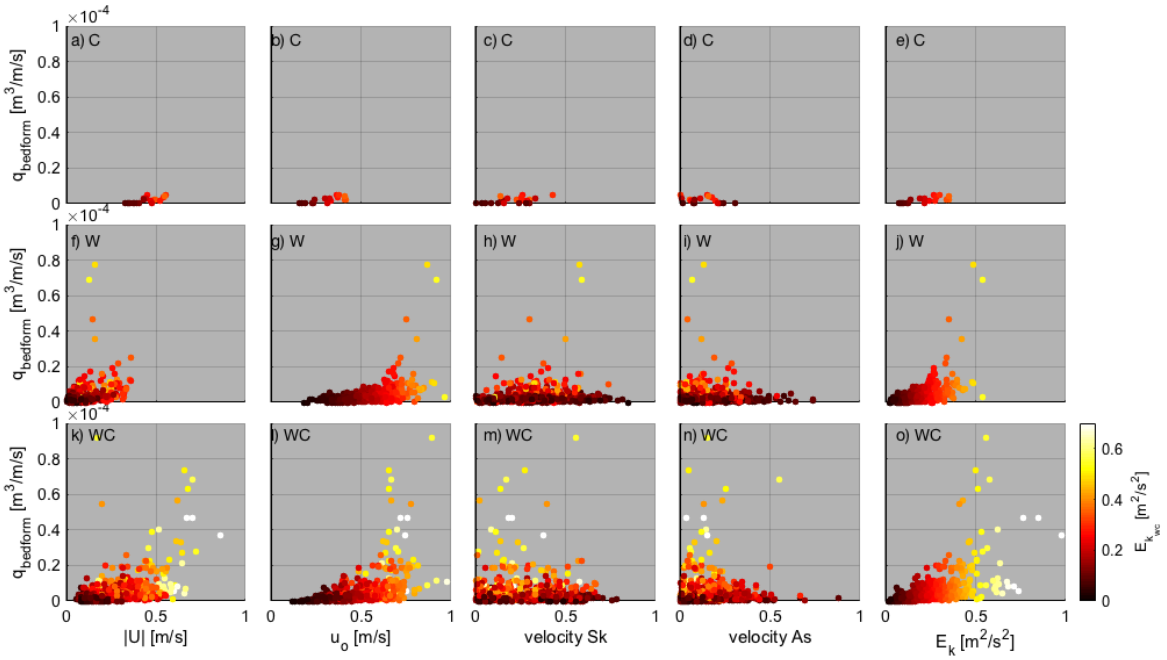

Figure 4.8: Scatter plots of U, u_o, velocity Sk, velocity As, E_k plotted against the bedload sediment flux due to bedform migration, $q_{bedform}$, and colored by the total kinetic energy in the combined wave-currents, E_{kwc}. Panels a-e) show current dominant flows (fraction of energy due to waves < 0.25), panels f-j) show wave dominant flows (fraction of energy due to waves > 0.75), and panels k-o) show combined wave-current flows (fraction of energy due to waves is between 0.25 and 0.75).

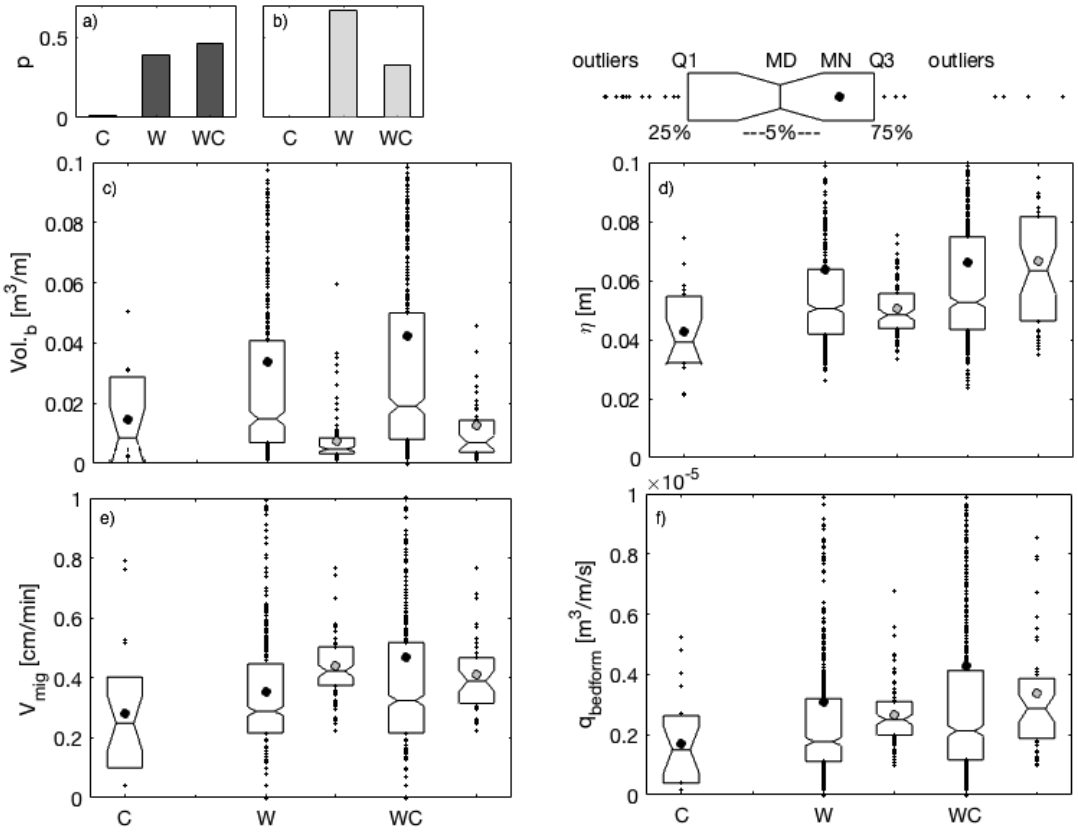

Figure 4.9: Boxplot diagrams showing relevant metrics for calculating sediment flux from bedform migration for current dominant (C), wave dominant (W), and combined wave-current (WC) flows. Panels a,b) show the probability distributions of data falling into C/W/WC dominant flows for S1 and S2. Panel c) shows boxplot diagrams of bedform volume, $Vol._b$. Panel d) shows boxplot diagrams of bedform height, η. Panel e) shows boxplot diagrams of bedform migration rate, $V_{mig.}$ Panel f) shows boxplot diagrams of bedform sediment flux, q_b. The mean point (MN) for site S1 is in black and site S2 is in gray on each boxplot. The key in the upper right hand corner of the figure shows relevant information for understanding a boxplot diagram. A boxplot is a simplistic method to represent a probability distribution. Q1 is the first quartile, and contains 25% of the data, MD is the data median (shown by the center line), MN is the data mean (shown by the dot), and Q3 is the third quartile and contains another 25% of the data. The notch in the middle of the boxplot indicates the 95% confidence interval (shown by –5%– in the key), if the notch of one boxplot does not overlap with the notch of another, then the medians of the boxplots are statistically different with 95% confidence. The points to either side of Q1 and Q3 are outliers, note that all panels do not show the extent of their outliers so that the boxplot distribution is easier to distinguish.

data only ($0.25 < E_{k_w}/E_{k_{wc}} < 0.75$), and for *wave* dominant flows only ($E_{k_w}/E_{k_{wc}} > 0.75$). Data were portioned to demonstrate which models perform best overall, and which perform best in specifically combined flow conditions.

First, we compared the intra-model portioned cases, *all data*, *combined*, and *wave*, to one and other. Interestingly, the *combined* flow case had the highest $rmse/\sigma$ r^2 for each combined flow sediment transport when compared with the *wave* and *all data* cases; showing that even though the model fit the trend of the observations well, it also had the largest deviations of the three cases. The *wave* case had the lowest $rmse/\sigma$ of all cases, but also the lowest r^2; showing the opposite: the model fit the trend of the observations poorly, yet had the smallest deviations.

Most models tend to over predict bedload transport when compared to bedform transport rates (Figure 4.10). The SVR97 model was the only one that had an $rmse/\sigma$ of 1 or less in all three cases (*all data*, *combined*, *wave*). Four models had an r^2 of 0.60 or greater within the *all data* condition (VR04, VR07, SVR97, and HEG06). Within the *combined* subset most models had an r^2 of approximately 0.7, but for the *wave* subset the r^2 dropped to approximately 0.5. Overall, SVR97 (Figure 4.10d) performed the best, followed by the MPM-SC05 (Figure 4.10g). The VR04 and VR07 models also performed well, but the scatter (Figure 4.10a and b) shows that both models largely under predict during periods with the largest transport rates. The under prediction of large flux is a problem for implementation in coastal change models since these large sediment flux events have been shown to highly influence morphologic evolution (de Schipper et al., 2016). SVR97 was formulated as an excess stress model with a drag coefficient that considers both logarithmic boundary layer scaling (for currents) and turbulent kinetic energy produced by the combined wave current boundary layer over a rippled bed (Soulsby, 1997) - building blocks that fully describe conditions of our observations. The model also reasonably well predicted periods with large transport rates when compared with other models (Figure 4.10). MPM-SC05 and HEG06 also qualitatively predict periods with large transport rates. VDA13 is a semi-unsteady state

of the art model that captures the effects of wave skewness on transport, but it has not yet been tested in combined flows over ripples, and from our analysis over predicts transport.

Energetics models have a u^3 relationship for bedload transport, an efficiency of transport parameter (percent of energy in the flow field that is transferred to bed mobility), and a friction coefficient. The energetics model in Hsu et al. (2006) uses wave and current friction coefficients that were 'tuned' for sandbar mobility, where bedload transport is generally sheet flow driven. It is possible that the friction coefficient may be different when applied to bedform migration, either because the flow obstacle geometry is smaller or because the dominant process of bedload transport are different (predominantly sheet flow over the sandbar whereas rolling, jumping, and marching during bedform migration). Since sand ripples/bedforms are smaller than sandbars, and/or the type of bedload transport occurring during bedform migration requires less energy, it is logical for the friction coefficient to decrease to fit the bedload transport due to bedform migration condition. If the current and wave friction coefficients are both decreased by 60% in Hsu et al. (2006), the model $rmse/\sigma$ and r^2 becomes the best compared with the *all data*, *combined*, and *wave* cases (see Figure 4.11 HEG06 (mod.)). This suggests that an energetics approach may be able to model all cases of bedload transport, if the friction coefficients are modified to fit the bedload transport conditions. Figures 4.7 and 4.8 suggests that there was a direct relationship between the bedform sediment flux and the total energy in the flow field, providing foundation to relate flow field energy to the bedload sediment transport rate.

4.5.3 Bedform Migration Direction Compared with MGBNT

Gallagher et al. (1998) and Lacy et al. (2007) show that the bedform migration direction has some relationship with the prevailing flow field using MGBNT from (4.5). The bedform migration direction, $\phi_{mig.}$ and the MGBNT direction ϕ_{MGBNT} are shown in a truncated time series in Figure 4.12b, with the total energy in the flow field plotted for reference in Figure 4.12a. As described in Gallagher et al. (1998) for the MGBNT to accurately describe

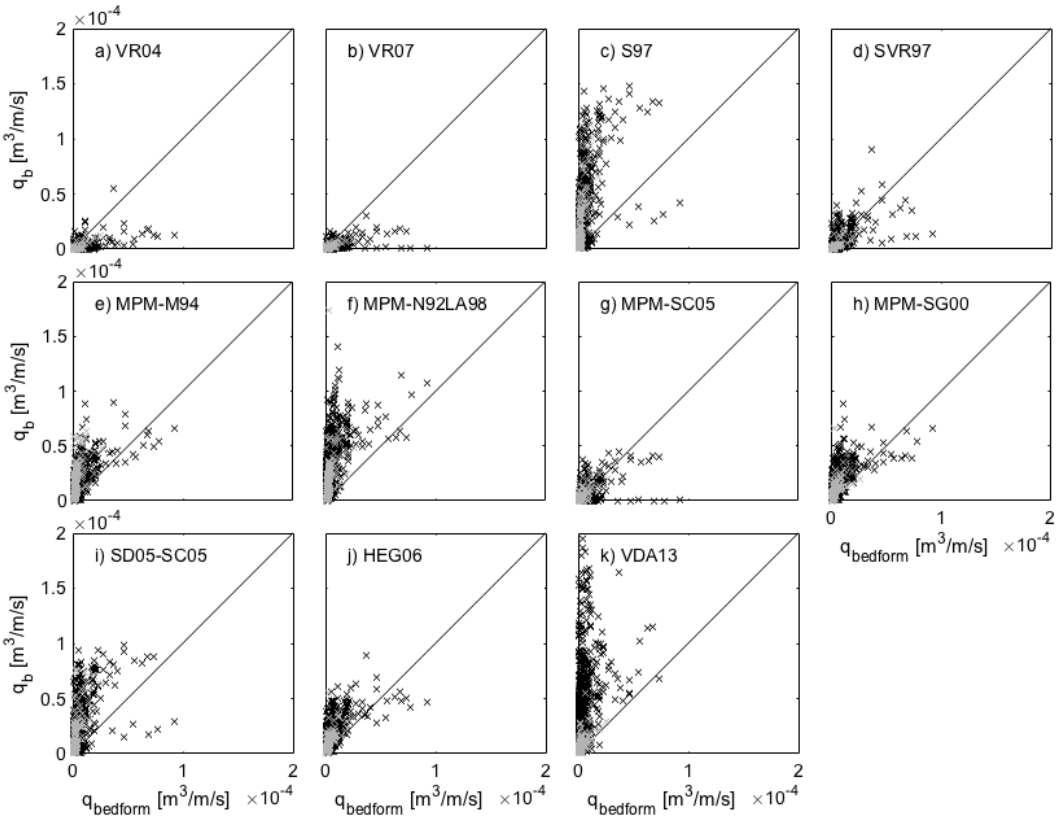

Figure 4.10: Data-model comparisons of bedload sediment flux from bedform migration ($q_{bedform}$) to bedload transport models (q_b). Transport measurements were instantaneous. In black $\times$ are data from S1 and in gray $\circ$ are data from S2. The solid black line is a 1:1 ratio. The following are panels paired with the transport model reference: a) van Rijn et al. (2004) transport model, b) van Rijn (2007) transport model, c) Soulsby (1997) transport model, d) Soulsby-van Rijn transport model published in Soulsby (1997), e) Meyer-Peter and Muller (1948) transport model with Madsen (1994) bed stress model, f) Meyer-Peter and Muller (1948) transport model with Nielsen (1992) wave bed stress model and Li and Amos (1998) current bed stress model, g) Meyer-Peter and Muller (1948) transport model with Soulsby and Clarke (2005) bed stress model, h) Meyer-Peter and Muller (1948) transport model with Styles and Glenn (2000) bed stress model, i) Soulsby and Damgaard (2005) transport model with Soulsby and Clarke (2005) bed stress model, j) Hsu et al. (2006) energetics transport model, and k) van der A et al. (2013) semi-unsteady transport model. For reference, every step increase of 0.1×10^{-4} m^3/m/s is equivalent to an increase of 10 cm^3/m/s.

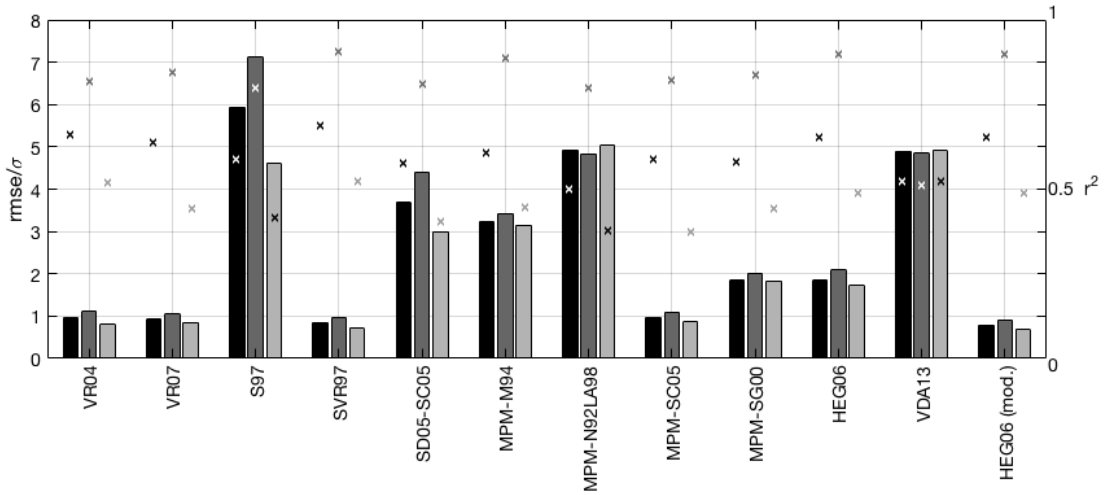

Figure 4.11: Data-model comparison statistics of *rmse* (bars) and r^2 ($\times$) for the bedload sediment transport models shown in Figure 4.10. The black bars show statistics for the entire time series (*all data*) collected at S1 and S2, the dark gray bars show statistics for *combined* flow data only ($E_{k_w}/E_{k_{wc}}$ is between 0.25 and 0.75), and the light gray bars show statistics for *wave* dominant flows only ($E_{k_w}/E_{k_{wc}} > 0.75$). Current dominant flow statistics are not shown because of low data availability. For reference, every step increase of 0.1×10^{-4} $m^3/m/s$ is equivalent to an increase of 10 $cm^3/m/s$.

the bedform orientation, the flow vectors (containing both waves and currents) must be summed over the timescale of bedform development, implying a time dependence between flow direction and bedform migration direction. In Wengrove et al. (2018b), an adjustment time, τ, is suggested as the integration timescale in order to predict bedform growth. The time scale may also be relevant in predicting bedform migration direction. The MGBNT including the variable adjustment timescale from Wengrove et al. (2018b) (red), as well as with a constant adjustment timescale equal to the sampling rate, dt, (blue), is compared with the observed bedform migration direction in Figure 4.12b. The variable adjustment timescale did not significantly increase MGBNT model skill. The main difference was the duration that a migration direction peak persisted (Figure 4.12b). Bedform migration direction was compared to MBGNT direction prediction, ϕ_{MGBNT}, in Figure 4.6c (MGBNT using an adjustment time related to bedform growth had a $r^2 = 0.28$, $rmse = 41°$; MGBNT using an adjustment time of the dt had a $r^2 = 0.24$, $rmse = 40°$). MGBNT did estimate transport direction better than the current or wave directions alone. However, use of the variable adjustment time did not improve prediction. Qualitatively, MGBNT predictions vary with $\phi_{mig.}$, but temporal lags between predictions and measurements reduce correlations. In Lacy et al. (2007) the MGBNT method fits the measured transport direction at times, but also shows significant deviations for approximately 20% of the data shown (see Lacy et al. (2007) Figure 17d).

Overall, the bedform migration direction was difficult to predict in these data. This may be due to the bedform dynamics not considered and the large variability in the flow directions and strengths. The MGBNT method appears to be the best model to describe these bedforms, but the bedform growth timescale may not be characteristic of the change in migration direction. Bedform migration direction leads the bedform orientation direction as well as the bedform growth (Figures 4.2-4.5).

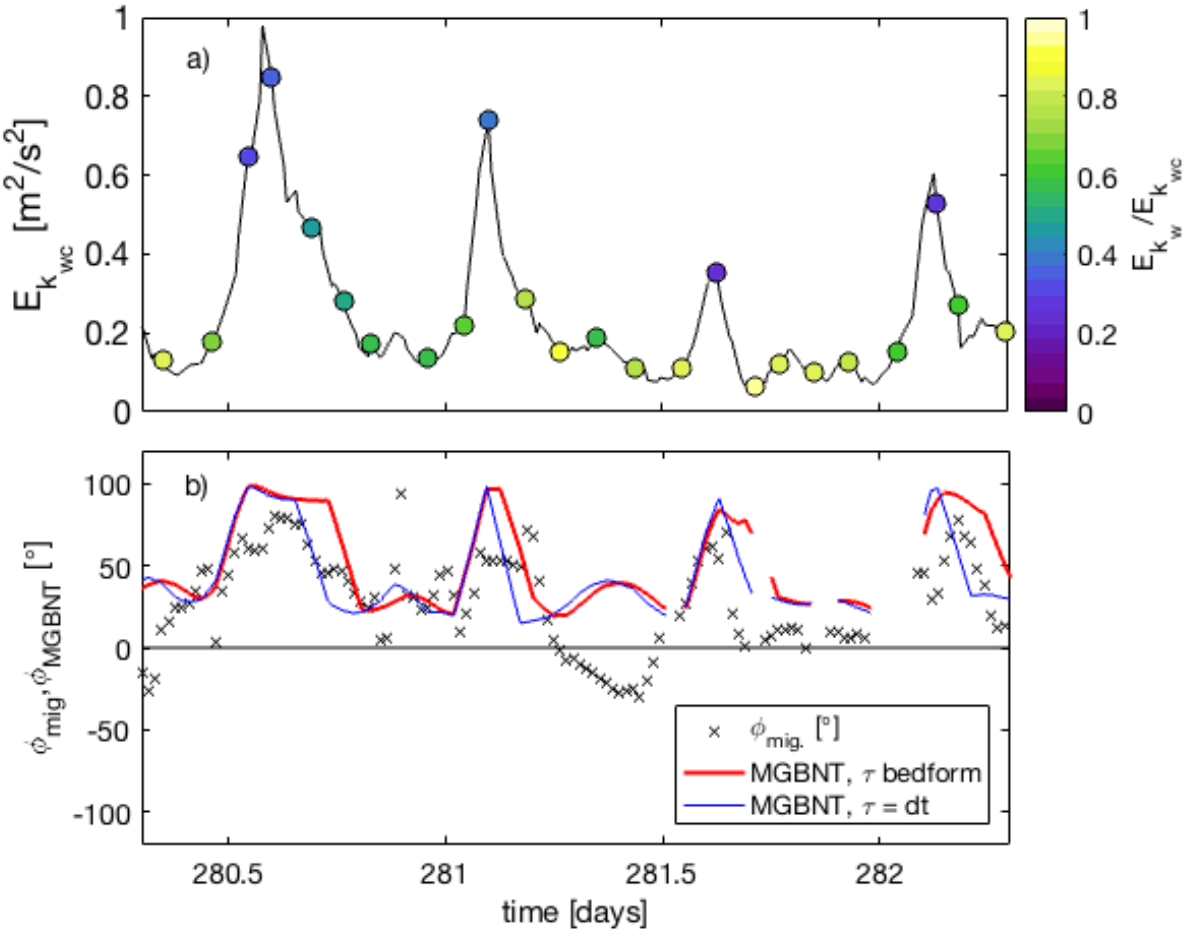

Figure 4.12: Truncated time series showing bedform migration direction, $\phi_{mig.}$, and modeled direction, ϕ_{MGBNT}. Panel a) shows the total kinetic energy, $E_{k_{wc}}$ colored by fraction of energy due to waves, and panel b) shows bedform migration direction, $\phi_{mig.}$, observed ($\times$) and modeled, ϕ_{MGBNT} (red and blue lines). MGBNT was calculated using an adjustment time, τ, related to the bedform growth lag time (red, $r^2 = 0.28$, $rmse = 41°$), and the sampling frequency (blue, $dt = 20$ min., $r^2 = 0.24$, $rmse = 40°$).

4.6 Conclusions

Our effort contributes unique field observations made in the surfzone of bedform response to current dominant, wave dominant, and combined wave-current flow conditions and the relationship to bedload sediment transport are characterized. Increased sediment flux was driven predominantly by increased total kinetic energy in the flow field. Individually, the current dominant, wave dominant, and combined wave current conditions had characteristic differences in bedform shape, migration direction with respect to the overlying flow directions, and mechanisms driving sediment flux:

- During current dominant flow conditions, bedforms were long in wavelength ($\lambda \sim 1$ m), but there was not enough total flow field energy to cause these bedforms to migrate, so the overall sediment flux due to currents alone was low. Additionally, the sediment transport direction visibly led the bedform orientation direction, potentially due to the adjustment time lag of bedform building (Wengrove et al., 2018b).

- During wave dominant flow conditions, the bedform wavelength could vary dependent on the orbital excursion of the waves (in this dataset $\lambda \sim 0.20$ - 1.5 m). When the bedforms began to migrate most rapidly ($V_{mig.} > 1$ cm/min.), the waves were skewed and the sediment transport direction and the bedform orientation were aligned.

- During combined flow conditions the bedforms could get very large in wavelength ($\lambda \sim$ 1 - 2.5 m) and volume. During the highest energy conditions characteristic of strong current velocities and almost equally as strong wave orbital velocities, the combined flow bedforms evolved into lunate megaripples with their migration direction somewhat aligned with the predominant flood tidal current direction. Additionally, combined flow bedforms migrate the most when the sediment transport direction and the bedform orientation were aligned.

Observations show that combined wave-current bedforms had higher sediment flux rates than current dominant and wave dominant bedforms. The sediment flux magnitude associated with bedform mobility within combined wave-current flows was on average 24% (15%) greater in mean (median) than wave dominant flows and 82% (91%) greater in mean (median) than current dominant flows. Suggesting that combined wave-current flows may significantly contribute to sediment transport in nearshore regions.

Eleven existing bedload transport models used in large scale coastal change models were assessed. Each model is specifically formulated to estimate transport and bed stress in combined wave-current flows by either taking a stress ($q_b = f(\tau_b)$) or an energetics ($q_b = f(u)$) based approach. Overall, the Soulsby/van Rijn (Soulsby, 1997) model performed the best with respect to model $rmse/\sigma$ and r^2 when compared with bedload transport rates estimated from observations of bedform migration. The Soulsby/van Rijn bedload transport model was formulated for combined flows over ripples, which was characteristic of the observed conditions. Our observations show that the bedload sediment flux was directly proportional to the total kinetic energy in the flow field, suggesting that an energetics approach to estimate bedload transport may be more representative of the system physics. In the energetics model assessed (Hsu et al. (2006)) the wave and current friction coefficients were based on bedload transport associated with sandbar mobility. If these friction coefficients are decreased to account for differences in length scales (sandbar vs. ripple geometry) and time scales of transport mode (sheet flow for sandbar mobility vs. bedform migration for ripples), then the energetics approach had the lowest $rmse/\sigma$ and the highest r^2 of all the assessed transport models.

Transport direction associated with our very dynamic bedform observations was difficult to predict. The Maximum Gross Bedform Normal Transport (MGBNT) approach predicted overall trends in transport direction, but was not always consistent with the timing of transport direction change. It may be that MGBNT is an appropriate method for transport direction prediction because it does account for overlying flow dynamics; however, an appro-

priate adjustment time for transport direction response in highly dynamic flows needs to be addressed.

Bedload transport in combined wave-current flows is an important mechanism for sediment flux in nearshore environments. These data as well as model-data comparisons show that combined flows may account for more bedload sediment flux than wave dominant and current dominant flows in the nearshore. Our findings suggest that combined wave-current flows should be carefully considered in the sediment transport modules that are implemented in models used to predict coastal morphologic change, and that a transport model with foundation in hydrodynamic kinetic energy may be the most characteristic of system physics.

CHAPTER 5

ESTIMATING BED STRESS IN UNIDIRECTIONAL- AND OSCILLATORY- SEPARATED FLOWS OVER FIXED AND MOBILE BOUNDARIES

5.1 Abstract

Estimating the bed shear stress is non-trivial in non-equilibrium, separated flows over complex boundary geometries, and even more difficult if the bed is mobile. A momentum integral method is presented and evaluated to estimate the bed shear stress these complicated flow conditions with three complementary numerical datasets. The first is a Direct Numerical Simulation (DNS) of unidirectional flow over a fixed-smooth bump, the second is a coupled Large Eddy Simulation (LES) and Discrete Particle Model (DPM) of unidirectional flow over mobile ripples, and the third is a LES-DPM of oscillatory flow over mobile ripples. Analysis shows that the momentum integral method is viable for estimating bed stress in separated flows if at least 90% of the separated region represented within the integral analysis. Additionally, in flows over complicated geometries if data is collected in a cartesian plane and not collected normal to the boundary, error in the estimate of stress is shown to be a function of the boundary gradient angle (e.g. $\alpha = 20^{\circ}$ with error of 17%). However, results show that error in the stress estimate can be reduced by half when dividing the cartesian estimate of stress by $\cos(\alpha)$. Over mobile beds results show that there are important gradients of momentum into the mobilized sediment layer, thereby generating a mobile bed stress, a gradient of stress through the mobile layer, and an immobile bed stress. In unidirectional flow the immobile bed stress is 80% less than the mobile bed stress, and in oscillatory flow the immobile bed stress magnitude is not only reduced, but also the opposite sign of the

mobile bed stress. Results show that the boundary geometry, separation region, and mobile layer all affect the ability for the momentum integral method to estimate stress. However, since the momentum integral method does not make *a-priori* assumptions of boundary layer shape, it is suitable for the aforementioned environments with the proper resolution of the flow field structures.

For reference see: Appendix G, Appendix H, and Appendix I

5.2 Introduction

Bed shear stress is responsible for the transformation of hydrodynamic momentum to the boundary, which can result in drag on the flow field and erosion of the boundary over mobile or deformable beds (Bagnold, 1946). In geophysical flows over sediment beds, an accurate estimation of shear stress applied to the boundary is critical to estimate sediment transport rates and nutrient fluxes (Soulsby, 1997; Boudreau and Jorgensen, 2001; Sherwood et al., 2006). However, geophysical environments are often complicated by non-equilibrium flows, such as separated boundary layers (unidirectional or oscillatory), complicated bottom geometries, and mobile beds, making bed shear stress difficult to estimate (Engelund and Fredsøe, 1982; Fredsøe, 1984; Davies et al., 1988; Van der Werf et al., 2007; Charru et al., 2013).

Shear stress in the nearshore environment is generally partitioned into skin friction-stress, form drag-stress, and entrained sediment-stress; each of these contributions affect the flow field, however only the skin friction-stress affects sediment pickup (Engelund and Fredsøe, 1982; McLean, 1990; Soulsby, 1997; Charru et al., 2013). Here, the skin friction-stress is referred to as the bed stress. There are several methods that are typically used to estimate bed stress in the nearshore environment. The eddy correlation method assumes that in the constant stress layer, the Reynolds stress is closely related to the bottom stress (Trowbridge, 1998). The logarithmic velocity profile method can assume a single logarithmic profile or a dual profile where a logarithmic profile in the upper water column is due to current flow and

is boundary layer matched to a secondary logarithmic boundary layer profile within the wave bottom boundary layer (Grant and Madsen, 1979). The inertial dissipation method relates the spectral amplitude of turbulent kinetic energy in the inertial range to the dissipation rate (Trowbridge and Elgar, 2001), and uses an eddy viscosity to close the Navier-Stokes equations with a drag coefficient or friction factor (Grant and Madsen, 1979; Madsen, 1994; Nielsen, 1992; Li and Amos, 1998; Styles and Glenn, 2000; Soulsby and Clarke, 2005).

As with any model, these methods make assumptions that may not be completely representative of actual flow conditions or boundary layer shape. For example, the traditional logarithmic velocity profile model to approximate the friction velocity is not appropriate in separated and oscillatory flows because of the characteristic velocity phase lead near the boundary (Jonsson and Carlsen, 1976). Additionally, because of flow separations over bedforms and complexities of combined flows in the nearshore region, the constant stress layer or assumptions that the Reynolds stress at an arbitrary water column position is directly related to boundary shear may not be representative approximations (Blondeaux and Vittori, 1990; Fredsøe et al., 1999; Hay et al., 2012b). The boundary layer shape is effectively a result of the transfer of momentum through the water column, influenced by the boundary (Klewicki et al., 2007; Adrian, 2007). With the feedback between the boundary and the flow, the structure of momentum in the boundary layer effectively forces gradients in stress applied to the boundary (Buckles et al., 1984; Nelson et al., 1993; Maab and Schumann, 1996; Chang and Scotti, 2004; Charru et al., 2013). Over complex geometries, such as steps or ripples, *a-priori* assumptions of gradients in the mean and turbulence profiles cannot be made.

More recently, efforts to estimate bed stress have taken an approach to make no *a-priori* assumptions of boundary layer shape. Rodriguez-Abudo and Foster (2014) extended the efforts of Coleman et al. (2008) to yield a momentum balance between the acceleration deficit, form-induced drag and stress gradient as a function of wave phase. Their method averages the continuity and momentum equations in time and space, resulting in the Double-

Averaged Navier Stokes (DANS) equations. This allows for space-averaged stress partitioning that considers the shear contribution due to viscosity plus the phase-dependent momentum contributions due to waves and currents, turbulence, and the presence of bed forms (ripples) (Rodriguez-Abudo and Foster, 2014). Mehdi et al. (2014) extended the efforts of Fukagata et al. (2002) to develop a full momentum integral-based method for steady-unidirectional flow that estimates bed stress by measuring components of the momentum transfer terms in the Navier Stokes equations. The method integrates the streamwise Navier Stokes equation three times to an arbitrary position within the boundary layer. The first integration yields the stress profile, the second the mean velocity profile, and the third the mass flow rate (Mehdi and White, 2011). This method requires a single vertical (boundary-normal) profile of velocity between the boundary and an arbitrary height within the boundary layer to resolve the momentum contributions due to viscosity, the mean flow, and turbulence. The method is mathematically exact and makes assumptions of steady-unidirectional flow with a zero vertical mean (boundary-normal) velocity contribution, and is representative of the flow condition as a function of streamwise position and time. Our effort tests and extends the momentum integral method suggested by Mehdi et al. (2014) to estimate bed stress over fixed-smooth and mobile sediment beds with bedforms in unidirectional- and oscillatory-separated flows.

5.3 Methods

5.3.1 The Momentum Integral Method

The momentum integral method from Mehdi et al. (2014) is presented in time averaged form, relevant to unidirectional flows, and phase averaged form, relevant to oscillatory flows. The method presented is further described in Mehdi and White (2011) and Mehdi et al. (2014).

5.3.1.1 Unidirectional Flow

For two-dimensional, wall-bounded turbulent flow, the horizontal component of the Navier-Stokes equation takes the form

$$\frac{\partial u}{\partial t} + u\frac{\partial u}{\partial x} + w\frac{\partial u}{\partial z} = \frac{1}{\rho}\frac{\partial p}{\partial x} + \nu(\frac{\partial^2 u}{\partial x^2} + \frac{\partial^2 u}{\partial z^2}). \tag{5.1}$$

where u and w are the streamwise and wall-normal velocities, respectively, t is time, p is the pressure, and ρ and ν are the density and kinematic viscosity, respectively. The equation is then Reynolds decomposed ($u_i = \overline{u_i} + u_i'$ and $p = \overline{p} + p'$) and re-written following Mehdi et al. (2014),

$$0 = -\frac{\partial \overline{u}}{\partial t} + \frac{\partial}{\partial z}(\overline{u'w'} - \nu\frac{\partial \overline{u}}{\partial z}) + I + \frac{1}{\rho}\frac{\partial \overline{p}}{\partial x}. \tag{5.2}$$

where, within the parenthesis, are the Reynolds stress contribution and the viscous stress contribution. And,

$$I = \overline{u}\frac{\partial \overline{u}}{\partial x} + \overline{w}\frac{\partial \overline{u}}{\partial z} - \nu\frac{\partial^2 \overline{u}}{\partial x^2} + \frac{\partial \overline{u'^2}}{\partial x}. \tag{5.3}$$

(5.2) and (5.3) are together exact and do not require a boundary layer approximation, and theoretically should hold true close to separation points or even in separated regions (Mehdi et al. 2014).

Following the approach of Fukagata et al. (2002), Mehdi and White (2011), and Mehdi et al. (2014), (5.2) is integrated three times in the vertical (wall-normal) direction. By integrating to an arbitrary height z_t, and replacing ρI by $\frac{\partial \overline{\tau}}{\partial z} - \frac{\partial \overline{p}}{\partial x}$ (where $\frac{\overline{\tau}}{\rho} = \nu\frac{\partial \overline{u}}{\partial z} - \overline{u'w'}$), the following expression is obtained

$$\tau_b = \tau_w = \frac{2\rho}{{z_t}^2}[\nu\int_0^{z_t}\overline{u}dz - \int_0^{z_t}(z_t - z)\overline{u'w'}dz - \frac{1}{2\rho}\int_0^{z_t}(z_t - z)^2\frac{\partial \overline{\tau}}{\partial z}dz], \tag{5.4}$$

where, τ_b is the bed (wall) shear stress and the proceeding terms $(z_t - z)$ are effectively weighting the Reynolds stress and gradient in total stress higher approaching the boundary,

where z_t is the top of the integration extent. The momentum-integral method formulation keeps all wall-normal terms in the horizontal momentum equation, and makes a substitution for the horizontally variable terms. This equation is therefore not dependent upon any quantity variable in the streamwise direction of the flow. Thus, approximation of the wall shear stress is viable with measurements of a vertical (wall-normal) profile of the mean horizontal and vertical velocity and the Reynolds stress.

5.3.1.2 Oscillatory Flow

Under waves there is an additional forcing mechanism due to the oscillatory motion, continuing from (5.1) and similar to a Reynolds decomposition, the velocity and pressure are decomposed into a mean, a phase-dependent and a fluctuating component ($u_i = \overline{u_i} + \widetilde{u_i} + u_i'$ and $p = \overline{p} + \widetilde{p} + p'$) and phase averaging of (5.1) is accomplished by

$$\widetilde{u_i}(\tilde{t}) = \frac{1}{M}\sum_{m=0}^{M} u_i(t + mT) \tag{5.5}$$

where M is the total number of waves and T is the wave period (Anis and Moum, 1995; Rodriguez-Abudo and Foster, 2014).The following is the phase decomposed Reynolds-Averaged Navier-Stokes equation formulated similarly to (5.2), assuming there is not a mean current,

$$0 = \frac{\partial}{\partial z}(\widetilde{u'w'} - \nu\frac{\partial \widetilde{u}}{\partial z} + \widetilde{u}\widetilde{w}) + I + \frac{1}{\rho}\frac{\partial \widetilde{p}}{\partial x}. \tag{5.6}$$

where, within the parenthesis, the first term is the phase averaged Reynolds stress contribution, the second term is the phase averaged viscous stress contribution, and the third term is the contribution from the phase averaged stress imparted from the presence of oscillatory waves. And,

$$I = 2\widetilde{u}\frac{\partial \widetilde{u}}{\partial x} - \nu\frac{\partial^2 \widetilde{u}}{\partial x^2} + \frac{\partial \widetilde{u'^2}}{\partial x}. \tag{5.7}$$

Again, following the approach of Fukagata et al. (2002), Mehdi and White (2011), and Mehdi et al. (2014), (5.6) is integrated three times in the vertical (wall-normal) direction. By

integrating to an arbitrary height z_t, and replacing ρI by $\frac{\partial \widetilde{\tau}}{\partial z} - \frac{\partial \widetilde{p}}{\partial x}$ (where $\frac{\widetilde{\tau}}{\rho} = \nu \frac{\partial \widetilde{u}}{\partial z} - \widetilde{u'w'} - \widetilde{u}\widetilde{w}$), the following expression is obtained

$$\tau_b = \tau_w = \frac{2\rho}{{z_t}^2}[\nu \int_0^{z_t} \widetilde{u} dz - \int_0^{z_t} (z_t - z)\widetilde{u'w'} dz - \int_0^{z_t} (z_t - z)\widetilde{u}\widetilde{w} dz - \frac{1}{2\rho} \int_0^{z_t} (z_t - z)^2 \frac{\partial \widetilde{\tau}}{\partial z} dz]. \quad (5.8)$$

again, τ_b is the bed (wall) shear stress, but (5.8) describes the phase averaged bed shear stress. If (5.8) is then time averaged within irrotational, progressive waves, $\overline{\widetilde{u}\widetilde{w}}$ is zero and (5.8) becomes (5.4).

5.3.2 Considerations when Applying the Momentum Integral Method over Complex Geometries and Mobile Beds

Over mobile sediment boundaries there are often 1) regions of flow separation, 2) complicated bed geometries, and 3) a layer of mobile sediment making estimating bed stress complicated (Penko et al., 2013; Rodriguez-Abudo and Foster, 2014). Each of the three aforementioned difficulties must be carefully considered for the momentum integral method to be used to resolve the bed stress in these conditions.

- Firstly, flow separation can be imposed by an adverse pressure gradient or a shedding vortex on the the lee-side of bedforms in both unidirectional and oscillatory flows (Buckles et al., 1984; Blondeaux and Vittori, 1990; Nelson et al., 1993; Maab and Schumann, 1996; Chang and Scotti, 2004; Charru et al., 2013). The momentum integral method is sensitive to gradients in the boundary-normal velocity profile, suggesting that in order to resolve bed stress under a region of flow separation, the integration limits must pass through the separated region.

- Additionally, complicated bed geometry violates one of the assumptions of the xz plane momentum integral method formulation, the boundary-normal coordinate system is no longer defined by the xyz plane but rather by the *syn* plane (Marquillie et al., 2008).

Where x is along the channel, y is across the channel, and z is the vertical coordinate system, s is then parallel to the curvature of the channel wall, and n is the new vertical coordinate that is defined as perpendicular to the channel wall. The effects of an alternate boundary normal geometry must also be considered.

- Finally, during bedload transport conditions there is a layer of moving sediment that has a gradient in shear stress from the top of the mobile bed down through the mobile layer to the immobile particles (Fredsøe et al., 1992). The mobile sediment layer is considered to be the bedload transport layer, where theoretically the total stress is a function of the skin friction and the drag on the mobile particles,

$$\tau = \tau_{c_f} + nF_d, \tag{5.9}$$

where τ is the total stress on the boundary, τ_{c_f} is the contribution from skin friction imparted on the immobile boundary to the total stress, and nF_d are the number of moving particles and the drag force on each single particle (Fredsøe et al., 1992). The momentum integral method and with integration extents from to the top of the mobile layer to somewhere in the boundary layer may effectively yield the mobile bed stress ($\tau \sim \tau_m$), but not necessarily the immobile bed stress ($\tau_{c_f} \sim \tau_b$), suggesting that τ_m may not account for the gradient in stress within the mobile layer.

Once bed stress is estimated, to relate it to sediment transport regime, a non-dimensional bed stress is defined by the Shields parameter (Shields, 1936).

$$\theta = \frac{\tau_b}{\rho(s-1)gd_{50}}. \tag{5.10}$$

where τ_b is the bed stress, ρ is the fluid density, s is the specific weight of the sediment, g is the acceleration due to gravity, and d_{50} is the median sediment grain size. The Shields parameter is used to classify regimes of sediment transport and ranges from 0.03-0.06 for

incipient motion of sediment (things are starting to move), 0.1-0.8 for bedform formation and migration, and 0.8+ for sheet flow sediment transport (a lot of sediment is moving and bedforms are being washed out) (Soulsby, 1997).

5.3.3 Numerics

We used three simulation frameworks to address the momentum integral method's ability to estimate stress in the aforementioned complex flow conditions, as well as evaluate the physics of the mobile layer of transport. A Direct Numerical Simulation (DNS) of unidirectional flow within a channel contraction with flow separation forced by an adverse pressure gradient bump was used to understand limitations of the momentum integral method to resolve stress in separated flows over a fixed boundary and to understand the effects of an xyz coordinate system to a syn coordinate system on the momentum integral method (Marquillie et al., 2008). DNS directly models the Navier-Stokes equations. The flow Reynolds number of the simulation used in this work was 600. The simulation was done in air. The simulation was designed to have a very thin region of detachment (separation) on the lee side of the bump.

Additionally, a coupled Large Eddy Simulation (LES) and Discrete Particle Model (DPM) was used to model the fluid-particle interaction and flow flow over mobile ripples (in unidirectional flow and in oscillatory flow) to understand the effects of estimating bed stress over and within mobile beds in separated flows (Hagan, 2018). LES resolves the large scales of the flows, but the sub-grid scales are modeled. The Reynolds number for the LES-DPM model is 200. The simulation was done in water. The particles have a diameter of 1 mm, a density of $\rho_s = 2500$ kg/m^3, and a specific gravity of $s = 2.5$. The mobile boundary was configured to a field of 6 sinusoidal ripples shaped with height of 20 mm and wavelength of 100 mm and the particles were gravity settled, once the simulation started, particles were free to move and change position with the flow field forcing.

5.4 Results and Discussion

5.4.1 Unidirectional and separated flow over a fixed boundary

The DNS of unidirectional flow within a channel contraction was used to understand both the influence of flow separation as well as the effects of the coordinate system following the traditional xz cartesian plane to the sn boundary normal plane over a fixed boundary. The flow is moving from left to right and accelerates over the crest of the imposed channel contraction bump, creating the highest velocities at the crest (Figure 5.1a). Downstream of the crest there is a region of separated flow, in the region there is a sign change in both the Reynolds stress ($-\rho\overline{u\prime w\prime}$) and vorticity ($\omega_y$) (Figure 5.1b and c), and this region corresponds to an area of negative wall stress (Figure 5.2).

Additionally, the flow reversal causes restructuring of the momentum in the boundary layer as seen through the vertical spatial gradient of the Reynolds stress ($d\overline{u\prime w\prime}/dz$) (Klewicki et al., 2007; Adrian, 2007). Over a flat-smooth boundary, there is traditionally a high amplitude but short range momentum source ($+d\overline{u\prime w\prime}/dz$) by the wall, and an adjacent small amplitude but long range momentum sink (-$d\overline{u\prime w\prime}/dz$) reaching toward the boundary layer thickness (as seen in Figure 5.1d profile at $x = 0.75$). As the channel contraction is reached the adverse pressure gradient begins to shift the momentum structure, forcing both the source of momentum by the wall and the adjacent sink to increase amplitude and create another low amplitude momentum source region as the boundary layer thickness is reached (Figure 5.1d profile at $x = 4 - 5.5$). The trend continues as the flow reaches the separation point, the momentum source by the wall and adjacent sink have large increases in amplitude, and the sink region continues to persist and lengthen approaching the end of the downstream side of the channel contraction while the source region is squeezed toward the wall. The integration of $d\overline{u\prime w\prime}/dz$ from the wall over the full boundary layer thickness at any point along the channel contraction is zero showing that there is a balance of momentum in the boundary layer profile.

Differences between the xz (blue profiles) and the sn (red profiles) coordinate system is apparent in the $d\overline{u\prime w\prime}/dz$ (Figure 5.1d). The amplitude of the momentum source and sink regions are the most striking difference between the two coordinate systems, but with a closer look, between $x = 2.4 - 6$ in the adverse pressure gradient region as the crest of the bump is approached and passed, but before the flow separates, the sign of the momentum region is opposite between the xy and sn profiles (where there is a momentum source in one there is a sink in the other and visa versa). The apparent differences in the spatial Reynolds stress gradients does affect the ability for the momentum integral method to approximate the wall stress (Figure 5.2). The bed stress is approximated using (5.4) with both coordinate systems, replacing the gradients in x and z with s and n for both space and velocity fields. While the momentum integral method approximation of τ_w with the sn coordinate system has less than 3% error within the adverse pressure gradient and separated regions of the flow over the bump, the xz coordinate system approaches 17% error at the steepest boundary gradient of just over 20°.

Realistically, using the momentum integral method with a sn coordinate system is difficult, especially with non-numerical data. It is possible to reduce the error by half if the xy approximation of bed stress using (5.4) is divided by the $\cos(\alpha)$, where α is the boundary gradient in degrees (Figure 5.2). Where, a simple correction for the estimate of the wall stress ($\tau_{w_{xz}}$) after using the momentum integral method in the xz plane is

$$\tau_b = \tau_w = \frac{\tau_{w_{xz}}}{\cos(\alpha)}. \tag{5.11}$$

Aside from complications with coordinate systems over variable bed geometries, in many field or laboratory measurement campaigns, it is difficult to capture the full boundary layer separation region in the lee-side vortex. The momentum integral method weights gradients in the contributing terms higher as the boundary is approached. Since there is a change in gradient near the boundary within separated flows and adverse pressure gradients, it is worth while to understand how much estimates of stress may be affected by missing the flow

reversal in the integration limits of the momentum integral method (Figure 5.3). The region of flow separation the DNS channel contraction over the bump was 1 cm thick (Marquillie et al., 2008). Figure 5.3a shows a zoomed in area of the flow separation, as well as the τ_w estimate from the momentum integral method using the uncorrected xz and sn coordinate systems with the integration limit near the wall moving progressively further away. Within the xz coordinate system, in order to capture the negative wall stress within the separated flow region with less than 35% error the lower integration limit should capture at least 90% of the flow separation. If $\tau_{w_{xz}}$ is corrected using (5.11) the error is reduced by approximately half, but this correction is not able to capture the sign reversal on its own. Within the sn coordinate system the overall error associated with the lower integration limit moving further from the boundary is reduced; still, at least 70% of the flow separation should be captured to have less than 35% error. The DNS was designed to have a very thin region of flow separation (Marquillie et al., 2008), which is not characteristic of all separated flows, but we believe that the statistics of the needed % of the separated region required to resolve the wall stress is still valid to other separated flows. Over the fixed boundary, results show that both the coordinate system and the lower integration limits of (5.4) affect the ability for the momentum integral method to approximate the wall stress.

5.4.2 Unidirectional and separated flow over a mobile bed

The mobile bed LES-DPM cases provide interesting insight into the dynamics of the mobile sediment layer. Since the bedforms in the unidirectional LES-DPM simulation are not meant to force a channel contraction, there is not as much flow acceleration over the crests of the ripples when compared with the DNS channel simulation (Figure 5.4, set up similar to Figure 5.1). The Reynolds stress and vorticity panels show that the region of flow separation is thicker on the lee side of the bedforms compared to the fixed boundary DNS channel simulations as well (Figure 5.4b and c).

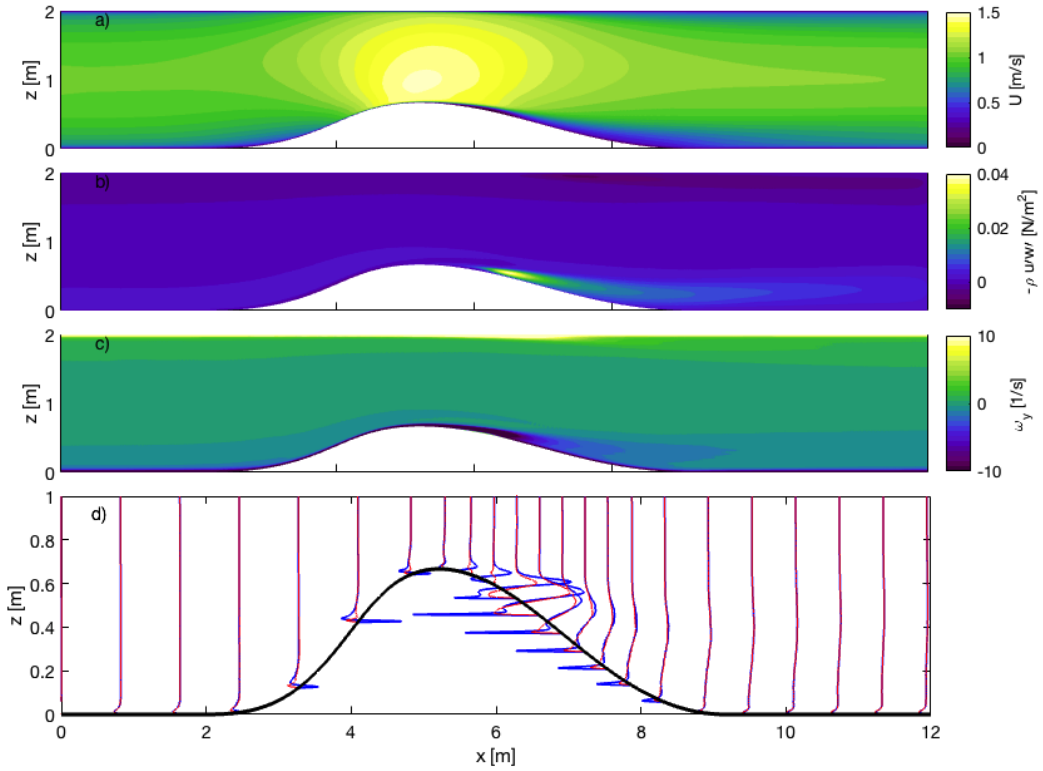

Figure 5.1: Statistics of DNS of a channel contraction over a fixed, smooth bump. Panel a) shows the mean horizontal velocity (U), with positive defined moving from left to right. Panel b) shows the Reynolds stress ($-\rho\overline{u'w'}$). Panel c) shows the vorticity (ω_y). Panel d) shows the vertical gradient of the Reynolds stress ($d\overline{u'w'}/dz$), with the profiles defined following the bump boundary outlined in black. The positive direction for the profile is defined to the left. The blue line is the gradient taken in the xz plane and the red line is the gradient taken in the sn plane, but plotted in the xz plane for purpose of comparison.

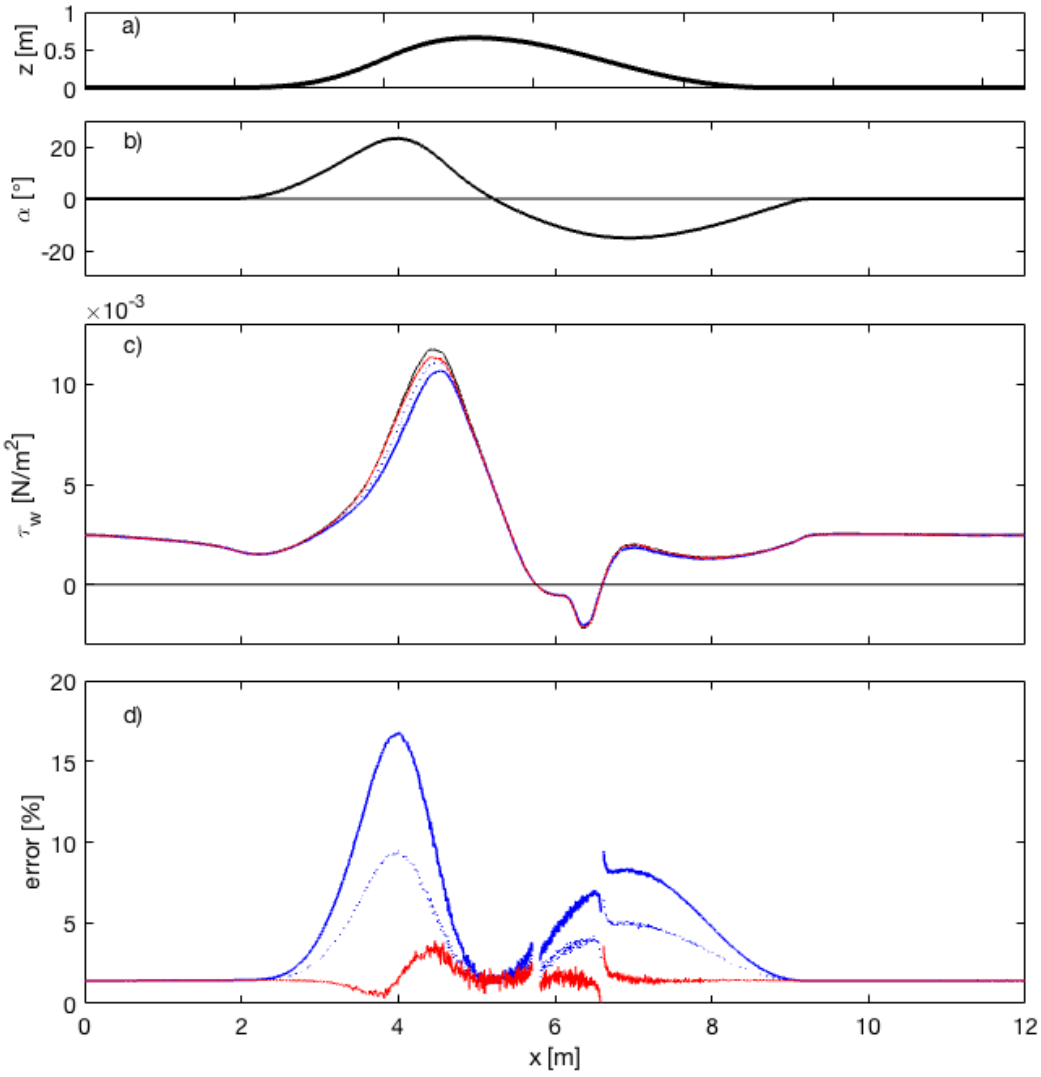

Figure 5.2: Wall stress estimates from the DNS of a channel contraction over a fixed, smooth bump. Panel a) shows the bump profile. Panel b) shows the bump gradient (α) in degrees. Panel c) shows τ_w from the model (black), in the xz coordinate system (solid blue), in the sn coordinate system (solid red), and the corrected xz coordinate system for bed angle using (5.11) (dotted blue). Panel d) shows the percent difference of each estimate from the model τ_w with the same texture and color from (c).

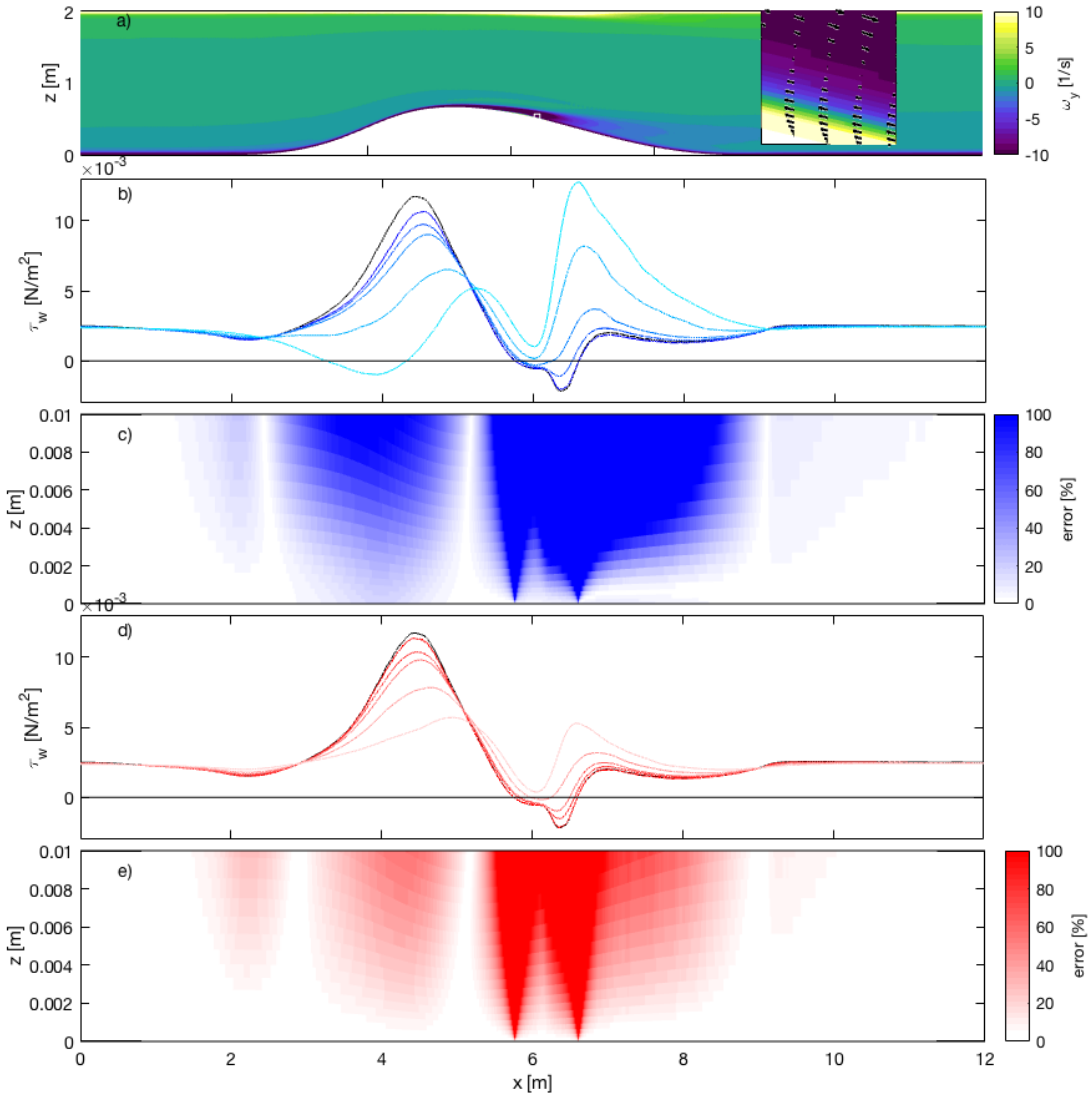

Figure 5.3: Wall stress estimates from the DNS of a channel contraction over a fixed, smooth bump. Panel a) shows the bump vorticity, with inset showing the vorticity and velocity vectors in the separated flow highlighted by white outline on larger view. Panel b) and c) show τ_w and percent error with increasing lower integration limit away from the boundary, respectively. In (b) the black line is τ_w from the DNS, and the blue lines are integrating to the boundary (darkest blue) and then moving incrementally away from the boundary (toward lighter blue), the lower integration limits are as follows [0 mm, 1 mm, 2 mm, 5 mm, 10 mm]. Panels d) and e) are the same as (b and c) but for an *sn* coordinate system in shades of red. Percent error is shown up to 100%, however there were greater errors, so dark red or blue could be error of 100% or greater.

In each panel the solid line represents the mobile bed level, while the dashed line represents the immobile bed level. The immobile bed level was determined by integrating the profiles of Reynolds stress gradients until the integration yielded a value of $1\text{x}10^{-6}$, or approximately zero (Figure 5.4d). It is clear from Figure 5.4d that the exchange of momentum into the bed stops at the immobile layer. In regions where there are no particles moving then the mobile and immobile bed levels should be the same. Additionally, similar trends in momentum source and sink amplitude and spread through the boundary layer can be observed moving from the stoss side to the lee side of the ripple and especially into the region of flow separation with large increases in the amplitude of the momentum source and sink as seen with the channel contraction DNS simulation. However, the lee side separation over the ripples does affect the structure and amplitude of momentum ascending up the stoss side of the adjacent downstream ripple. Importantly, it is apparent that there is a positive gradient of momentum within the mobile layer along the crest of each ripple, which influences the magnitude of the mobile and immobile layer bed stress.

To estimate bed stress the time averaged momentum integral method was used, (5.4). The bed stress over the mobile boundary shows positive stress over the stoss side and crest of the ripple and then in the region of flow separation τ_b is negative. A direct estimate of stress from the LES-DPM was made using the total stress ($\tau_b = \mu \partial u/\partial z - \rho\overline{u\prime w\prime}$) at the mobile and immobile bed elevations, additionally the momentum integral method was used to estimate the bed stress by assuming a lower integration limit of the mobile or immobile bed interface. When integrating into the mobile layer, the density and dynamic viscosity of the fluid-particle mixture changes with percent of the mixture occupied by particles. There is some discrepancy between the direct estimate of stress from the LES-DPM simulation at the mobile and immobile layers, mainly within the trough of the ripple; however, general patterns of stress are the same between the direct estimate of stress and the momentum integral method estimate of stress (Figure 5.5). In either case, the bed stress is reduced by 80% through the mobile layer to the immobile layer (Figure 5.5b). In reference to (5.9),

results would suggest that the drag from the interaction between moving particles accounts for 80% of the additional stress at the mobile bed compared to the immobile bed.

Results are put in terms of the Shields parameter in order to observe the regions of the bedform where sediment is expected to be in motion ($\theta > \theta_{crit}$). The estimates of bed stress at the mobile interface suggest that only particles at the crest of the ripple have imposed stress greater than the critical threshold ($\theta_{crit} = 0.035$ for 1 mm particles), supported by the simulation results (Figure 5.5c). However, particles at the immobile bed interface are not in motion, consistent with the assumption of an immobile layer.

5.4.3 Oscillatory and separated flow over a mobile bed

The mobile bed LES-DPM with oscillatory flow forcing demonstrates that gradients in boundary layer momentum are important even within the mobile bed layer. The Reynolds stress and vorticity panels show that there are regions of flow separation on both sides of the ripple, where there is an eddy shed off the crest of the ripple that rotates clockwise with negative vorticity when the flow oscillation is in positive phases (or moving from left to right), and rotates counter-clockwise with positive vorticity when the flow oscillation is in negative phases (or moving from right to left) (Figure 5.6). Just under these main regions of vorticity, there is a region of counter rotation sitting right at the mobile bed interface (Figure 5.6b and c). The pockets of Reynolds stress momentum that are adjacent to the bed have a sign opposite to the main eddy vorticity envelope and do not seem to be influenced by the counter rotation envelope right at the mobile bed interface. Since the Reynolds stress is much larger than the viscous stress at the mobile bed interface the total stress at the mobile bed is negative on the left side of the ripple and positive on the right side of the ripple, which is counter to theory and simulations of bedforms over a smooth-fixed boundary (Jacobsen and Fredsøe, 2013; Charru et al., 2013).

However, recall that fluid is able to flow through the mobile layer. In each panel the solid line represents the mobile bed level, while the dashed line represents the immobile bed level.

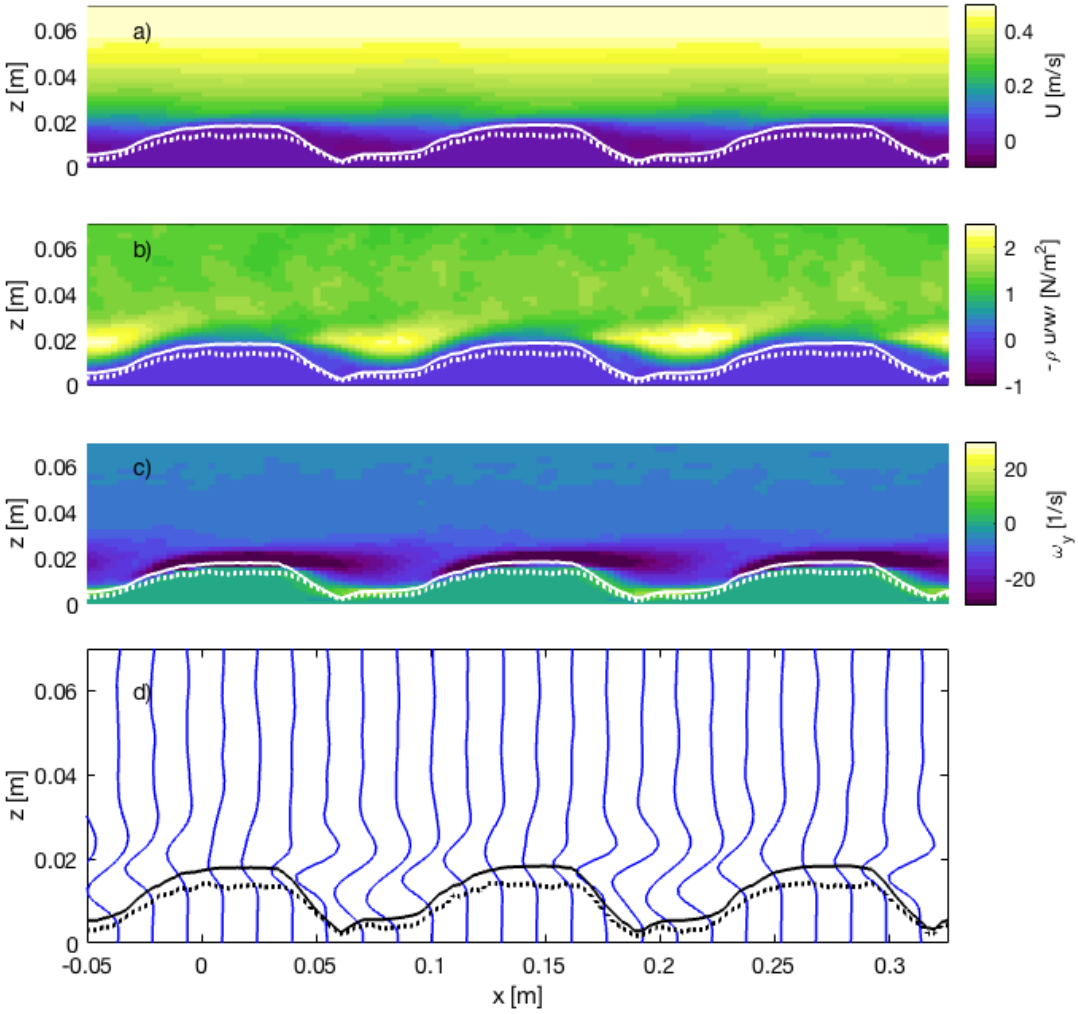

Figure 5.4: Statistics of LES-DPM of unidirectional flow over a mobile rippled bed. The solid white line in panels (a-c) is the mobile bed layer, and the dotted white line is the immobile bed layer. Panel a) shows the mean horizontal velocity (U), with positive defined moving from left to right. Panel b) shows the Reynolds stress ($-\rho\overline{u\prime w\prime}$). Panel c) shows the vorticity (ω_y). Panel d) shows the vertical gradient of the Reynolds stress ($d\overline{u\prime w\prime}/dz$), with the profiles defined following the ripple mobile bed layer (solid black) and immobile bed (dotted black) lines. The positive direction for the profile is defined to the left. The blue line is the gradient taken in the xy plane. Bed statistics are averaged in the across channel direction (y, over 64 slices).

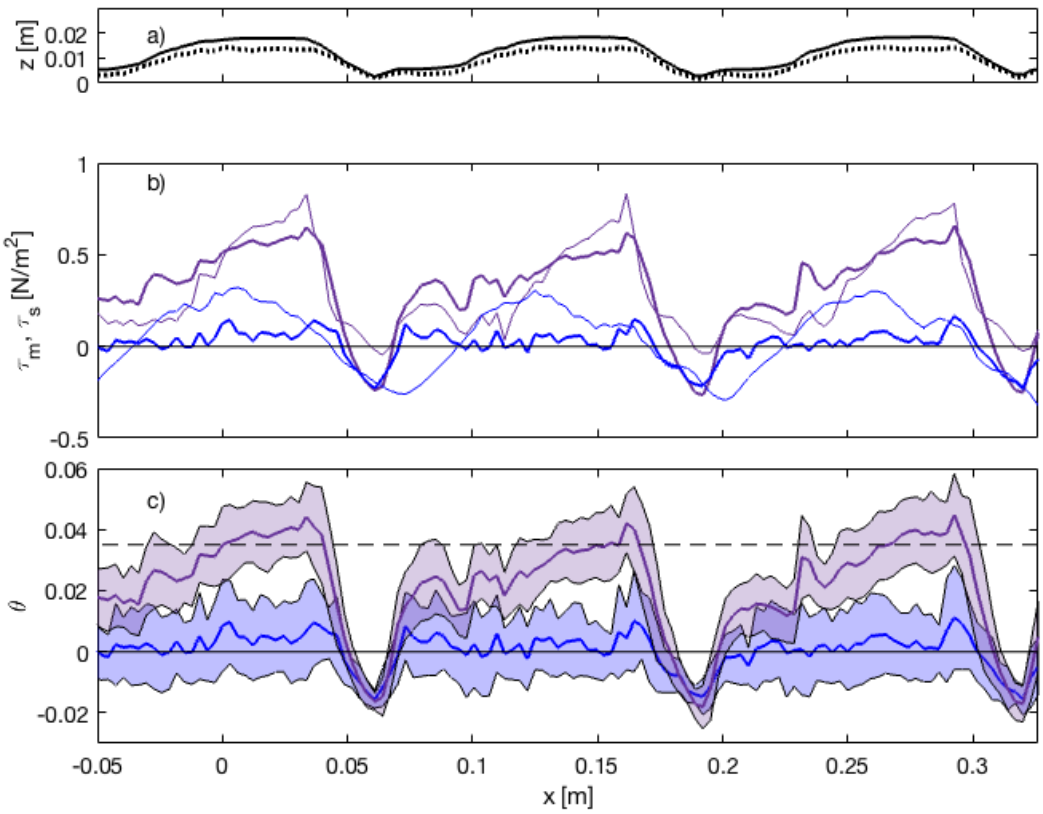

Figure 5.5: Bed stress estimates from the LES-DPM of unidirectional flow over a mobile rippled bed. Panel a) shows the ripple mobile bed layer (solid black) and immobile bed (dotted black) lines. Panel b) shows the mobile bed stress (τ_m, purple) and immobile bed stress (τ_b, blue) estimated from the total stress at the bed position in the model (thin lines) and from the momentum integral method (thick lines). Panel c) shows the corresponding Shields parameter for the momentum integral method of the mobile (purple) and immobile (blue) bed stress, the solid line is the mean over the across channel width, and the shaded regions are $\pm$ one standard deviation. The dotted black line is the critical threshold for motion of particles 1 mm in diameter ($\theta = 0.035$).

The immobile bed level was again determined by integrating the profiles of Reynolds stress gradients ($d\overline{u'w'}/dy$) until the integration yielded a value of value of $\pm$1x10^{-}6, or approximately zero (Figure 5.6d). It is clear from Figure 5.6d that the exchange of momentum into the bed stops at the immobile layer because the profile gradients have little to no change below the immobile bed level. Generally the $d\overline{u'w'}/dy$ source and sink regions are symmetric about the ripple crest, with the left side of the ripple showing a momentum source above the mobile layer and a momentum sink into the bed, and visa versa on the right side of the ripple. Importantly, there is an inflection point in the gradient of momentum at the mobile bed interface along both the lee and stoss sides of the ripple. The inflection point signifies a change in the momentum gradient in the mobile layer, and therefore influences the magnitude and sign of the mobile layer and immobile contour bed stress. The inflection point in $d\overline{u'w'}/dy$ occurs in the region of opposite vorticity at the mobile bed interface. Recall, from the DNS over the bump analysis, that in order to correctly model the sign of the bed stress in separated flows, the lower integration limit must encompass approximately 90% of the separated region, so even though the change in vorticity occurs at and into the mobile bed interface, estimating the bed stress requires an integration into the mobile bed.

To estimate bed stress the time average of the phase averaged momentum integral method was used. The bed stress at the mobile boundary was found to be negative on the left side of the ripple and positive on the right side (Figure 5.7, but at the immobile bed contour, the bed stress was found to be positive on the left side of the ripple and negative on the right (consistent with theory and simulations over fixed-smooth beds (Charru et al., 2013)). These estimates are consistent in sign and somewhat consistent in magnitude with a direct estimate of stress from the LES-DPM made using the total stress ($\tau_b = \mu\partial u/\partial z - \rho\overline{u\prime w\prime}$) at the mobile and immobile bed elevations. At the crest of the ripple at the immobile bed contour, there is a stress discontinuity, this may be due to the waggling of the ripple crest with the passing of the flow oscillations and is also consistent with the simulations of Jacobsen and Fredsøe (2013) over a smooth fixed boundary (Figure 5.5). Again, sediment-fluid mixture density

and viscosity is accounted for within the stress estimates. Overall, the bed stress magnitude, again is reduced by 80% through the mobile layer to the immobile layer (Figure 5.5b), but the more striking inconsistency is the sign change in bed stress between the mobile and immobile contours due to the momentum gradient change within the mobile layer.

With a simple thought experiment, if a ripple is considered in oscillatory flow with the positive direction defined to the right, if the bed stress imposed on the ripple is negative on the left side of the crest and positive on the right side of the crest (as seen in the oscillatory flow at the mobile bed interface) then the ripple should flatten over time. If flattening does not occur (as in the LES-DPM oscillatory flow case), then a balancing stress must be maintaining the ripple shape, and in this case this may be the stress through the mobile layer and at the immobile contour. The thought experiment alone demonstrates that the mobile layer dynamics are important to understanding mechanisms for sediment transport.

Finally, results are put in terms of the Shields parameter in order to observe the regions of the bedform where sediment is expected to be in motion ($\theta > \theta_{crit}$). The estimates of bed stress at the mobile interface suggest that only particles at the crest of the ripple have imposed stress greater than the critical threshold ($\theta_{crit} = \pm 0.035$ for 1 mm particles), supported by the simulation results (Figure 5.7c). However, particles at the immobile bed interface are not in motion, consistent with the assumption of an immobile layer.

5.5 Conclusions

Estimating bed stress in unsteady, oscillatory, non-equilibrium flows is difficult over a fixed and smooth boundary alone, not to mention adding in the additional complexity of a non-uniform geometry and a mobile boundary. The momentum integral method is a tool that can be used to estimate bed stress when high resolution measurements or numerics of the boundary layer dynamics are available. Here, we showed that the momentum integral method is viable for estimating bed stress in separated flows, in flows over complicated geometries, and even over mobile beds. The momentum integral method may be the most accurate method

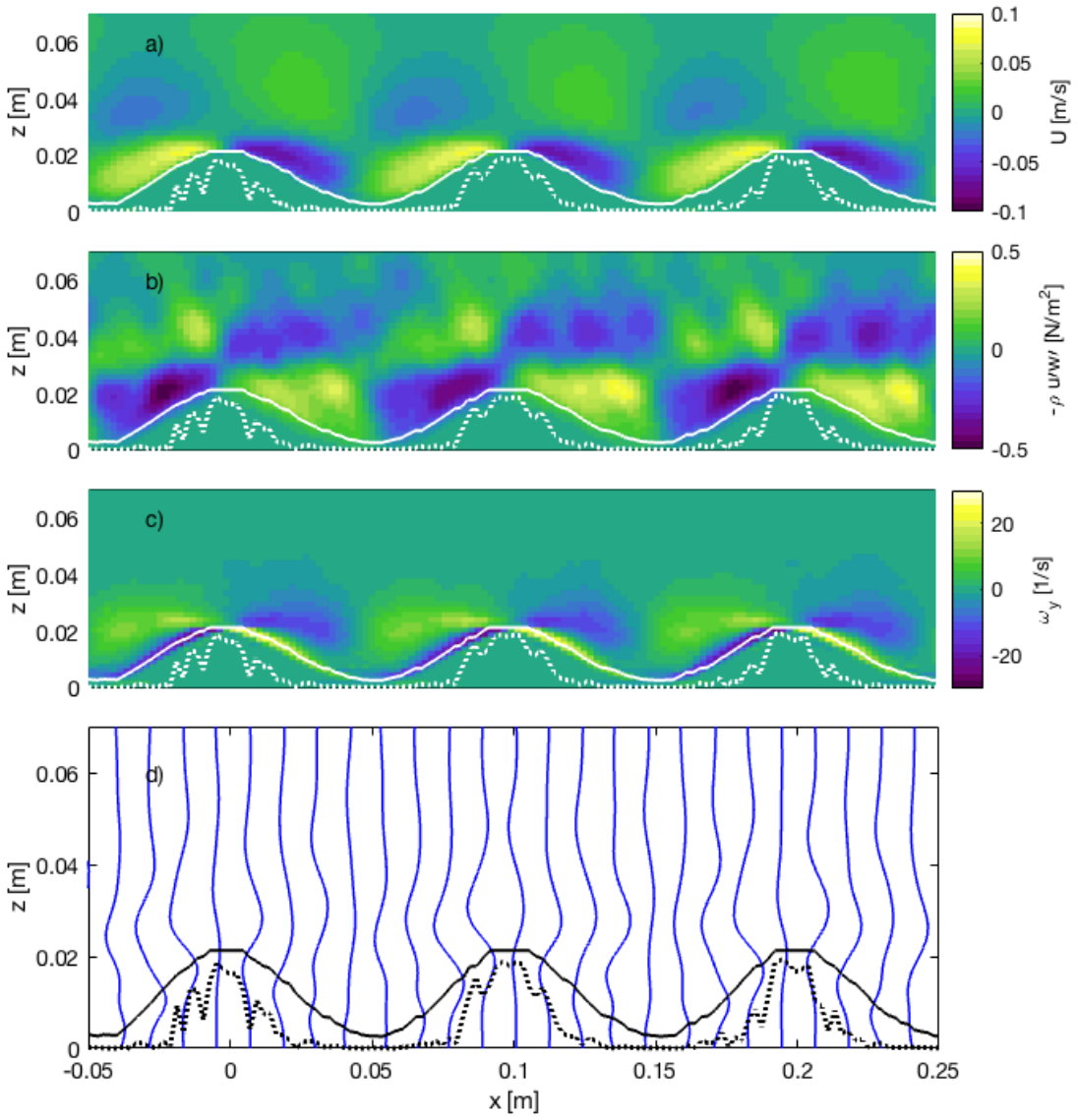

Figure 5.6: Statistics of LES-DPM of oscillatory flow over a mobile rippled bed. The solid white line in panels (a-c) is the mobile bed layer, and the dotted white line is the immobile bed layer. Panel a) shows the mean horizontal velocity (U, with positive defined moving from left to right. Panel b) shows the Reynolds stress ($-\rho\overline{u\prime w\prime}$). Panel c) shows the vorticity (ω_y). Panel d) shows the vertical gradient of the Reynolds stress ($d\overline{u\prime w\prime}/dz$), with the profiles defined following the ripple mobile bed layer (solid black) and immobile bed (dotted black) lines. The positive direction for the profile is defined to the left. The blue line is the gradient taken in the xy plane. Bed statistics are averaged in the across channel direction (y, over 64 slices).

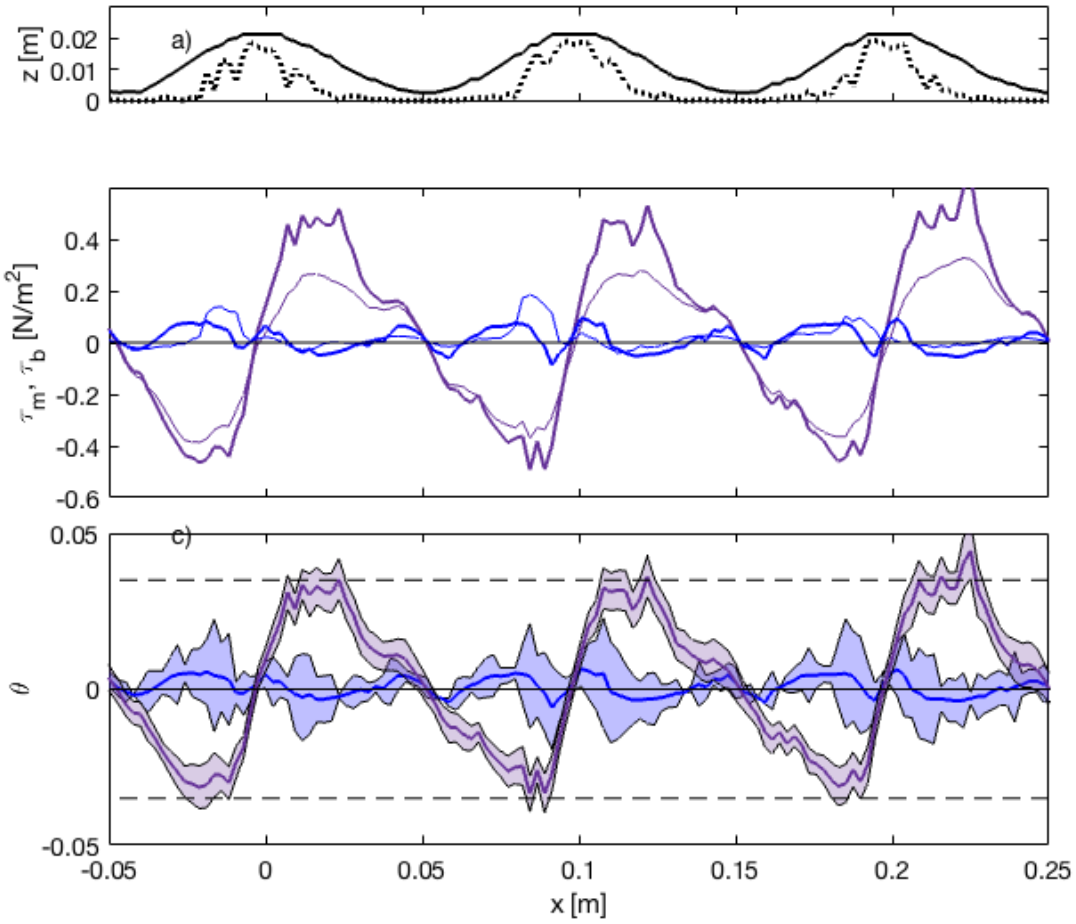

Figure 5.7: Bed stress estimates from the LES-DPM of oscillatory flow over a mobile rippled bed. Panel a) shows the ripple mobile bed layer (solid black) and immobile bed (dotted black) lines. Panel b) shows the mobile bed stress (τ_m, purple) and immobile bed stress (τ_b, blue) estimated from the total stress at the bed position in the model (thin lines) and from the momentum integral method (thick lines). Panel c) shows the corresponding Shields parameter for the momentum integral method of the mobile (purple) and immobile (blue) bed stress, the solid line is the mean over the across channel width, and the shaded regions are $\pm$ one standard deviation. The dotted black line is the critical threshold for motion of particles 1 mm in diameter ($\theta = \pm 0.035$).

to estimate bed stress at the top of the mobile layer existing. Since it is a mathematically exact method to estimate bed stress, it is the most representative of the Navier-Stokes equations that are assumed to be representative of fluid motion. With a constitutive relationship for dynamics through the mobile sediment layer, the momentum integral method could also be viable to estimate bed stress at the immobile sediment interface.

However, the limitations of the method must be considered.

- Firstly, the momentum integral method assumes a boundary normal coordinate system. Over a complicated geometry, the assumed xyz coordinate system of may measurement campaigns and numerics does introduce error into the estimate of bed/wall stress as a function of the boundary gradient angle. Due to the impracticality of collecting data in a *syn* coordinate system, we proposed a simple correction of dividing the xz stress estimate by the $\cos(\alpha)$, which reduces associated error by half.

- Additionally, in order to resolve the bed stress in regions of flow separation the lower integration limit must include at least 90 percent of the region of separated flow. For various flows, the physical unit of the region is variable. If the proper gradients are not included, the bed stress could be not only have errors in magnitude, but also in sign.

- Over mobile boundaries in unidirectional flow, the integral method can be used to estimate the mobile bed stress, and with the LES-DPM numerics of this work from Hagan (2018), the immobile bed stress was also estimated. The thickness of the mobile layer is variable with the flow field. The mobile bed stress was shown to be up to 80% larger in magnitude than the immobile bed stress in unidirectional flow. In oscillatory flow the mobile bed stress was shown to be up to 80% larger in magnitude than the immobile bed stress and opposite in sign, due to the momentum gradients in the mobile layer. In laboratory or field data, when it is not possible to measure flow velocities within the mobile layer, a future constitutive relationship should be developed

to accurately account for both the change in magnitude an direction of the bed stress through the mobile or fluidized sediment layer.

Overall, the momentum integral method does not make assumptions of boundary layer shape, which makes it a robust method to estimate bed/wall stress under separated, non-equilibrium, and oscillatory flows when sufficient information of the boundary layer gradients are measured or simulated. Not only do results show the benefits and limitations of the momentum integral method, but they also highlight the complexities of estimating bed stress over mobile boundaries in the laboratory and especially in the field. Within the sediment transport community, many have relied upon measurements of the overlying flow field to estimate bed stress, however, our results show that resolution of the momentum gradients in the mobile layer are just as important in order to accurately represent system physics.

CHAPTER 6

CONCLUSIONS AND FUTURE WORK

The study of bedform mechanics has now been investigated for more than a century, with the first known contributions pondering the ripple mark formation dating back to the end of the 19th century (Darwin, 1883; Ayrton, 1910). This dissertation continued in the vein of investigation of ripple growth and decay and transport dynamics; however, to begin, gave a justification for the many detailed studies of ripple evolution and growth. For the first time, observations showed evidence for ripples significantly contributing to the larger morphologic evolution. In fact, it may be that ripples are driving variability in coastal change and could be a mechanism for persistent system patterns of net erosion and accretion. Specifically, analysis of nearshore bedform migration gradients demonstrated that large scale morphologic evolution (e.g. sandbars) was consistent with the sediment divergence associated with small scale ripple adjustment. At its heart, demonstrating a connection between the large scale morphologic change and small scale volumetric sediment flux advocates for detailed analysis of the mobility, growth, and sediment flux mechanics of ripples and megaripples that aggregate on our coastlines, inlets, and rivers. This dissertation additionally contributes new knowledge related to the mechanics of bedform growth/decay and mobility in current dominant, wave dominant, and combined wave-current flows from the bulk multi-ripple scale to the detailed intra-ripple scale.

Fundamentally, on the multi-ripple scale, the bedforms are shown to have an adjustment lag time for both reorientation as well as growth or decay with onset of changes in the flow field direction and flow kinetic energy magnitude. With respect to bedform volume, in wave dominant flows the bedforms can adjust and come into equilibrium with the flow field within as little as 20 minutes. However, with current dominant and combined wave-current

flows, the addition of the mean flow increases the bedform adjustment time to multiple hours. The sediment continuity equation was used to model this time varying volumetric growth/decay without any model parameters, and is potentially applicable to prediction of roughness variability in space and time over the range of scales present in a full coastal system. Additionally, this dissertation showed that regardless of the flow dominance (current, wave, combined wave-current), the bedload sediment transport associated with bedform migration can be robustly estimated using the kinetic energy contained in the flow field. On the intra-ripple scale, dynamics of bedload transport were investigated in both mean flows and oscillatory flows at the mobile sediment layer of the ripple crest. The mobile bed layer was shown to have a decay in applied stress through the full mobile layer depth with up to an 80% reduction in shear stress between the top of the mobile layer and the immobile layer. Where, under oscillatory flow, the sign of the applied shear stress at the mobile surface was found to be opposite that at the immobile interface. At some of the smallest scales of sediment transport, findings have implications for understanding the mechanisms of bedload transport under waves and currents as well as the shear structure within the mobile layer.

Practically, this dissertation contributes the building blocks for a bulk model to estimate roughness and bedload transport on the multi-ripple scale, as well as a detailed validation study for the momentum integral method to estimate the intra-ripple bed shear stress on the intra-ripple scale. The former uses the proposed time integrated sediment continuity equation model to predict volumetric roughness and the energetics based bedload transport model of Bowen (1980) modified for combined flows by Hsu et al. (2006) with this dissertation's proposed modification to the drag coefficient to model transport from small-scale bedform migration. Together the formulations only need input of bulk flow statistics, such as the mean current and the orbital velocity of the waves to predict volumetric roughness and bedload transport in current dominant, wave dominant, and combined wave-current flows. Such a model is highly applicable to measurement campaigns and numerical simulations that do not resolve the boundary layer dynamics in detail. However, if physical measurements

or numerical simulations of detailed boundary layer dynamics are available, the momentum integral method of Mehdi et al. (2014) was also evaluated and extended to estimate bed stress over curved surfaces, in separated flows, and over mobile boundaries in both mean and oscillatory flows. The momentum integral method does not make assumptions of boundary layer shape. With the technique, a direct estimate of the bed stress at the mobile layer can then be used to estimate transport regime and rates. Both techniques are applicable to current dominant, wave dominant, and combined wave-current flows on the appropriate scale.

Both the fundamental and the practical findings suggest an approach to estimating the bedform roughness and the bedload sediment flux in nearshore environment based in the flow field kinetic energy. Results show that accurately estimating bed stress with physical measurements or numerics is non-trivial. Many methods used to approximate the bed stress in the complicated flows of the coastal nearshore make assumptions of boundary layer gradients that may not be physically representative of the flow forcing, especially true in large scale field measurement campaigns and within coastal change prediction models. Thereby, this dissertation proposed using the flow field kinetic energy, $Q_b = f(E_{k_{wc}})$, in place of $Q_b = f(\tau_b)$ to estimate sediment transport rates and thereby bedform roughness volumes. $Q_b = f(E_{k_{wc}})$ may be more robust and suitable to natural and numerical environments where detailed boundary layer measurements are unavailable.

There are several avenues for proposed future work. First, the volumetric roughness sediment continuity model and the modified energetics bedload transport model can be connected to form a unified predictive roughness-bedload transport model that is applicable in current dominant, wave dominant, and combined wave-current flows. The proposed addition will use stability theory to estimate bedform height (roughness height) from volumetric growth. Secondly, the sediment continuity volumetric growth analysis may be extended to predict bedform growth and change at much larger scales, for aid in navigation and large scale sediment transport studies within coastal inlets. Thirdly, related to the observations

of the dynamics of the mobile bedload transport layer, a constitutive relationship can be developed so that the momentum integral method can be used robustly in field and laboratory environments to estimate the bed stress at both the mobile bed and the immobile bed interface. In this dissertation, numerical simulations were able to resolve flow through the mobile layer to investigate momentum dynamics, but flow through natural sediment particles cannot be measured with existing techniques, supporting the need for development of a constitutive relationship to estimate bed shear stress through the mobile layer. Additionally, existing knowledge in the sediment transport community attributes the deviation between the mobile and immobile bed stress to be to inter-granular interactions; however, there is a persisting question as to whether it is the mobile or immobile stress estimate that should be used within transport models - signifying an additional avenue of investigation. Finally, although this dissertation provided evidence that ripples contribute to the evolution of larger morphologies, the mechanisms for contribution and loss of sediments are unknown. Investigation into the sediment transport processes that force the observed convergence and divergence gradients in sediment transport is another avenue of future research.

In summary, this dissertation contributes unique field observations of bedform response to combined wave-current forcing in the surfzone. Observational results show that bedforms have a time varying response to the overlying flow field forcing and their roughness and transport rates can be predicted using the flow kinetic energy. At finer detail, results show that the mobile bedload transport layer has its own characteristic momentum gradients and the consequence of these mobile layer gradients to bedload transport is an area of future research. Additionally, with basis in the observations of bedform response to combined wave-current flows, the structure for a combined roughness and bedload transport model is outlined supporting that at the large scale Q_b is better estimated as a $f(E_{k_{wc}})$ instead of a $f(\tau_b)$, this connection will be extended in future work. Finally, results suggest that sand ripples may significantly contribute to the evolution of larger morphologic features, which justifies continued efforts into the investigation of the dynamics of the ripple mark.

BIBLIOGRAPHY

Aagaard, T., R. Davidson-Arnott, B. Greenwood, and J. Nielsen
2004. Sediment supply from shore face to dunes: linking sediment transport measurements and long-term morphological evolution. *Geomorphology*, 60.

Aagaard, T., B. Greenwood, and J. Nielsen
2000. Bed level changes and megaripple migration on a barred beach. *Journal of Coastal Research*.

Adrian, R. J.
2007. Hairpin vortex organization in wall turbulence. *Physics of Fluids*.

Alamo, J. C. and J. Jimenez
2003. Spectra of very large anisotropic scales in turbulent channels. *Physics of Fluids Letters*, 15(6).

Allen, J. and J. Collision
1974. The superimposition and classification of dunes formed by unidirectional aqueous flows. *Sedimentary Geology*, 12(169–178).

Amos, C., A. Bowen, D. Huntley, J. Judge, and M. Li
1999. Ripple migration and sand transport under quasi-orthogonal combined flows on the scotian shelf. *J. Coastal Research*, 15(1).

Anis, A. and J. N. Moum
1995. Surface wave-turbulence intractions: Scaling near the sea surface. *American Meteorological Society*.

Arolla, S. K. and O. Desjardins
2014. Transport modeling of sedimenting particles in a turbulent pipe flow using euler-lagrange large eddy simulation. *International Journal of Multiphase Flow*.

Austin, M. J., G. Masselink, T. J. O'Hare, and P. E. Russell
2007. Relaxation time effects of wave ripples on tidal beaches. *Geophysical Research Letters*, 34.

Ayrton, H.
1910. The origin and growth of ripple-mark. *Proceedings of the Royal Society of London. Series A, Mathematical and Physical Character*, 84(571):285–310.

Bagnold, R.
1966. An approach to the sediment transport problem from general physics. Prof. Paper 422-1, U.S.G.S.

Bagnold, R. A.
1946. Motion of waves in shallow water, interaction between waves and sand bottoms. *Proceedings of the Royal Society of London. Series A, Mathematical and Physical Sciences*, 187(1008):1–18.

Bailard, J. and D. Inman
1981. An energetics bedload transport model for a plane sloping beach: local transport. *J. Geophys. Res.*, 86:2035–2043.

Becker, J. M., Y. L. Firing, J. Aucan, R. Holman, M. Merrifield, and G. Pawlak
2007. Video-based observations of nearshore sand ripples and ripple migration. *Journal of Geophysical Research*, 112.

Blondeaux, P. and G. Vittori
1990. Vorticity dynamics in an oscillatory flow over a rippled bed. *J. Fluid Mech.*, 226.

Bosboom, J., A. Reniers, and A. Luijendijk
2014. On the perception of morphodynamic model skill. *Coastal Engineering*, Pp. 112–125.

Boudreau, B. and B. Jorgensen, eds.
2001. *The Benthic Boundary Layer*. Oxford University Press.

Bowen, A. J.
1980. Simple models of nearshore sedimentation; beach profiles and longshore bars. *The Coastline of Canada*.

Buckles, J., T. J. Hanratty, and R. J. Adrian
1984. Turbulent flow over large-amplitude wavy surfaces. *J. Fluid Mech.*

Carlson, E. M.
2015. Identification of ripple migration mechanisms on a natural sand bed. Master's thesis, University of New Hampshire.

Catano-Lopera, Y. A. and M. H. Garcia
2006. Geometry and migration characteristics of bedforms under waves and currents part 2: Ripples superimposed on sandwaves. *Coastal Engineering*, 53.

CEM
2002. The coastal engineering manual. Technical report.

Chang, Y. S. and A. Scotti
2004. Modeling unsteady turbulent flow over ripples: Reynolds-averaged navier-stokes equations (rans) versus large-eddy simulation (les). *J. Geophys. Res.*, 109:1–16.

Charru, F., B. Andreotti, and P. Claudin
2013. Sand ripples and dunes. *Annu. Rev. Fluid Mech.*

Clarke, L. and B. Warner
2004. Tidally modulated occurrences of megaripples in a saturated surf zone. *Journal of Geophysical Research*, 109.

Clifton, H. E. and J. R. Dingler
1984. Wave-formed structures and paleoenvironmental reconstruction. *Marine Geology*, 60:165–198.

Coleman, S. E., V. I. Nikora, and T. Schlicke
2008. Spatially-averaged oscillatory flow over a rough bed. *Acta Geophysica*, 56(3):698–733.

Craig, R., C. Loadman, B. Clement, P. Rusello, and E. Seigel
2010. Characterization and testing of a new bistatic profiling acoustic doppler velocimeter: The vectrino-ii. *Proc. of the IEE/OES/CWTM Tenth Working COnference on Current Measurement Technology.*

Dalrymple, R. W.
1984. Morphology and internal structure of sand waves in the bay of fundy. *Sedimentology*, 31.

Dalrymple, R. W. and R. N. Rhodes
1995. *Geomorphology and Sedementology of Estuaries. Developments in Sedimentology 53*, chapter Estuarine Dunes and Bars. Elsevier Science.

Darwin, G. H.
1883. On the formation of ripple-mark in sand. *Proceedings of the Royal Society of London*, 36:18–43.

Davies, A. G., R. L. Soulsby, and H. L. King
1988. A numerical model of the combined wave and current bottom boundary layer. *Journal of Geophysical Research*, 93(C1).

Davies, A. G. and C. Villaret
1999. Eulerian drift induced by progressive waves above rippled and very rough beds. *Journal of Geophysical Research*, 104(C1).

Davis, J. P., D. J. Walker, M. Townsend, and I. R. Young
2004. Wave-formed sediment ripples: Transient analysis of ripple spectral development. *J. Geophys. Res.*, 109(C07020, doi:10.1029/2004JC002307):1–15.

de Schipper, M. A., S. de Vries, G. Ruessink, R. C. de Zeeuw, J. Rutten, C. van Gelder-Mass, and M. J. F. Stive
2016. Initial spreading of a mega feeder nourishment: Observations of the sand engine pilot project. *Coastal Engineering*, 111:23–38.

de Zeeuw, R., M. A. de Schipper, P. K. Toonon, and B. van der Valk
2016. Morfologische ontwikkeling van de zandmotor pilot in de periode 2 tot 4,5 jaar na aanleg. Technical report, Shore Monitoring and Research.

Dean, R. G.
1991. Equilibrium beach profiles: Characteristics and applications. *Journal of Coastal Research*, 7(1).

Dietrich, W. E. and J. D. Smith
1984. Bed load transport in a river meander. *Water Resources Research*, 20(10).

DoD
2018. Department of defense climate-related risk to dod infrastructure initial vulnerability assessment survey (slvas) report. Technical report, Office of the Under Secretary of the Defense for Acquisition, Technology, and Logistics.

Doucette, J. S. and T. O'Donoghue
2006. Response of sand ripples to change in oscillatory flow. *Sedimentology*, 53:581–596.

Elko, N., F. Feddersen, D. Foster, C. Hapke, J. McNinch, R. Mulligan, H. T. Ozkan-Haller, N. Plant, and B. Raubenheimer
2014. The future of nearshore processes research. Technical report, The Nearshore Processes Community.

Engelund, F. and J. Fredsøe
1982. Sediment ripples and dunes. *Annu. Rev. Fluid Mech.*, 14.

Fredsøe, J.
1984. Turbulent boundary layer in wave-current motion. *J. Hydraul. Eng.*, 110(8).

Fredsøe, J., K. H. Andersen, and B. Mutlu Sumer
1999. Wave plus current over a ripple-covered bed. *Coast. Eng.*, 38:177–221.

Fredsøe, J. and R. Deigaard
1992. *Mechanics of coastal sediment transport.* World Scientific.

Fredsøe, J., B. M. Sumer, and M. M. Arnskov
1992. Time scale for wave/current scour below pipelines. *Int. J. Offshore Polar*, 2(1).

Fukagata, K., K. Iwamoto, and N. Kasagi
2002. Contribution of reynolds stress distribution to the skin friction in wall-bounded flows. *Phys. Fluids*, 14.

Gallagher, E. L.
2003. A note on megaripples in the surf zone: evidence for their relation to ready flow dunes. *Marine Geology*, 193:171–176.

Gallagher, E. L., S. Elgar, and E. B. Thornton
1998. Megaripple migration in a natural surf zone. *Letters to Nature*, 394.

Ganju, N. E. and C. R. Sherwood
2010. Effect of roughness formulation on the performance of a coupled wave, hydrodynamic, and sediment transport model. *Ocean Modeling*, 33:299–313.

Grant, W. D. and O. S. Madsen
1979. Combined wave and current interaction with a rough bottom. *J. Geophys. Res.*, 84(C4):1797–1808.

Hagan, D. H.
2018. *Large Eddy Simulation of Oscillatory Flow over a Mobile Rippled Bed using an Euler-Lagrange Approach*. PhD thesis, University of Vermont.

Hay, A., L. Zedel, R. Cheel, and J. Dillon
2012a. Observations of the vertical structure of turbulent oscillatory boundary layers above fixed roughness beds using a prototype wide-band coherent doppler profiler: 2. turbulence and stress. *Journal of Geophysical Research*, (in press).

Hay, A. E. and T. Mudge
2005. Principal bed states during sandyduck97: Occurrence, spectral anisotropy, and the bed state storm cycle. *J. Geophys. Res.*, 110(C03013, doi:10.1029/2004JC002451):1–18.

Hay, A. E., L. Zedel, R. Cheel, and J. Dillon
2012b. On the vertical and temporal structure of flow and stress within the turbulent oscillatory boundary layer above evolving ripples. *Continental Shelf Res.*, 46.

Hsu, T.-J., S. Elgar, and R. T. Guza
2006. Wave-induced sediment transport and onshore sandbar migration. *Coastal Engineering*, 53:817–824.

Imagenex
2011. *Imagenex Model 881A Digital Multi-Frequency Imaging Sonar*. Imagenex.

IPCC
2014. Climate change 2014 synthesis report. Technical report, Intergovernmental Panel on Climate Change.

Jacobsen, N. G. and J. Fredsøe
2013. Relevance of an intra-wave morphodynamic description of vortex. *Coastal Dynamics 2013 Conference Proceedings*.

Jaffe, B. E. and D. M. Rubin
1996. Using nonlinear forecasting to learn the magnitude and phasing of time-varying sediment suspension in the surf zone. *J. Geophys. Res.*, 101(C6):14283–14296.

Jonsson, I. and N. Carlsen
1976. Experimental and theoretical investigations in an oscillatory turbulent boundary layer. *Journal of Hydraulic Research*, 14(1):45–60.

Julien, P. Y.
1998. *Erosion and Sedimentation*. Cambridge University Press.

Klewicki, J., P. Fife, T. Wei, and P. McMurtry
2007. A physical model of the turbulent boundary layer constant with mean momentum balance structure. *Philosophical Transactions of the Royal Society A Mathematical, Physical and Engineering Sciences*.

Koca, K., C. Noss, C. Anklanger, A. Brand, and A. Lorke
2017. Performance of the vectrino profiler at the sediment-water interface. *Journal of Hydraulic Research*.

Lacy, J. R., D. M. Rubin, H. Ikeda, K. Mokudai, and D. M. Hanes
2007. Bed forms created by simulated waves and currents in a large flume. *Journal of Geophysical Research*, 112.

Lanckriet, T., J. Puleo, G. Masselink, I. Turner, D. Conley, C. Blenkinsopp, and P. Russell
2012. Field measurements of sheet flow sediment transport in the swash zone. *Coastal Engineering Proceedings*.

Larsen, S. M., B. Greenwood, and R. Aagaard
2015. Observations of megaripples in the surf zone. *Marine Geology*, 364.

Lefebvre, A., V. Ernstsen, and C. Winter
2013. Estimation of roughness lengths and flow separation over compound bedforms in a natural-tidal inlet. *Continental Shelf Research*.

Lesser, G. R., J. A. Roelvink, T. M. van Kester, and G. S. Stelling
2004. Development and validation of a three-dimensional morphological model. *Coastal Engineering*, 51:883–915.

Li, M. Z. and C. L. Amos
1998. Predicting ripple geometry and bed roughness under combined waves and currents in a continental shelf enviornment. *Continental Shelf Research*, 18:941–970.

Ludka, B., R. Guza, W. O'Reilly, and M. Yates
2015. Field evidence of beach profile evolution toward equilibrium. *Journal of Geophysical Research*.

Maab, C. and U. Schumann
1996. Direct numerical simulation of separated turbulent flow over a wavy boundary. *In: Herschel E.H. (els) Flow Simulation with High-Performance Computers. Notes on Numerical Fluid Mechanics (NNFM)*, 48.

Madsen, O.
1994. Spectral wave-current bottom boundary layer flows. *Proc. Coast. Eng. 24th Intn'l Conf.*, 1:384–398.

Madsen, O., Y. Poon, and H. Graber
1988. Spectral wave attenuation by bottom friction: Theory. *Coastal Engineering, Proceedings of the 21st Conference Am. Soc. Civ. Eng. New York*, 1.

Madsen, O. S. and W. D. Grant
1976. Quantitative description of sediment transport by waves. In *Fifteenth International Coastal Engineering Conference*, volume 2, Pp. 1093–1112. American Society of Civil Engineers.

Maier, I. and A. E. Hay
2009. Occurrence and orientation of an orbital ripples in near-shore sands. *Journal of Geophysical Research*, 114.

Marquillie, M., J.-P. Laval, and R. Dolganov
2008. Direct numerical simulation of a separated channel flow with a smooth profile. *Physics of Fluids*.

McLean, S. R.
1990. The stability of ripples and dunes. *Earth-Science Reviews*, 29.

Mehdi, F., T. G. Johansson, C. M. White, and J. W. Naughton
2014. On determining wall shear stress in spatially developing two-dimensional wall-bounded flows. *Exp. Fluids*, 55(1656).

Mehdi, F. and C. M. White
2011. Integral form of the skin friction coefficient suitable for experimental data. *Exp. Fluids*, 50:43–51.

Meyer-Peter, E. and R. Muller
1948. Formulas for bed-load transport. In *Report on the Second Meeting of the International Association for Hydraulic Structures Research*, Pp. 39–64, Stockholm.

Murray, A. B., E. Lazarus, A. Ashton, A. Baas, G. Coco, T. Coulthard, M. Fonstand, P. Haff, D. McNamara, C. Paola, J. Pelletier, and L. Reinhardt
2009. Geomorphology, complexity, and the emerging science of the earth's surface. *Geomorphology*, 103:456–505.

Nelson, J. M., S. R. McLean, and S. R. Wolfe
1993. Mean flow and turbulence fields over two-dimensional bed forms. *Water Resources Research*.

Nelson, T. R. and G. Voulgaris
2015. A spectral model for estimating temporal and spatial evolution of rippled seabeds. *Ocean Dynamics*, 65:155–171.

Ngusaru, A. S. and A. E. Hay
2004. Cross-shore migration of lunate megaripples during duck94. *J. Geophys. Res.*, 109.

Nielsen, P.
1992. *Coastal bottom boundary layers and sediment transport*. World Scientific.

Nielsen, P. and D. Callaghan
2003. Shear stress and sediment transport calculations for sheet flow under waves. *Coastal Engineering*, 47(3):347–354.

NortekAS
2013. *Nortek Comprehensive Manual*. NortekAS.

Omidyeganeh, M. and U. Piomelli
2011. Large-eddy simulation of two-dimensional dunes in a steady, unidirectional flow. *Journal of Turbulence*, 12(42):1–31.

Passchier, S. and M. G. Kleinhans
2005. Observations of sand waves, megaripples, and hummocks in the dutch coastal area and their relation to currents and combined flow conditions. *J. Geophys. Res.*, 110.

Pendleton, L. and J. Kildow
2006. The non-market value of beach recreation in california. *Shore and Beach*, 74(2).

Penko, A., J. Calantoni, and B. T. Hefner
2017. Modeling and observations of sand ripple formation and evolution during trex13. *Journal of Oceanic Engineering*.

Penko, A. M., J. Calantoni, S. Rodriguez-Abudo, D. L. Foster, and D. N. Slinn
2013. Three-dimensional mixture simulations of flow over dynamic rippled beds. *Journal of Geophysical Research - Oceans*.

Perillo, M. M., J. L. Best, M. Yokokawa, T. Sekiguchi, T. Takagawa, and M. H. Garcia
2014. A unified model for bedform development and equilibrium under unidirectional, oscillatory and combined flows. *Sedimentology*, 61.

Perkovic, D., T. Lippmann, and S. Frasier
2009. Longshore surface currents measured by doppler radar and video piv techniques. *Geoscience and Remote Sensing, IEEE Transactions on*, 47(8):2787–2800.

Price, T. and G. Ruessink
2011. State dynamics of a double sandbar system. *Continental Shelf Research*, 31.

Radermacher, M., M. A. de Schipper, C. Swinkels, J. H. MacMahan, and A. J. Reniers
2017. Tidal flow separation at protruding beach nourishments. *Journal of Geophysical Research: Oceans*, 122:63–79.

Rodriguez-Abudo, S. A. and D. L. Foster
2014. Unsteady stress partitioning and momentum transfer in the wave bottom boundary layer over movable rippled beds. *J. Geophysical Research Oceans*, 119:8530–8551.

Roelvink, D. J. A., A. van Dongeren, R. T. McCall, and B. Hoonhout
2015. Beach technical reference: Kingsway release. User manual, Daltares.

Ruggiero, P., G. M. Kaminsky, G. Gelfenbaum, and N. Cohn
2016. Morphodydnamics of prograding beaches: A synthesis of seasonal- to century-scale observations of the columbia river littoral cell. *Marine Geology*, 376.

Saulter, A. N., P. E. Russell, E. L. Gallagher, and J. R. Miles
2003. Observations of bed level change in a saturated surf zone. *Journal of Geophysical Research*, 108(C4).

SeaBeam
2000. Multibeam sonar theory of operation. Technical report, L3 Communications of SeaBeam Instruments.

Sherman, D. J.
1995. Problems of scale in the modeling and interpretation of coastal dunes. *Marine Geology*, 124.

Sherwood, C. R., J. R. Lacy, and G. Voulgaris
2006. Shea velocity estimates on the inner shelf off grays harbor, washington, usa. *Continental Shelf Res.*, 26.

Shields, A.
1936. Anwendung der anhlichkeitsmechanik und turbulenzforschung auf die geschiebebewegung. *Mitt. Preuss Versuchsanstalt fur Wassebaur und Schiffbau*, 26.

Sleath, J. F. A.
1999. Conditions for plug formation in oscillatory flow. *Cont. Shelf Res.*, 19:1643–1664.

Smith, D. and J. F. A. Sleath
2005. Transient ripples in oscillatory flows. *Cont. Shelf Res.*, 25:485–501.

Smyth, C. and M. Li
2005. Wave-current bedform scales, orientation, and migration on sable island bank. *J. Geophys. Res.*, 110.

Soulsby, R. and S. Clarke
2005. Bed shear-stresses under combined waves and currents on smooth and rough beds. Report TR 137, HR Wallingford.

Soulsby, R. L.
1997. *Dynamics of marine sands*, 1st edition. Thomas Telford Services, Ltd.

Soulsby, R. L. and J. S. Damgaard
2005. Bedload sediment transport in coastal waters. *Coastal Engineering*, 52:673–689.

Soulsby, R. L., R. J. S. Whitehouse, and K. V. Marten
2012. Prediction of time-evolving sand ripples in shelf seas. *Continental Shelf Res.*, 38:47–62.

Stive, M. J. F., M. A. de Schipper, A. P. Luijendijk, S. G. J. Aarninkhof, C. van Gelder-Maas, J. S. M. van Thiel de Vries, S. de Vries, M. Henriquez, S. Marx, and R. Ranasinghe
2013. A new alternative to saving our beaches from sea-level rise: The sand engine. *J. Coastal Research*, 29(5).

Styles, R. and S. M. Glenn
2000. Modeling stratified wave and current bottom boundary layers on the continental shelf. *J. Geophys. Res.*, 105(C10):24,119–24,139.

Summerfield, M.
2005. A tale of two scales, or two geomorphologies. *Transactions of the Institute of British Geographers*, 30(4).

Swart, D. H.
1974. Offshore sediment transport and equilibrium beach profiles. *Delft Hydr. Lab Publ. No 131.*

Terwindt, J. H. J. and K. M. Wijnberg
1991. Thoughts on large scale coastal behavior. In *Coastal Sediments.*

Testik, F. Y., S. I. Voropayev, and H. J. S. Fernando
2005. Adjustment of sand ripples under changing water waves. *Physics of Fluids*, 17.

Thornton, E. B., J. L. Swayne, and J. R. Dingler
1998. Small-scale morphology across the surf zone. *Marine Geology*, 145:173–196.

Traykovski, P.
2007. Observations of wave orbital scale ripples and a nonequilibrium time-dependent model. *J. Geophys. Res.*, 112(C06026):doi:10.1029/2006JC003811.

Traykovski, P., A. E. Hay, J. D. Irish, and J. F. Lynch
1999. Geometry, migration, and evolution of wave orbital ripples at leo-15. *J. Geophys. Res.*, 104(C1):1505–1524.

Trowbridge, J. and S. Elgar
2001. Turbulence measurements in the surf zone. *Journal of Physical Oceanography*, 31.

Trowbridge, J. H.
1998. On a technique for measurement of turbulent shear stress in the presence of surge waves. *J. Atmospheric and Ocean Technology*, 15:290–298.

van der A, D. A., J. S. Ribberink, J. J. van der Werf, T. O'Donoghue, R. H. Buisrogge, and W. M. Kranenburg
2013. Practical sand transport formula for non-breaking waves and currents. *Coastal Engineering*, 76:26–42.

Van der Werf, J. J., J. S. Doucette, T. O'Donoghue, and J. S. Ribberink
2007. Detailed measurements of velocities and suspended sand concentrations over full-scale ripples in regular oscillatory flow. *Journal of Geophysical Research-Earth Surface*, 112(F2).

van Rijn, L.
1993. *Principles of sediment transport in rivers, estuaries and coastal seas.* The Netherlands: Aqua Publications.

van Rijn, L. C.
2007. Unified view of sediment transport by currents and waves. i: Initiation of motion, bed roughness, and bed-load transport. *Journal of Hydraulic Engineering*, 133.

van Rijn, L. C., D. J. R. Walstra, and M. Ormondt
2004. Description of transpor2004 and implementation in delft3d-online: final report. Technical report, Deltares.

Warner, J., C. Sherwood, R. Signell, C. Harris, and H. Arango
2008. Development of a three-dimensional, regional, coupled wave, current, and sediment-transport model. *Computers & Geosciences*, 34(10):1284–1306.

Wengrove, M. E. and D. L. Foster
2014. Field evidence of the viscous sublayer in a tidally forced developing boundary layer. *Geophysical Research Letters*.

Wengrove, M. E., D. L. Foster, M. A. de Schipper, and T. C. Lippmann
2017. Wave and current ripple formation and migration during storms. *Proceedings of Coastal Dynamics 2017*, (129).

Wengrove, M. E., D. L. Foster, T. C. Lippmann, M. A. de Schipper, and J. Calantoni
2018a. Observations of bedform migration and bedload sediment transport in combined wave-current flows. *Journal of Geophysical Research - Oceans*.

Wengrove, M. E., D. L. Foster, T. C. Lippmann, M. A. de Schipper, and J. Calantoni
2018b. Observations of time dependent bedform transformation in combined wave-current flows. *Journal of Geophysical Research - Oceans*.

Wiberg, P. L. and C. K. Harris
1994. Ripple geometry in wave-dominated environments. *Journal of Geophysical Research*, 99.

Wikramanayake, P. N. and O. S. Madsen
1994. Calculation of movable bed friction factors. Technical report for us army corps of engineers, Massachusetts Institute of Technology.

Wilson, G. W. and A. E. Hay
2016. Acoustic observations of near-bed sediment concentration and flux statistics above migration sand dunes. *Geophysical Research Letters*, 43.

Winter, C., G. Vittori, V. B. Ernstsen, and J. Bartholdy
2008. On the superimposition of bedforms in tidal channels. In *Marlene and River Dune Dynamics*.

Zala Flores, N. and J. F. A. Sleath
1998. Mobile layer in oscillatory sheet flow. *J. Geophys. Res.*, 103(C6):12,783–12,793.

Zhao, Q. and J. T. Kirby
2005. Bagnold formula revisited: Incorporating pressure gradient into energetics models. *Proc. Waves'05 Madrid*.

APPENDIX A

LIST OF SYMBOLS

Appendix A provides a list and description of symbols used in the dissertation.

Table A.1: Symbols.

A	orbital amplitude	m
c	speed of sound	m/s
C_D	drag coefficient	–
d_{50}	grain size	m
D_*	$d_{50}\left(\frac{(s-1)g}{\nu^2}\right)^{1/3}$	–
d_o	wave orbital diameter	m
$E_{k_{wc}}$	total kinetic energy in waves and currents	$\rho(\mathrm{m/s})^2$
$f_{2.5}$	grain size friction factor	–
f_c	current friction factor	–
f_w	wave friction factor	–
f_{wc}	wave current factor	–
g	acceleration due to gravity (9.81 m/s/s)	m/s/s
h	water depth	m
k_s	$= d_{90}$ (500 μm)	m
n	sediment packing fraction (0.7)	–
p	pressure	m of H_2O
Q_b	bedload mass sediment flux	kg/(ms)
q_b	bedload volumetric sediment flux	$\mathrm{m}^3/(\mathrm{ms})$
Re	Reynolds number $= uL/\nu$	–
r	roughness	m
s	ρ_s/ρ	–
T	wave period	s
u, v, w	horizontal, horizontal, vertical components of velocity	m/s
U	mean velocity	m/s
U_c	current velocity	m/s
u_o	wave orbital velocity ($\sqrt{2}u_{rms}$)	m/s
u_{rms}	rms wave velocity	m/s

Table A.2: Symbols cont'd.

u_{wc}	combined wave-current velocity	m/s
$\tilde{u}$	phase average velocity	m/s
u'	velocity fluctuation	m/s
u_*	friction velocity	m/s
u_{*_c}	friction velocity of current flow	m/s
u_{*_r}	friction velocity of combined flow	m/s
$u_{*_{wm}}$	friction velocity of wave flow	m/s
$Vol._b$	bedform volume	m^3
v_m	bedform migration rate	m/s
w_s	sediment settling velocity	m/s
x, y, z	horizontal, horizontal, vertical direction defintion	m
x_b	horizontal direction normal to the bedform orientation	m
z_b	bed elevation	m
z_o	roughness length scale, generally based on grain size	m
δ_{wc}	boundary layer thickness	m
δ_{x_b}	phase offset between q_b and z_b	m
η	bedform height	m
κ	von Karmen coefficient, 0.38 in boundary layer flows	–
λ	bedform wavelength	m
μ	dynamic viscosity	Ns/m^2
ν	kinematic viscosity	m^2/s
Φ	dimensionless sediment flux, $_x$ or $_y$ indicate components	–
ϕ	angle between waves and currents	$\circ$
ϕ_r	bedform orientation	$\circ$
θ	Shields parameter	–
θ_c	current Shields parameter	–
θ_{crit}	critical Shields parameter (0.05 for given d_{50})	–
θ_w	wave Shields parameter	–
θ_{wc}	combined wave-current Shields parameter	–
ρ	water density (1030 kg/m^3)	kg/m^3
ρ_s	sediment density (2650 kg/m^3)	kg/m^3
τ or τ_{lag}	lag time for bedform growth	time
τ_b	bed shear stress	N/m^2
τ_c	current induced shear stress	N/m^2
τ_{crit}	critical bed shear stress based on θ_{crit}	N/m^2
τ_e	effective shear stress	N/m^2
τ_m	mean shear stress averaged over wave cycle	N/m^2
τ_{max}	max shear stress within wave cycle	N/m^2
τ_p	periodic shear stress	N/m^2
τ_{rms}	rms shear stress	N/m^2
τ_w	wave induced shear stress or wall shear stress (context)	N/m^2

APPENDIX B

WAVE AND CURRENT RIPPLE FORMATION AND MIGRATION DURING STORMS - COASTAL DYNAMICS 2017 CONFERENCE PROCEEDING

Appendix B provides detail on methods used to process data from the MEGAPEX 2014 field experiment. The content of Appendix B is published as a Conference Proceeding for Coastal Dynamics 2017 - Helsingor, Denmark.

Coastal Dynamics 2017

Paper No. 129

WAVE AND CURRENT RIPPLE FORMATION AND MIGRATION DURING STORMS

Meagan E. Wengrove[1], Diane L. Foster[2], Matthieu A. de Schipper[3], and Thomas C. Lippmann[4]

Abstract

Field observations of bedform response to combined wave-current flows were obtained within the surf zone along the Delfland coast, The Netherlands, as part of the MEGAPEX Field Experiment in the fall of 2014. Fine scale seafloor topography was observed with a rotating pencil beam sonar along with co-located observations of waves and currents. New methods for sonar processing were implemented to find fluid-sediment boundaries, quantify bedform geometry, and estimate bedform migration rates. Observed bedform geometries with wavelengths ranging from 0.14 to 2.5 m and migration rates between 0 and 3 cm/min are strongly influenced by variations in the flow field due to the spring-neap tidal cycle as well as forcing from several storm events. Results suggest that the combined effects of storm waves and mean currents most strongly influence small scale morphodynamic behaviors.

Key words: bedforms, combined flows, currents, sediment transport, morphodynamics, field experiment

1. Introduction

In coastal environments small scale bed roughness (e.g. sand ripples) can have a significant influence on local hydrodynamics (Traykovski et al., 1999). In the nearshore, waves, tidal currents, river currents, storm surge, and alongshore currents can each contribute significantly to local morphodynamics. In particular, a nonlinear combination of waves and currents can strongly influence bedform geometries and sediment transport (Lacy et al., 2007). Many field and laboratory observations of bedform evolution have been made under wave dominated conditions (see Soulsby et al., 2005); however, far fewer have been made under combined wave-current flows (e.g. Li and Amos, 1998; Gallagher et al., 1998; Lacy et al., 2007; Larsen et al., 2015). Significant differences exist between current generated bedforms and those generated by waves (Fredsøe and Deigaard, 1992), and so parameterizing roughness in combined flows using results from only-wave or only-current conditions may lead to misrepresentation of sediment transport flux estimates in morphologic modeling. In order to better predict the effects of bedforms on larger scale sediment transport patterns, it is important to improve understanding hydrodynamic forcing drives the evolution of small scale coastal morphology, and the influence that combined flows have upon these changes.

Surf zone observations of wave and current induced bedform formation and migration during spring-neap tidal variations and the passing of several storms were made on the Delfland coast of The Netherlands. Data were collected at the Sand Engine as a part of the MEGA-Perturbation EXperiment (MEGAPEX) in the fall of 2014. Since the installment of the 20 million cubic meter sand mega-nourishment in 2011, nearshore morphology has dramatically changed shape; in 2011 the Sand Engine extended 2 km in the alongshore and 1 km into the North Sea, and by 2014 it stretched to 4.5 km alongshore and contracted to 700 m seaward (Stive, et al. 2013; Radermacher, et al. 2017).

Our research focus is on fine scale spatial and temporal resolution of seafloor morphology that respond to the combined influence of storm waves and strong currents in the nearshore, and forms one of few observational data sets of bedforms under combined wave-current flows.

[1] Ocean Engineering, University of New Hampshire (UNH). med36@wildcats.unh.edu
[2] Department of Mechanical Engineering and Ocean Engineering, UNH. diane.foster@unh.edu
[3] Hydraulic Engineering Department, CiTG, Technical University of Delft. m.a.deschipper@tudelft.nl
[4] Center for Coastal and Ocean Mapping and Department of Earth Sciences, UNH. lippmann@ccom.unh.edu

2. Methods

2.1. *Instrumentation*

Local small scale morphology and hydrodynamics were observed just seaward of the low tide shoreline at the tip of the Sand Engine (Figure 1). Seafloor topography was obtained with a stationary sweeping and incrementallyrotating 1 MHz Imagenex 881a pencil beam sonar with a 3 m diameter footprint, sampled every 20 minutes with a 1.4° sweep step and a 2.4° rotation step from 26 Sept. to 23 Oct. 2014 (day of year 269-296). The vertical profile of horizontal currents measured using a downward looking high resolution acoustic Doppler current profiler (ADCP) positioned ~0.4 m above the bottom boundary and sampled at 4 Hz in 20 minute bursts every hour. The mean low water depth was -0.3 m NAP (Normaal Amsterdams Peil) and the median sediment grain size was 350 µm. Generally, the tidal range was approximately 1.5 m. These observations were collected just seaward of the shore break.

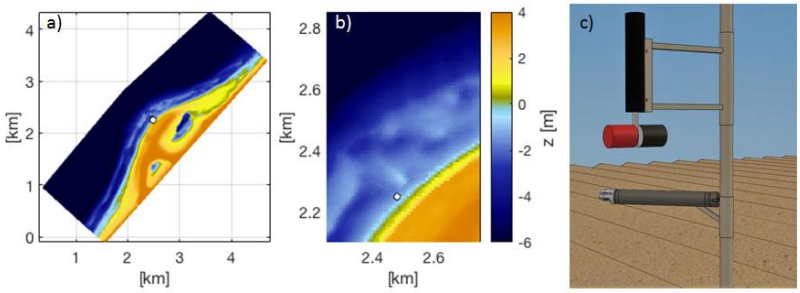

Figure 1. Sampling location and instrument set up. a) Sand Engine mega-nourishment, North is toward the positive y-axis, East is toward the positive x-axis. b) Close-up showing sampling location marked by white circle. c) Schematic showing instrument setup; upper instrument is an Imagenex pencil beam sonar (located 1 m from the boundary); lower instrument is a downward looking high resolution ADCP (located 0.4 m from the boundary).

2.2. *Morphologic Statistics*

Statics of bedform wavelength (λ), height (η), direction (ϕ), migration rate (V_{mig}), and migration direction (ϕ_{mig}) are determined through analysis of sonar return data. These statistics can be determined using processed bathymetries found through analysis of the sonar intensity data for every sonar sweep (e.g. Figure 2).

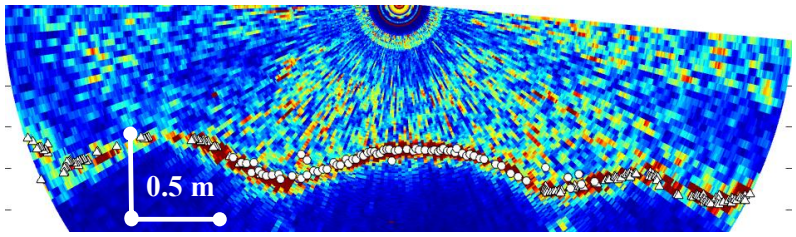

Figure 2. Ripple profile at peak of storm showing wavelength of 2 m and height of 25 cm (Julian day 295.05 for reference to time series in Figure 4). Image color scale is intensity of acoustic return, where reds are high intensity and blues are low intensity. Bottom return is indicated by the dark red line signal. The sonar head is located at the top center of the image. The white circles are the result of the WMS bottom finding method and the white triangles are the result of the BDI bottom finding method. Scale bars are shown in lower left hand corner.

2.2.1. *Bottom Finding*

Bottom position within each sonar dataset was found by identifying the high intensity return region for each sonar ping using two methods. The first is a weighted mean sum (WMS) method, which works well for return data with high grazing angles (data within ~30° of the sonar nadar). The second is a bearing direction indicator (BDI) method, which works well for intensity returns at low grazing angles. WMS is applied to each sonar ping return time series and BDI is applied considering every sonar ping return time series in an entire sonar sweep (see Figure 2). The sweep is composed of many sonar pings, each originating from the sonar head (Figure 2). This assumes that the acoustic return for each ping within a sweep is the same with respect to the relative time of the return pulse. Using estimates of sound speed and ping angle, return time, t, can be transformed into a distance from the sonar head, so within each sweep the coordinate system is (s, z), where s is the horizontal distance away from the sonar head, and z is the vertical distance away from the sonar head. A sonar ping return time series for any given direction is henceforth referred to as an individual beam.

The WMS method is defined by a summation over time of return along an individual beam,

$$WMS = \frac{\sum_{t=1}^{T} n_t^{\beta} n_t}{\sum_{t=1}^{T} n_t^{\beta}}, \tag{1}$$

where, n_t is the acoustic return time along any beam, n, from the sonar head to the extent of the collection (somewhere below the boundary return), and β is a weighting factor, set to 10 (SeaBeam, 2000). The location of the highest WMS for each beam is the (s, z) location of the bed.

The BDI method assumes that every sweep of the pencil beam sonar is analogous to one pulse from a multi-beam sonar. At low grazing angles, multiple beams in a sweep for a given time, t, will capture a return from the same piece of boundary, especially if there are bedforms present. By combining the return information from all beams gives a better estimation of the location of the bed. In essence, the BDI method takes into account the intensity peaks of all beams in a given sweep for some return time. Each peak with intensity greater than a given noise threshold are fit with a 3-5 point parabola. Within a given sweep, at locations where the return signal is interacting with the boundary at a low grazing angle, there will be two parabolic fits to the signal return, one for the $+s$ direction from the sonar head and one for the $-s$ direction. In the ideal case the center peak in both directions will have the strongest intensity return. The peak of the fitted parabola in Cartesian coordinates is the (s, z) location of the bed (SeaBeam, 2000).

After all (s, z) bed locations are determined using both WMS and BDI, the respective sweeps are rotated in a horizontal plane around the sonar head to determine the relative (x, y, z) position rendering a local bathymetric map for each sonar run.

2.2.2. *Estimating Bedform Geometry and Migration Rates*

From the 2D local bathymetry maps, the dominant ripple wavelengths, heights, and orientations are determined with 2D spatial spectral analysis (Maier and Hay, 2009; Becker et al., 2007). The 2D spatial spectra have axes of wavenumber, k_x and k_y (1/m), and energy density, S (m^4). The location of the dominant peaks in the spectra indicate the associated bedform wave number, where bedform wavelength, orientation, and height are defined, respectively.

$$\lambda = 2\pi/(k_x^2 + k_y^2)^{0.5}, \tag{2}$$

$$\phi_r = \mathrm{atan}(k_y/k_x), \tag{3}$$

$$\eta = 4\sqrt{\int\int \eta(k)^2 dk_x dk_y}. \tag{4}$$

The calculation of bedform height, η, is analogous to a significant ocean wave height calculation from temporal spectral analysis (Traykovski, 2007; Penko, et al., 2016). Figure 3 shows three example bathymetries and their corresponding 2D spectra.

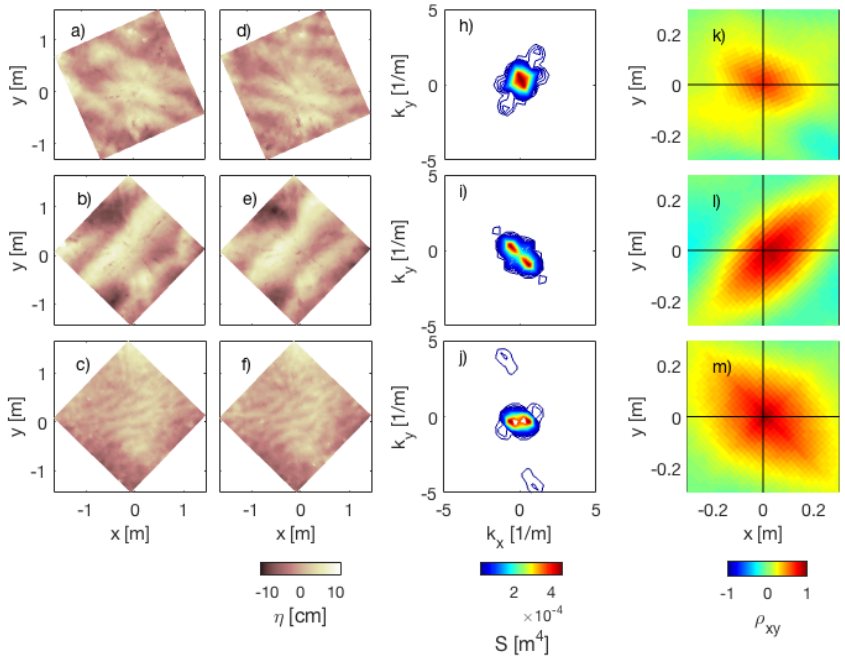

Figure 3. Bathymetry maps (a-f) and 2D spectra of a-c (h-j) and 2D cross correlations between a-d, b-e, and c-f (k-m). Orientation of image is –y directed onshore, +x directed towards the NE, -x directed toward the SW as seen in Figure 1. (a-f) Local bathymetry maps found using the WMS and BDI methods. (h-j) 2D spectra of bathymetries a-c, respectively. Orientation of lobes shows orientation of bedforms, and position of lobe corresponds to bedform wavenumber. (k-m) 2D cross correlation between bathymetric pairs. The location of peak correlation corresponds to the magnitude and direction of bedform migration between bathymetric pairs. Ex: Panel b) has a wavelength of 1.1 m, orientation of 45° from shore normal to the NE; migration distance in a 20 minute period between image pairs is 7 cm, which corresponds to a migration rate of 0.35 cm/min; migration direction is 80° from shore normal to the NE.

To find migration rates and migration directions a 2D cross correlation was used. The 2D cross correlation, ρ_{xy}, is defined as

$$\rho_{xy} = \frac{(x_t - \mu_x)(y_t - \mu_y)}{\sigma_x \sigma_y}, \tag{5}$$

where, x and y indicate the subsequent bathymetries in time that are being compared spatially, μ is the mean, and σ is the standard deviation (Bendat and Piersol, 2010). From the maxima (x_m, y_m) in the 2D cross correlation, the migration rate and migration direction can be found, respectively, by

$$V_{mig} = \frac{\sqrt{x_m^2 + y_m^2}}{t_s}, \tag{6}$$

$$\phi_{mig} = \mathrm{atan}(y_m / x_m), \tag{7}$$

respectively, where t_s is the time between the subsequent bathymetry pair. Figure 3 shows three example bathymetry pairs and their corresponding 2D cross correlation.

2.3. *Hydrodynamic Statistics*

Hydrodynamic statistics were calculated using measured velocity components from the ADCP. The current velocity, U, and direction, ϕ_c, were found, respectively, by

$$U = \sqrt{\overline{u}^2 + \overline{v}^2}, \tag{8}$$

$$\phi_c = \mathrm{atan}(\overline{v}/\overline{u}), \tag{9}$$

where u and v are the horizontal components of velocity and the overbar represents a 10 minute mean. By removing the mean current,

$$u_w = \sqrt{u^2 + v^2} - U \tag{10}$$

the orbital velocity, u_o, is calculated using the root mean square velocity as

$$u_o = \sqrt{2}\sqrt{\overline{|u_w^2|}} \tag{11}$$

and the direction of the waves, ϕ_w, is defined with

$$\phi_w = \mathrm{atan}((v - \overline{v})/(u - \overline{u})). \tag{12}$$

3. Results and Discussion

3.1 Hydrodynamics

Bedform geometry and orientation is a result of the hydrodynamic forcing imposed upon the boundary. Time series of bedform wavelength, orientation, migration rate, and migration direction are shown in Figure 4d and 4e, along with time series of water depths (4a), mean current magnitude (4b), and rms orbital

velocities (4c). The variability in hydrodynamic forcing drives the bedform geometry and migration patterns. The color scale represents flow direction, bedform orientation, or bedform migration direction. The magnitude and direction of the current indicate that the mean current is highly dominated by tides. The predominant tidal orientation on the Delfland coast is shore parallel, with flood tides directed toward the NE and ebb tides toward the SW (see Figure 1 for reference). The magnitude of the current during flood tide is generally stronger than during ebb tide; however, with additional storm forcing the wave-driven flow exceeds the tidal flow in the inner surf zone. The time series goes through 2 spring-neap cycles and has 4 storm events (indicated in Figure 5). Spring flood tidal currents are stronger than those during neap.

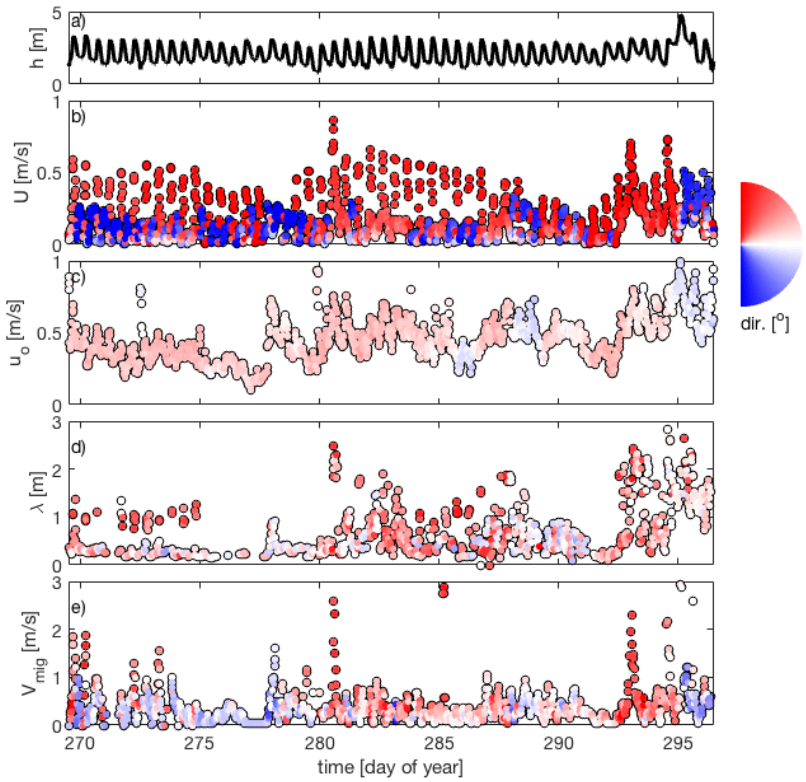

Figure 4. Time series of hydrodynamic and bedform statistics colored by flow direction or bedform orientation as indicated by the color wheel (white is directed onshore, dark red and blue are alongshore, with red flowing or oriented toward the NE and blue toward the SW as seen in Figure 1). a) depth. b) current magnitude. c) wave orbital velocity. d) bedform wavelength. e) bedform migration rate.

At the Sand Engine, wave forcing is driven by frequent offshore storms lasting typically 1-3 days. The magnitude of the wave orbital velocity at the sampling location within the inner surf zone (Figure 4c) increases with the onset of storms but is tidally modulated due to wave breaking on the offshore sandbar at lower stands of the tide. In general, waves came from the NW during the experiment and strike the coast at an angle driving a longshore current to the SE.

3.2 Bedform Geometry and Mobility in Response to Waves and Currents

Bedform wavelengths (Figure 4d) and migration rates (Figure 4e) are influenced by both mean currents and waves. During spring tide (day of year 270-275) bedform wavelengths and migration rates are strongly influenced by large tidal currents, increasing and decreasing as a function of current magnitude. At day of year 278, 281, 283, and 293, the bedform wavelengths and migration rates increase during the passing of a storm. Bedform migration direction is qualitatively influenced by the direction of the current. Bedform migration direction is influenced by both wave direction and current direction with a bias toward the direction of the currents. Bedform orientation shows similar patterns, but is not as strongly influenced by current direction. The largest and most mobile bedforms occur when both the waves and currents are strongly contributing to the hydrodynamic forcing (as seen between day of year 293 and 296).

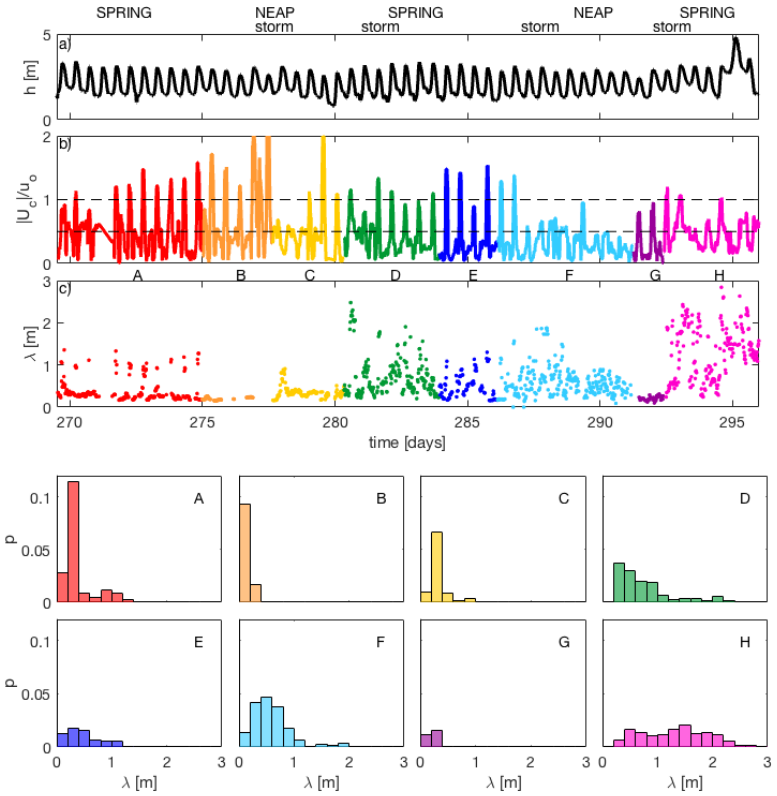

Figure 5. Time series of hydrodynamic forcing ratio and corresponding histograms of bedform wavelength for each forcing segment. Each histogram accounts for only those bedforms occurring within that highlighted segment; however distribution probability is relative to all observations, and hence the probability of occurrence, p, for any individual wavelength within each distribution is small. Spring tide, neap tide and periods with additional storm forcing are labeled above the top panel. a) Time series of depth. b) Time series of ratio of current velocity and wave orbital velocity colored in segments by periods of spring tide and neap tide with or without added storm forcing. Dashed lines indicate thresholds for wave dominant, combined wave-current dominant, and current dominant forcing as described in the text. c) Time series of bedform wavelength colored in same way as panel b. A-H are corresponding histograms of bedform wavelength for each colored and labeled segment as seen in panel b and c.

To examine the relationship between bedform geometry shifts and variability in hydrodynamics, the time series is segmented based upon forcing conditions, and a histogram of bedform wavelength is computed for each segment (Figure 5). Figure 5b shows a ratio of current magnitude to wave orbital velocity, analogous to Li and Amos (1998), where bedforms are thought to be wave formed when $U/u_o \leq 0.5$, combined wave current formed when $0.5<U/u_o \leq 1$ or current formed when $U/u_o > 1$. Segments A and E show spring tide without storm forcing, B and G show neap tide without storm forcing, C and F show neap tide with storm forcing, and D and H show spring tide with storm forcing.

When comparing periods of spring tide to neap tide without storm forcing, spring tide histograms A and E show an occurrence of larger wavelength bedforms (0.8 m or greater) that are not evident during neap tide without storms (B and G). When viewing histogram A in light of Figure 5b and 5c, it is evident that these larger wavelength bedforms were formed with the onset of strong currents. During neap tide the flood tide current is much weaker than during spring tide and does not likely generate these large wavelength bedforms. Even though segment B shows data with $U/u_o > 1$, which would indicate current induced bedforms, the magnitude of the current and orbital velocities during this period are low, suggesting that in this case current dominance erodes existing bedforms rather than forms new bedforms. Without storms, bedforms formed during neap tide and in-between periods of strong current during spring tide are wave induced ($U/u_o \leq 0.5$).

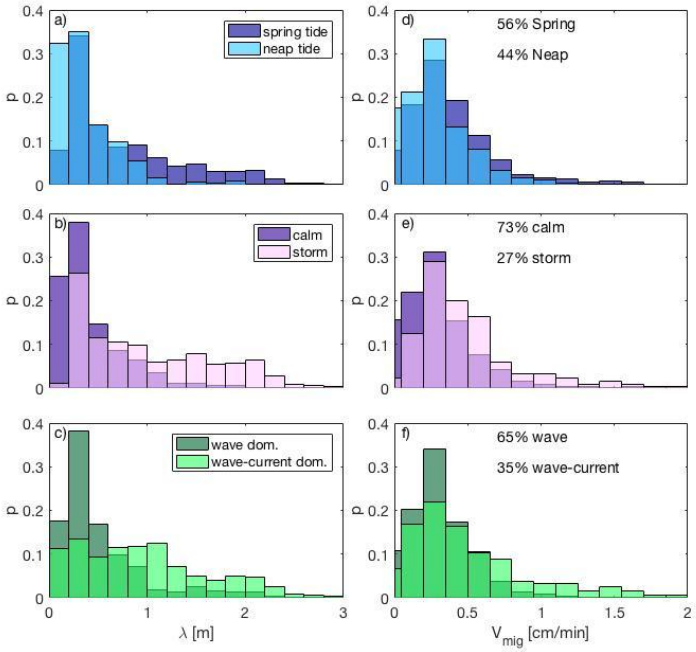

Figure 6. Histograms of bedform wavelength and migration rates based upon legend data segmentations. Within each panel, each histogram distribution is relative to itself and not to the entire dataset, meaning in panels a) and d) the distribution of bedform wavelength and migration rate is accounting for instances occurring within only spring tide or only neap tide. The percent of the dataset that falls within spring tide or neap tide is labeled in the upper right hand corner of d) for both panels. b) and e) Histograms of bedform wavelength and migration rate, respectively, segmented by periods of calm and storm. The percent of the dataset that falls within calm and storm periods are labeled in the upper right hand corner of e) for both panels. c) and f) Histograms of bedform wavelength and migration rate, respectively, segmented by periods of wave dominated flow and combined flow. The percent of the dataset that falls within wave dominated and combined flow conditions is labeled in the upper right hand corner of f) for both panels.

When storms do occur during neap tidal periods (C and F), there are a few instances of larger wavelength bedforms; however during these periods U/u_o is generally ≤ 0.5, suggesting that these wave formed bedforms as well. The wavelength of these bedforms is at times longer due to the larger storm waves. The largest wavelength and most dynamic bedforms occur during spring tide with the onset of a storm (D and H). The hydrodynamic forcing is greatest during the D and H segments (Figure 4b and 4c), and these bedforms were at times wave induced, current induced, or combined wave-current induced, with the largest bedforms being formed during periods of combined wave-current forcing (Figure 5b).

Observations of bedform geometry and mobility at the Sand Engine are observed to be variable based on the phase of the tide as well as the presence of a storm. Histograms of bedform wavelength and migration rates are segmented into observations based upon spring tide and neap tide (Figure 6a and 6d), calm and storm conditions (Figure 6b and 6e), and wave dominant ($U/u_o \leq 0.5$) and current or combined flow dominant ($U/u_o > 0.5$) (Figure 6c and 6f). These histograms are relative to only the data in the respective segment, rather than the entire set of observations as was the case for the histograms in Figure 5. The percentage of data falling into each segment is marked in the upper right hand corner of the right hand panels in Figure 6. These 12 histograms summarize factors driving bedform transformation and mobility during the deployment.

As bedforms get larger they can have a progressively greater influence on the local hydrodynamics. With the addition of increased bedform migration rates that move more sediment, the effect on coastal change could be more important. This suggests that the occurrence of larger wavelength bedforms ($\lambda \geq 0.8$ m) with increased migration rates ($V_{mig} \geq 1$ cm/min) may be disproportionally important to the net transport.

Although there were many observed occurrences of smaller wavelength bedforms ($\lambda < 0.8$ m) during all tides, there were slightly (10%) more, larger wavelength bedforms ($\lambda \geq 0.8$ m) during spring tides (Figure 6a). A similar variation is observed in the migration rate, with 5% increased occurrence of larger migration rates during spring tide compared to neap tide.

During the experiment storm conditions were present for 27% of the dataset. Under storm forcing, there is a 20% increase in occurrence of larger wavelength bedforms and an 8% increase in occurrence of higher bedform migration rates (Figure 6b and 6e) compared to calm conditions. Although during spring and neap tidal periods two storms of similar magnitude occurred, the spring tide bedforms had a higher frequency of occurrence of larger wavelength bedforms than neap tide (Figure 6a), a result that can be attributed to strong tidal currents of spring tide (as seen in Figure 4) in conjunction with additional storm forcing. Spring tides with the addition of storm waves had a 42% increase in occurrence of larger wavelength bedforms and a 5% increase of higher migration rates when compared to the rest of the dataset (Figure 5, periods D and H).

Histograms shown in Figure 6c and 6f show that combined flows are responsible for a 14% increase in occurrence of larger wavelength bedforms and a 13% increase in occurrence of higher migration rates when compared to the distributions of wave dominant flows only.

The influence of combined flows ($0.5 < U/u_o \leq 1$) on bedform wavelength and migration rates is shown in Figure 7. Bedforms with wavelengths greater than 0.8 m can occur during wave dominant, combined wave-current dominant, and current dominant forcing conditions with variable migration rates (from no migration to high migration). However, the largest observed migration rates occurred during periods of combined flows and slightly current dominated flows (it should be noted that there are a few occurrences of large migration rates in wave dominant conditions, possibly due to wave asymmetries when waves get large). Within combined flow conditions, as migration rates increase, bedform wavelengths are also generally larger. These large and rapidly migrating bedforms are likely to be transporting the most sand per unit time and are linked to flow conditions characterized by strong tidal currents coincident with storm waves (Figure 5).

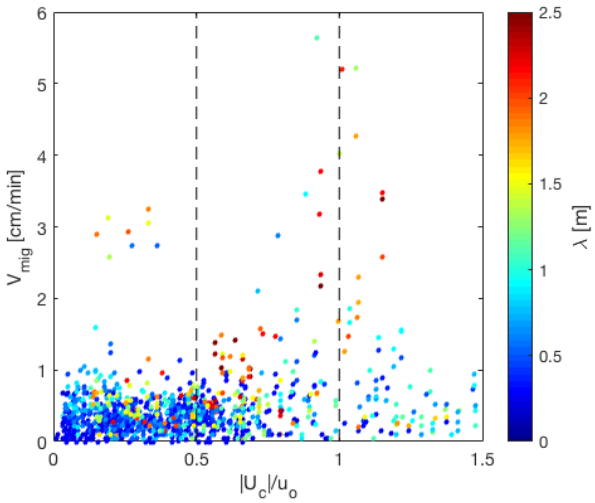

Figure 7. Scatter plot of the ratio of current velocity to orbital velocity plotted against bedform migration rate and colored by bedform wavelength. Dashed lines indicate cutoffs for defined wave, wave-current, and current dominant conditions.

4. Conclusion

Observations of local hydrodynamics and morphology indicate that both wave and mean current forcing contribute to the transformation and migration of nearshore bedforms during both calm and storm conditions. At the Sand Engine, bedform dynamics are strongly tidally regulated and greatly influenced by additional forcing from storms.

With the presence of a storm and in the absence of strong spring tidal currents, bedforms are generally wave dominated. Wave dominated bedforms can become large depending upon the size of the waves. Additionally, bedforms are shown to become purely current driven during spring flood tides in the absence of an imposed storm. Within these field observations, the largest and fastest moving bedforms occurred during combined flows during spring tides and storm waves, suggesting that combined forcing events may have the greatest influence on morphodynamics.

Overall, results show that combined flows can substantially contribute to changes in nearshore morphology, more than with wave or current forcing alone. Often, sediment transport models account for transport due to waves or due to currents, but not the combined effects of wave-current forcing. This research suggests that combined flow effects are important to bedform geometries and migration, and should be considered within sediment transport models. Examination of the combined flow effects upon bedform formation and influence upon sediment transport flux as well as its contribution to local coastal change is the subject of ongoing research.

Acknowledgements

Funding for our field efforts during MEGAPEX was provided by the PADI Foundation, ERC – advanced grant 291206-NEMO, and UNH. MEW is supported by a U.S. DOD NDSEG fellowship. MAdS is financed by NWO Domain Applied and Engineering Sciences under project code 15058. TCL was supported by the Office of Naval Research.

References

Bendat, J. S. and A. G. Piersol, 2010. *Random Data*. John Wiley and Sons.

Becker, J. M., Y. L. Firing, J. Aucan, R. Holman, M. Merrifield, and G. Pawlak, 2007. Video-based observations of nearshore sand ripples and ripple migration. *Journal of Geophysical Research*, 112.

Fredsøe, J., and R. Deigaard, 1992. *Mechanics of coastal sediment transport*. World Scientific.

Gallagher, E. L., S. Elgar, and E. B. Thornton, 1998. Megaripple migration in a natural surf zone. *Letters to Nature*, 394.

Lacy, J. R., D. M. Rubin, H. Ikeda, K. Mokudai, and D. M. Hanes, 2007. Bed forms created by simulated waves and currents in a large flume. *Journal of Geophysical Research*, 112.

Larsen, S. M., B. Greenwood, and R. Aagaard, 2015. Observations of megaripples in the surf zone. *Marine Geology*, 364.

Li, M. Z., and C. L. Amos, 1998. Predicting ripple geometry and bed roughness under combined waves and currents in a continental shelf environment. *Continental Shelf Research*, 18, 941–970.

Maier, I., and A. E. Hay, 2009. Occurrence and orientation of an orbital ripples in near- shore sands. *Journal of Geophysical Research*, 114.

Penko, A., J. Calantoni, and B. T. Hefner, 2016. Modeling and observations of sand ripple formation and evolution during trex13, *Journal of Oceanic Engineering*.

Radermacher, M., M. A. de Schipper, C. Swinkles, J. H. MacMahan, A. J.H.M. Reniers, 2017. Tidal flow separation at protruding beach nourisments, *Journal of Geophysical Research:Oceans*.

SeaBeam, 2000. Multibeam sonar theory of operation, Tech. rep., L3 *Communications of SeaBeam Instruments*.

Soulsby, R. L., R. J. S. Whitehouse, and K. V. Marten, 2005. Prediction ripple properties in shelf seas. *HR Wallingford Report*, TR 150.

Stive, M. J. F., M. A. de Schipper, A. P. Luijendijk, S. G. J. Aarninkhof, C. van GelderMaas, J. S. M. van Thiel de Vries, S. de Vries, M. Henriquez, S. Marx, and R. Ranasinghe, 2013. A new alternative to saving our beaches from sea-level rise: The sand engine. *Coastal Engineering*, 29(5).

Traykovski, P., A. E. Hay, J. D. Irish, and J. F. Lynch, 1999. Geometry, migration, and evolution of wave orbital ripples at leo-15. *Journal of Geophysical Research*, 104(C1), 1505–1524.

Traykovski, P, 2007. Observations of wave orbital scale ripples and a nonequilibrium time-dependent model. *Journal of Geophysical Research*, 112(C06026)

APPENDIX C

INSTRUMENTATION

Appendix C provides detail on instrumentation used at the MEGAPEX 2014 field experiment.

- Imagenex 881a Pencil-beam with Azimuth Drive: The Imagenex 881a Pencil-beam sonar is a pencil beam profiling sonar that is able to rotate in a 2D plane perpendicular to the sonar beam axis. The motor step size is between 0.3° and 2.4°. The 881a has operation frequencies between 310 kHz to 1 MHz. The transducer beam width is 1.4° when operated at 1MHz. The sonar records data in sound intensity, and is not calibrated for water column backscatter.

  With the added azimuth drive, the sonar is rotated so that the combination of both rotation axis create a 3D image when fully sampled. With 2 mm range resolution the sampling range is between 1 and 4 m. The azimuth drive step motor rotates through 359° at as low 0.3° increments.

  The vertical resolution for each ping remains constant, however the horizontal resolution of the 3D image becomes coarser with increasing distance away from the sonar. At 1 m range, the horizontal planar resolution with a sonar motor step size of 1.4° and an azimuth motor step size of 1.4° at the sonar nader is approximately 2 cm x 2 cm, however 1 m displaced from the sonar nader the resolution becomes 5 cm x 3 cm (Imagenex, 2011).

- Nortek AquadoppHR ADCP (acoustic Doppler current profiler): The AquadoppHR is a pulse coherent current profiler that transmits at 2 MHz with a dynamic range of

90 dB and resolution of 0.45 dB and samples at a rate of 1 Hz to 8 Hz depending upon its interval burst length (buffer time between data collections). The current profiler has 3 diverging beams at 45° with beam width of 1.7°. It can profile over a distance of up to 3 m, with a minimum resolution of 7 mm (there are significant tradeoffs for range/resolution/sampling rate). The Doppler uncertainty is 1% of the velocity measurement ± 0.5 cm/s. Uncertainty is determined by a combination of short term (instrumental) and long term bias (generally environmental). Data quality is monitored with a signal to noise ratio (SNR) and a correlation level for each beam.

The current profiler measures velocity parallel to each of the three diverging beams, and nothing perpendicular, this is why the beams are diverging from each other, so that all 3 components of velocity can be measured. Each beam is both a transducer and a receiver. The profiler estimates velocity using phase differencing between coherent pings within each beam along the profile by sampling at a series of overlapping cells, where the cell size is often the same length as the transmit pulse length. Cell position and size is determined by a combination of transmit pulse length and the receive window (or how long the instrument is listening) (NortekAS, 2013).

- Nortek Vector ADV (acoustic Doppler velocimeter): The Vector is a pulse coherent velocimeter that transmits at 6 MHz with a dynamic range of 90 dB with a resolution of 0.45 dB and samples at a rate up to 64 Hz. The velocimeter has one central transmitter and three inward looking receivers angled at 30°. This velocimeter measures velocity at a single point, and is rugged, developed for field deployments. The Vector uses the Doppler shift to estimate water column velocity, it samples in beam coordinates and then does a coordinate transformation to Cartesian coordinates or East-North-Up coordinates using the onboard compass. The instrument sweet spot where the velocity measurement is made is 15 cm from the transducer face. The Doppler uncertainty is a function of the beam pattern, the pulse rate, and the pulse length. The Doppler uncertainty is 1% of the velocity measurement ± 1 mm/s. Uncertainty is determined

by a combination of short term (instrumental) and long term bias (generally environmental). Data quality is monitored with a signal to noise ratio (SNR) and a correlation level for each beam (NortekAS, 2013).

- PIV (particle image velocimetry): In PIV a laser is used to illuminate scatters in the flow field and then a series of high speed snapshots of the flow are taken with synced cameras. The velocity field is found by calibrating the images to a known geometry and then preforming a correlation between image pairs to estimate distance that the same particle moved over the known image pair collection rate. The spatial and temporal resolution of the PIV system depends upon the PIV equipment (i.e. camera pixel resolution, camera snap resolution, temporal capacity of on board data buffering) as well as how fast the cameras need to take subsequent image pairs. Interrogation windows are generally overlapped by 50% (Carlson, 2015).

  The PIV dataset of Frank and Calantoni (2016) and that from the OSU Large Wave Flume Dataset have different spatial and temporal resolution accuracies.

- Nortek Vectrino Profiler PADV (profiling acoustic Doppler velocimeter): The Vectrino Profiler is a bi-static pulse coherent velocimeter that transmits at 10 MHz with a dynamic range of 60 dB and samples at a rate of up to 100 Hz. The velocimeter has one central transmitter and four inward looking receivers. The instrument is rather fragile, developed for laboratory experiments, although it has been used in the field. The profiling range spans over 3.5 cm from 4 cm to 7.5 cm away from the transducer face with resolution of 1 mm. The instrument is composed of two individual dual-axis velocimeters for each directional plane (x, z_1) and (y, z_2). The Vectrino Profiler first samples in beam coordinates, for each of the four receivers and then does a coordinate transformation to shift to Cartesian coordinates. The instrument produces a velocity profile with discrete cells within the range where the transducer beam and 2 of the opposite receiver beams overlap. Cell position and size is determined by a combination

of transmit pulse length and the receive window (or how long the instrument is listening). The angle of the receivers from the transducer plane is 16° from parallel, making the acoustic sweet spot 5.5 cm away from the transducer face, this introduces bias into the range bins closer and further from this sweet spot. The Doppler uncertainty is 1% of the velocity measurement. Uncertainty is determined by a combination of short term (instrumental) and long term bias (generally environmental). Data quality is monitored with a signal to noise ratio (SNR) and a correlation level for each beam (Craig et al., 2010).

The profiler measures velocity at every range bin using the Doppler shift by measuring a change in phase of the return signal from scatters in the water column ($v = [c\Delta\phi]/[4\pi f\Delta t]$, where v is velocity, c is speed of sound, $\Delta\phi$ is the change in phase between two coherent pulses, f is the carrier frequency, and Δt is the change in time (Craig et al., 2010).

There are two independent references that discuss the ability for the Vectrino profiler to measure velocities near a boundary. The first is the online supplementary material of Wengrove and Foster (2014) and the second is a paper discussing the velocimeter performance over various bottom types Koca et al. (2017). Both references conclude that the velocimeter can measure velocity to within 2 cm of the boundary over smooth and low reflection surfaces. This is mainly because of the beam pattern of the instrument in the acoustic near-field.

- MFDop PADV (profiling acoustic Doppler velocimeter): The MFDop is a privately developed velocimeter that has one central transmitter and four inward looking receivers to measure the water velocity using the Doppler shift.The MFDop operated at two carrier frequencies within the dataset discussed, 1.4 and 1.8 MHz. The vertical profile is separated into 4 mm range bins, and the acoustic beam is approximately conical with half-width 1.4° (i.e., the beam diameter is 3 cm at the nominal range-to-bed of 60

cm), so each range bin represents a sample volume of 2 cm^3 (Wilson and Hay, 2016). Wilson and Hay (2016) references three additional papers about the development of the MFDop. Similarities exist between this instrument and the Nortek Vectrino Profiler, however the MFDop operates at a range of carrier frequencies and can change receiver angle. Additionally, the MFDop has a sampling profile range of 20-30 cm with mm to cm scale range bins (Hay et al., 2012a).

APPENDIX D

SELECT BED STRESS FORMULATIONS

Appendix 4 provides details of select formulations to estimate bed stress used in coastal applications.

A select set of bed stress approximations are given, however with the more complicated formulations the reader is also refered to the origional citation. Unique symbols are defined within the following text, while others are listed in the List of Symbols table in Appendix A.

- Nielsen (1992) proposed the following for τ_b within wave environments with a friction factor proposed by Swart (1974) based upon grain size. Generally this bed stress is presented as a Shields parameter.

$$\tau_{2.5} = 0.5 f_{2.5} \rho ((d_o/2)(2\pi/T))^2, \tag{D.1}$$

$$f_{2.5} = \exp(5.213(2.5 d_{50}/(d_o/2))^{0.194} - 5.977). \tag{D.2}$$

- Li and Amos (1998) proposed the following for τ_b within current dominant environments with a friction factor of 0.003.

$$\tau_c = 0.5 \rho 0.003 U_c^2. \tag{D.3}$$

- Grant and Madsen (1979) proposed an estimate of τ_b in combined waves and currents, however the formulation was revised in Madsen (1994), which is overviewed here, however the original text gives the entire derivation. This is an iterative spectral method to estimate bed shear stress. Initially the Navier-Stokes equations are closed with an eddy viscosity and then wave friction velocity is solved for using a set of Kelvin functions and the near-bottom orbital velocity spectrum. The current friction velocity is solved for assuming a logarithmic boundary layer. This approach is used to solve for wave, current, and combined flow bed stress. Very basically,

$$u_{*_{wm}} = (0.5 f_{wc} u_o^2)^{0.5}, \tag{D.4}$$

where, $u_{*_{wm}}$ is the friction velocity imposed by the waves and f_{wc} is the wave-current friction factor defined in Madsen (1994), and is iterated upon until convergence, with variability in the estimate introduced by a ratio of the current friction velocity to the wave friction velocity, μ. The combined flow is represented by,

$$u_{*_r} = C_\mu u_{*_{wm}}^2, \tag{D.5}$$

where, u_{*_r} is the friction velocity imposed by the combined flow, and C_μ is a scaling parameter of the current fraction to the wave fraction as defined in Madsen (1994). The current flow is represented by,

$$u_{*_c} = \frac{u_{*_r}}{2} \frac{ln(z/\delta_{wc})}{ln(\delta_{wc}/z_o)} \Big(-1 + \Big[1 + \frac{4\kappa ln(\delta_{wc}/z_o)}{(ln(z/\delta_{wc}))^2} \frac{U_c}{u_{*_r}} \Big]^{0.5} \Big), \tag{D.6}$$

where, δ_{wc} is the wave-current boundary layer thickness, z_o is the roughness height, U_c is the current velocity measured at z. Finally, $\tau = \rho u_*^2$.

- Soulsby and Clarke (2005) proposed a method that calculates the shear stress from the currents (τ_c) and the waves (τ_w) alone, and then proposes a relationship for an effective shear stress (τ_e) of the combined flow based upon an eddy viscosity assumption, just as in Madsen (1994). However, Soulsby and Clarke (2005) also make a simplifying assumption that the wave shear is not enhanced by the current shear in order to be able to represent the eddy viscosity based upon known quantities.

$$\tau_c = \rho C_D U_c^2, \tag{D.7}$$

where, C_D is a drag coefficient.

$$\tau_w = \rho 0.5 f_w u_o^2, \tag{D.8}$$

where, $f_w = 1.39(A/z_o)^{-0.52}$ is a wave friction factor. And,

$$\tau_e^2 = \tau_w^2 + \tau_c^2. \tag{D.9}$$

Continuing forward, the derivation describes expressions for the mean (τ_m), max (τ_{max}), periodic (τ_p), and rms (τ_{rms}) shear stress in combined flows that depend upon the previous definitions. For the mean stress,

$$\tau_m = \rho\Big(\frac{1}{2a}\big[(b^2 + 4aU_c)^{0.5} - b\big]\Big)^2, \tag{D.10}$$

where, a and b are logarithmic relationships dependent upon the τ_e. For the periodic stress,

$$\tau_p = (0.5\tau_e f_w)^{0.5} u_o, \tag{D.11}$$

The max stress is also dependent on the direction that the waves are propigating in relation to the currents (ϕ).

$$\tau_{max} = \left[(\tau_m + \tau_p|\cos\phi|)^2 + (\tau_p|\sin\phi)^2\right]^{0.5}. \tag{D.12}$$

Finally, $\tau_{rms} = (\tau_m^2 + 0.5\tau_p^2)^{0.5}$.

- Styles and Glenn (2000) approach finding the bed shear stress by assuming an eddy viscosity closure. The basic equations for the combined flow stress are as follows.

$$\tau_{wc} = C_R\tau_w, \tag{D.13}$$

$$\tau_w = \rho 0.5 f_{wc} C_R u_o^2, \tag{D.14}$$

where, C_R is a current enhancement factor, and f_{wc} can be found by taking the limit of $\partial u_o/\partial z$ as z goes to z_o, where the final expression is

$$f_{wc} = 2(\kappa\xi\gamma_{wc})^2, \tag{D.15}$$

where, ξ and γ_{wc} are the non-dimensional vertical coordinate and the non-dimensional hydraulic roughness defined in Styles and Glenn (2000).

APPENDIX E

SELECT BEDLOAD SEDIMENT TRANSPORT FORMULATIONS

Appendix E provides details of select formulations to estimate bedload sediment transport used in coastal applications.

Many transport formulas are given as a function of the Shields parameter, θ, defined in equation 5.10 and is dependent upon an estimate of bed stress. Other bedload transport formulas are not explicitly dependent upon an outside approximation of stress. All transport formulations herein are given in the units of mass transport rate, Q_b (kg/(ms)) or volume transport rate, q_b (m^3/(ms)), where $Q_b = \rho_s q_b$. Unique symbols are defined within the following text, while others are listed in the List of Symbols table in Appendix A.

Generally, transport formulas are given for specified flow conditions, such as waves, currents, or combined flows. The following give formulas initially for unidirectional flows, then for waves, and finally for combined flows, however, some transport formulas that were initially formulated for unidirectional flow, that are dependent upon the Shields parameter have been shown to apply to wave and combined flows as well.

- Unidirectional Flow
  - Meyer-Peter and Muller (1948) estimated transport for flows in rivers initially, however this formulation has been and can be applied to wave or combined flow environments with appropriate approximations for bed stress in these flows. Generally for combined flows stress has been approximated with the Madsen (1994) combined flow stress estimate or a combination of the Li and Amos (1998) added

to the Nielsen (1992) 2.5 approximations given in Appendix D. Meyer-Peter and Muller (1948) estimate transport as,

$$Q_{b_{MPM48}} = 8(\theta - \theta_{crit})^{1.5}\rho_s d_{50}((s-1)gd_{50})^{0.5}. \tag{E.1}$$

– Nielsen (1992) as well as others proposed a modified version of the the Meyer-Peter and Muller (1948) formulation, however all for steady, unidirectional flow.

$$Q_{b_{N92}} = 12\theta^2(\theta - \theta_{crit})\rho_s d_{50}((s-1)gd_{50})^{0.5}. \tag{E.2}$$

- Waves

  – Madsen and Grant (1976) estimate transport for a wave half cycle as,

$$Q_{b_{GM76}} = \rho_s 12.5 w_s d_{50}\theta_w^3, \tag{E.3}$$

  where, w_s is the settling velocity, and the formula is valid for $\theta_w > \theta_{crit}$, otherwise $Q_{b_{GM76}} = 0$.

  – Soulsby (1997) estimates transport for a wave half cycle as,

$$Q_{b_{S97}} = \rho_s 5.1[g(s-1)d_{50}^3]^{1/2}(\theta_w - \theta_{crit})^{3/2}, \tag{E.4}$$

  which is very similar to the unidirectional formations.

- Combined Flow

– van Rijn et al. (2004) have a complex formulation for surfzone transport estimates, and a simplified version for coastal, but non-surfzone transport in van Rijn (2007), both of these approximations are formulated for combined flows.

$$Q_{b_{vR04}} = \gamma \rho_s d_{50} D_*^{-0.03} \frac{\tau_{bwc}}{\rho}^{0.5} \Big(\frac{max(\tau_{bwc} - \tau_{crit}, 0)}{\tau_{crit}} \Big)^{\eta_{vr}}, \tag{E.5}$$

$$\tau_{bwc} = 0.5 \rho f_{wc} u_i^2, \tag{E.6}$$

where u_i is the instantaneous velocity due to waves and currents,

$$f_{wc} = \alpha^{0.5} \beta_f f_c + (1 - \alpha^{0.5}) f_w, \tag{E.7}$$

$$f_c = 0.24 (log(12h/k_s))^{-2}, \tag{E.8}$$

$$f_w = exp(-6 + 5.2((d_o/2)/k_s)^{-0.19}), \tag{E.9}$$

$$\beta_f = 0.75 + 0.45 \Big(2 \Big(\frac{f_w}{f_c} \Big)^{0.5} \frac{u_o}{U_c} \Big)^{1.13}, \tag{E.10}$$

where, $\alpha = \frac{U_c}{u_o + U_c}$, β_f is a coefficient related to vertical structure of velocity profile, η_{vr} is a coefficient with default value of 1, and γ is a coefficient with default value of 0.5.

Transport estimated with van Rijn (2007), this is a simplified version of the 2004 formulation. It is a modified version of the van Rijn (1993) formulations made for rivers by using Soulsby (1997) to extend the formulations to coastal flows (steady flow plus waves). This formulation is not made for the complex environments of inner surf and swash zones,

$$Q_{b_{vR07}} = \alpha_b \rho_s U_c h (d_{50}/h)^{1.2} M_e^{1.5}, \tag{E.11}$$

$$M_e = \frac{u_e - u_{crit}}{((s-1)gd_{50})^{0.5}}, \tag{E.12}$$

where u_e is the effective velocity for waves and currents $= U_c + \gamma_e u_o$ ($\gamma_e = 0.4$ for irregular waves and 0.8 for regular waves), and u_{crit} is the critical velocity $= \beta_e u_{crc} + (1 - \beta u_{crw}$, $\beta_e = U_c/(U_c + u_o)$, u_{crc} and u_{crw} are the critical velocities for waves and currents based on grain size, respectively. For $0.00005 < d_{50} < 0.0005m$ $u_{crc} = 0.19 d_{50}^{0.1} log(12h/3d_{90})$, and $u_{crw} = 0.24((s-1)g)^{0.66} d_{50}^{0.33} T^{0.33}$.

– Soulsby/van Rijn (Soulsby, 1997) give an estimate for bedload transport in combined flows as

$$Q_{b_{SvR97}} = A_b U_c \Big[\Big(U_c^2 + \frac{0.018}{C_D} u_{rms}^2 \Big)^{1/2} - U_{cr} \Big]^{2.4} (1 - 1.6 \tan\beta), \tag{E.13}$$

where,

$$A_b = \frac{0.005 h (d_{50}/h)^{1.2}}{[(s-1)gd_{50}]^{1.2}} \tag{E.14}$$

$$C_D = \Big(\frac{\kappa}{[ln(h/z_o) - 1]} \Big)^2 \tag{E.15}$$

and β is the slope of the bed in the streamwise direction, U_{cr} is a threshold current velocity based upon grain size defined in Soulsby (1997).

– Souslby (Soulsby, 1997) gives a transport formulation for combined flows as,

$$\Phi_{x1} = 12 \theta_m^{1/2} (\theta_m - \theta_{crit}), \tag{E.16}$$

$$\Phi_{x2} = 12(0.95 + 0.19 \cos 2\phi) \theta_w^{1/2} \theta_m, \tag{E.17}$$

$$\Phi_x = max(\Phi_{x1}, \Phi_{x2}), \tag{E.18}$$

$$\Phi_y = \frac{12(0.19\theta_m\theta_w^2 \sin 2\phi}{\theta_w^{3/2} + 1.5\theta_m^{3/2}}, \tag{E.19}$$

subject to $\Phi_x = \Phi_y = 0$ if $\theta_m ax \leq \theta_{crit}$, where θ_m is the mean value of θ over a wave cycle, θ_w is the amplitude of oscillatory component of θ due to wave.

$$Q_{b_{S97}} = \rho_s[\Phi_x^2 + \Phi_y^2]^{1/2}[g(s-1)d_{50}^3]^{1/2}. \tag{E.20}$$

– Soulsby and Damgaard (2005) derived an expression for bedload transport under currents and asymmetric waves. They assume that bedload transport only occurs as a thin sheet flow layer over the boundary regardless of whether the bottom is flat or rippled. So, as long as the threshold of motion has been reached (i.e. $\theta > \theta_{crit}$) then these transport equations apply. The equations presented here are derived from assuming a velocity profile shape within the sheet flow layer and a sheet flow layer thickness based upon applied bed stress, constant A_2 is derived from this and sediment properties, they can be found in Soulsby and Damgaard (2005).

$$\Phi_{x1} = A_2\theta_m^{1/2}(\theta_m - \theta_{crit}), \tag{E.21}$$

$$\Phi_{x2} = A_2(0.9534 + 0.1907\cos 2\phi)\theta_w^{1/2}\theta_m + A_2(0.229\Delta\theta_w^{3/2}\cos\phi), \tag{E.22}$$

$$\Phi_x = max(\Phi_{x1}, \Phi_{x2}), \tag{E.23}$$

$$\Phi_y = A_2\frac{0.1907\theta_w^2}{\theta_w^{3/2} + (3/2)\theta_m^{3/2}}(\theta_m \sin 2\phi + 1.2\Delta\theta_w \sin\phi), \tag{E.24}$$

where, θ_m is the mean value over a wave cycle, θ_w is the Sheilds parameter due to waves, ϕ is the angle between the waves and currents, $\Delta = \theta_{w,2}/\theta_w$, or a ratio of the amplitude of the Shields parameter for the second harmonic to the first harmonic of the asymmetric wave. And,

$$Q_{b_{SD05}} = \rho_s[\Phi_x^2 + \Phi_y^2]^{1/2}[g(s-1)d_{50}^3]^{1/2}. \tag{E.25}$$

– Hsu et al. (2006) is an extension of the energetics sediment transport formulations by Bailard and Inman (1981).

$$Q_{b_{HEG06}} = K_w \frac{\epsilon_b}{\tan\phi_s}\langle|u_o|^2 u_o\rangle + K_c \frac{\epsilon_b}{\tan\phi_s}\langle|(u_o^2 + U_c^2)^{1/2}|^2 U_c\rangle, \tag{E.26}$$

$$K_w = \frac{C_w}{(s-1)g}, K_c = \frac{C_c}{(s-1)g} \tag{E.27}$$

where, ϕ_s is the friction angle, $\epsilon_b = 0.135$, $C_w = 0.0046$, and $C_w = 0.0053$.

APPENDIX F

DERIVATION OF VOLUMETRIC CHANGE MODEL

Appendix F provides a derivation of the proposed volumetric change model described in Chapter 3. The derivation of the phase shift for transport over bedforms is also part of this appendix.

First assuming a transport function as

$$q = \hat{q}\cos(\omega t - kx_b - k\delta_{x_b}). \tag{F.1}$$

Use $\cos(\alpha - \beta) = \cos(\alpha)\cos(\beta) + \sin(\alpha)\sin(\beta)$, and

$$q = \hat{q}_1\cos(\omega t - kx_b) + \hat{q}_2\sin(\omega t - kx_b), \tag{F.2}$$

$$\hat{q}_1 = \hat{q}\cos(k\delta_{x_b}), \hat{q}_2 = \hat{q}\sin(k\delta_{x_b}), \tag{F.3}$$

and $\hat{q}_2/\hat{q}_1 = \tan(k\delta_{x_b})$.

And we assume that the bed level can be described by

$$z_b(x_b, t) = \hat{\eta}\cos(\omega t - kx_b). \tag{F.4}$$

The the sediment continuity equation is,

$$\frac{\partial q}{\partial x_b} \equiv -n\frac{\partial z_b}{\partial t}. \tag{F.5}$$

If the equations for $\hat{q}$ and z_b are substituted into the sediment continuity equation by taking the derivative of both, and assuming that $\hat{\eta}$ is a function of t, but $\hat{q}_1$ and $\hat{q}_2$ are not a function of x_b, then,

$$\frac{\partial z_b}{\partial t} = \frac{\partial \hat{\eta}}{\partial t}\cos(\omega t - kx_b) - \hat{\eta}\omega \sin(\omega t - kx_b), \tag{F.6}$$

and

$$\frac{\partial q}{\partial x_b} = \hat{q}_1 k \sin(\omega t - kx_b) - \hat{q}_2 k \cos(\omega t - kx_b). \tag{F.7}$$

Now,

$$n\hat{\eta}\omega = k\hat{q}_1 \Rightarrow \hat{q}_1 = n\hat{\eta}V_{mig.}, \tag{F.8}$$

and

$$n\frac{\partial \hat{\eta}}{\partial t} = k\hat{q}_2 \Rightarrow \hat{q}_2 = \frac{n}{k}\frac{\partial \hat{\eta}}{\partial t}, \tag{F.9}$$

where (F.8) represents the sediment flux from the migrating bedform, and (F.9) represents the sediment flux from a growing or decaying bedform. Now, substituting (F.3) into (F.8) and (F.9), and equating the result by means of $\hat{q}$,

$$\frac{\partial \hat{\eta}}{\partial t} = k\hat{\eta}V_{mig.}\tan(k\delta_{x_b}). \tag{F.10}$$

Now solve for δ_{x_b}, as a function of $\partial\eta/\partial t$ and $V_{mig.}$,

$$\delta_{x_b} = \frac{\tan^{-1}([\frac{\partial \hat{\eta}}{\partial t}/k]/[\eta V_{mig.}])}{k}. \tag{F.11}$$

Now, to solve for the bedform volumetric change as a function of the sediment flux, use the product rule on the RHS of (F.9), where

$$\frac{n}{k}\frac{\partial \hat{\eta}}{\partial t} = \frac{n}{2\pi}\frac{\partial \hat{\eta}\lambda}{\partial t} - \frac{n}{2\pi}\frac{\hat{\eta}\partial\lambda}{\partial t}, \tag{F.12}$$

If $\frac{1}{2}n\frac{\partial \hat{\eta}\lambda}{\partial t}$ is taken to be $\frac{\partial Vol._b}{\partial t}$, then

$$\pi\hat{q}\sin(2\pi\delta_{x_b}/\lambda) = \frac{\partial Vol._b}{\partial t} - \frac{n}{2}\frac{\hat{\eta}\partial\lambda}{\partial t}. \tag{F.13}$$

And now integrating from $t-\tau$ to t,

$$\Delta Vol._b - \int_{t-\tau}^{t} \frac{n}{2}\frac{\hat{\eta}\partial\lambda}{\partial t}dt = \int_{t-\tau}^{t} \pi\hat{q}\sin(2\pi\delta_{x_b}/\lambda)dt. \tag{F.14}$$

APPENDIX G

MOMENTUM INTEGRAL METHOD DERIVATION FOR UNSTEADY UNIDIRECTIONAL FLOW

Appendix G provides a derivation of the momentum integral method for unsteady, unidirectional flow with a no-slip condition at the boundary.

Starting with 2 dimensional unsteady momentum equation in the BL

$$\frac{\partial u}{\partial t} + u\frac{\partial u}{\partial x} + v\frac{\partial u}{\partial y} = -\frac{1}{\rho}\frac{\partial p}{\partial x} + \nu(\frac{\partial^2 u}{\partial x^2} + \frac{\partial^2 u}{\partial y^2}) \tag{G.1}$$

Reynolds decomposition and averaging (i.e ensemble averaging):
$u = U + u'$ - streamwise direction (x)
$w = W + w'$ - vertical direction (z)
$p = P + p'$

$$\overline{\frac{\partial(U+u')}{\partial t}} + \overline{(U+u')\frac{\partial(U+u')}{\partial x}} + \overline{(W+w')\frac{\partial(U+u')}{\partial z}} = -\frac{1}{\rho}\frac{\partial P}{\partial x} + \nu\left(\overline{\frac{\partial^2(U+u')}{\partial x^2}} + \overline{\frac{\partial^2(U+u')}{\partial z^2}}\right) \tag{G.2}$$

Rearranging

$$\frac{\partial U}{\partial t} + U\frac{\partial U}{\partial x} + W\frac{\partial U}{\partial z} - \frac{\partial}{\partial x}(\nu\frac{\partial U}{\partial x} - \overline{u'^2}) + \frac{1}{\rho}\frac{\partial P}{\partial x} - \frac{\partial}{\partial z}(\nu\frac{\partial U}{\partial z} - \overline{u'w'}) = 0 \tag{G.3}$$

which can be written as:

$$\frac{\partial U}{\partial t} + \frac{1}{\rho}\frac{\partial P}{\partial x} + I - \frac{\partial}{\partial z}(\nu\frac{\partial U}{\partial z} - \overline{u'w'}) = 0 \tag{G.4}$$

where $I = U\frac{\partial U}{\partial x} + W\frac{\partial U}{\partial z} - \frac{\partial}{\partial x}(\nu\frac{\partial U}{\partial x} - \overline{u'^2}) = \frac{\partial}{\partial z}(\nu\frac{\partial U}{\partial z} - \overline{u'w'}) - \frac{\partial U}{\partial t} - \frac{1}{\rho}\frac{\partial P}{\partial x}$
Note: If advection terms are negligible, i.e. in fully developed channel flow $I = U\frac{\partial U}{\partial x} + W\frac{\partial U}{\partial z} - \frac{\partial}{\partial x}(\nu\frac{\partial U}{\partial x} - \overline{u'^2}) = 0$; hence $\frac{\partial U}{\partial t} + \frac{1}{\rho}\frac{\partial P}{\partial x} = \frac{\partial}{\partial z}(\nu\frac{\partial U}{\partial z} - \overline{u'w'})$

integrate equation (4) from 0 to z_t

(noting $\nu\frac{\partial U}{\partial z}(0) = \frac{\tau_w}{\rho}$ and $\overline{u'w'}(0) = 0$ for a fixed boundary and $\nu\frac{\partial U}{\partial z}(0) - \overline{u'w'}(0) = 0$ for a mobile boundary) :

$\int_0^{z_t}\left(\frac{\partial U}{\partial t} + \frac{1}{\rho}\frac{\partial P}{\partial x}\right)dz + \int_0^{z_t} I\,dz - \int_0^{z_t}\frac{\partial}{\partial z}(\nu\frac{\partial U}{\partial z} - \overline{u'w'})dz = 0$

$\int_0^{z_t}\left(\frac{\partial U}{\partial t} + \frac{1}{\rho}\frac{\partial P}{\partial x}\right)dz + \int_0^{z_t} I\,dz - \nu\frac{\partial U}{\partial z} + \overline{u'w'} + \nu\frac{\partial U(0)}{\partial z} - \overline{u'w'}(0) = 0$

$$\int_0^{z_t}\left(\frac{\partial U}{\partial t}+\frac{1}{\rho}\frac{\partial P}{\partial x}\right)dz+\int_0^{z_t} I\,dz-\nu\frac{\partial U}{\partial z}+\overline{u'w'}+\frac{\tau_w}{\rho}=0 \tag{G.5}$$

integrate equation (5) from 0 to z_t:

$\left[\int_0^{z_t}\int_0^{\eta}\left(\frac{\partial U}{\partial t}+\frac{1}{\rho}\frac{\partial P}{\partial x}\right)dzd\eta\right]+\left[\int_0^{z_t}\int_0^{\eta} I dzd\eta\right]-\nu\int_0^{z_t}\frac{\partial U}{\partial z}dz+\int_0^{z_t}\overline{u'w'}dz+\frac{\tau_w}{\rho}\int_0^{z_t}dz=0$

$$\begin{aligned}\left[z_t\int_0^{z_t}\left(\frac{\partial U}{\partial t}+\frac{1}{\rho}\frac{\partial P}{\partial x}\right)dz-\int_0^{z_t} z\left(\frac{\partial U}{\partial t}+\frac{1}{\rho}\frac{\partial P}{\partial x}\right)dz\right]+\left[z_t\int_0^{z_t} I dz-\int_0^{z_t} z I dz\right]-\ldots\\ \nu(U-U(0))+\int_0^{z_t}\overline{u'w'}dz+\frac{\tau_w}{\rho}z_t=0\end{aligned} \tag{G.6}$$

integrate equation (6) from 0 to z_t:

$\left[\int_0^{z_t}\eta\int_0^{\eta}\left(\frac{\partial U}{\partial t}+\frac{1}{\rho}\frac{\partial P}{\partial x}\right)dzd\eta-\int_0^{z_t}\int_0^{\eta} z\left(\frac{\partial U}{\partial t}+\frac{1}{\rho}\frac{\partial P}{\partial x}\right)dzd\eta\right]+\left[\int_0^{z_t}\eta\int_0^{\eta} I dzd\eta-\int_0^{z_t}\int_0^{\eta} z I dzd\eta\right]-\ldots$

$\nu\int_0^{z_t} U dz+\int_0^{z_t}\int_0^{\eta}\overline{u'w'}dzd\eta+\frac{\tau_w}{\rho}\int_0^{z_t} z dz=0$

$$\begin{aligned}\left[\frac{z_t^2}{2}\int_0^{z_t}\left(\frac{\partial U}{\partial t}+\frac{1}{\rho}\frac{\partial P}{\partial x}\right)dz-\int_0^{z_t}\frac{z^2}{2}\left(\frac{\partial U}{\partial t}+\frac{1}{\rho}\frac{\partial P}{\partial x}\right)dz-z_t\int_0^{z_t} z\left(\frac{\partial U}{\partial t}+\frac{1}{\rho}\frac{\partial P}{\partial x}\right)dz-\int_0^{z_t} z^2\left(\frac{\partial U}{\partial t}+\frac{1}{\rho}\frac{\partial P}{\partial x}\right)dz\right]+\ldots\\ \left[\frac{z_t^2}{2}\int_0^{z_t} I dz-\int_0^{z_t}\frac{z^2}{2} I dz-z_t\int_0^{z_t} z I dz-\int_0^{z_t} z^2 I dz\right]-\nu\int_0^{z_t} U dz+\int_0^{z_t}(z_t-z)\overline{u'w'}dz+\frac{\tau_w}{\rho}\int_0^{z_t} z dz=0\end{aligned} \tag{G.7}$$

rearranging equation (7) and combining terms:

$$\boxed{\tau_w=\underbrace{\frac{2\mu}{z_t^2}\int_0^{z_t} U dz}_{\text{I}}-\underbrace{\frac{2\rho}{z_t^2}\int_0^{z_t}(z_t-z)\overline{u'w'}dz}_{\text{II}}-\underbrace{\frac{\rho}{z_t^2}\int_0^{z_t}(z_t-z)^2 I dz}_{\text{III}}-\underbrace{\frac{\rho}{z_t^2}\int_0^{z_t}(z_t-z)^2\left(\frac{\partial U}{\partial t}+\frac{1}{\rho}\frac{\partial P}{\partial x}\right)dz}_{\text{IV}}} \tag{G.8}$$

In fully developed channel flow, the third term on the RHS of the Eq. 8 is 0.

replacing I:

$$\tau_w=\frac{2\mu}{z_t^2}\int_0^{z_t} U dz-\frac{2\rho}{z_t^2}\int_0^{z_t}(z_t-z)\overline{u'w'}dz-\frac{\rho}{z_t^2}\int_0^{z_t}(z_t-z)^2\left(\frac{\partial}{\partial z}(\nu\frac{\partial U}{\partial z}-\overline{u'w'})-\frac{\partial U}{\partial t}-\frac{1}{\rho}\frac{\partial P}{\partial x}\right)dz-\frac{\rho}{z_t^2}\int_0^{z_t}(z_t-z)^2\left(\frac{\partial U}{\partial t}+\frac{1}{\rho}\frac{\partial P}{\partial x}\right)dz \tag{G.9}$$

$$\boxed{\tau_w = \underbrace{\frac{2\mu}{z_t^2}\int_0^{z_t} U dz}_{\text{I}} - \underbrace{\frac{2\rho}{z_t^2}\int_0^{z_t}(z_t - z)\overline{u'w'}dz}_{\text{II}} - \underbrace{\frac{\rho}{z_t^2}\int_0^{z_t}(z_t - z)^2\frac{\partial}{\partial z}(\nu\frac{\partial U}{\partial z} - \overline{u'w'})dz}_{\text{III+IV}}} \tag{G.10}$$

APPENDIX H

MOMENTUM INTEGRAL METHOD DERIVATION FOR PHASE AVERAGED OSCILLATORY FLOW

Appendix H provides a derivation of the momentum integral method for phase averaged oscillatory flow with a no-slip condition at the boundary.

Starting with 2 dimensional unsteady momentum equation in the BL

$$\frac{\partial u}{\partial t} + u\frac{\partial u}{\partial x} + v\frac{\partial u}{\partial y} = -\frac{1}{\rho}\frac{\partial p}{\partial x} + \nu(\frac{\partial^2 u}{\partial x^2} + \frac{\partial^2 u}{\partial y^2}) \tag{H.1}$$

Reynolds decomposition and averaging (i.e phase averaging):
$u = \widetilde{u} + u'$ - streamwise direction (x)
$w = \widetilde{w} + w'$ - vertical direction (z)
$p = \widetilde{p} + p'$

$$\frac{\partial(\widetilde{\widetilde{u}+u'})}{\partial t} + (\widetilde{u}+u')\frac{\widetilde{\partial(\widetilde{u}+u')}}{\partial x} + (\widetilde{w}+w')\frac{\widetilde{\partial(\widetilde{u}+u')}}{\partial z} = -\frac{1}{\rho}\frac{\partial \widetilde{p}}{\partial x} + \nu\left(\frac{\partial^2(\widetilde{\widetilde{u}+u'})}{\partial x^2} + \frac{\partial^2(\widetilde{\widetilde{u}+u'})}{\partial z^2}\right) \tag{H.2}$$

Rearranging

$$\frac{\partial \widetilde{u}}{\partial t} + \widetilde{u}\frac{\partial \widetilde{u}}{\partial x} + \widetilde{w}\frac{\partial \widetilde{u}}{\partial z} - \frac{\partial}{\partial x}(\nu\frac{\partial \widetilde{u}}{\partial x} - \widetilde{u'^2}) + \frac{1}{\rho}\frac{\partial \widetilde{p}}{\partial x} - \frac{\partial}{\partial z}(\nu\frac{\partial \widetilde{u}}{\partial z} - \widetilde{u'w'}) = 0 \tag{H.3}$$

which can be written as:

$$\frac{\partial}{\partial z}(\widetilde{u'w'} - \nu\frac{\partial \widetilde{u}}{\partial z} + \widetilde{u}\widetilde{w}) + I + \frac{1}{\rho}\frac{\partial \widetilde{p}}{\partial x} = 0 \tag{H.4}$$

where $I = 2\widetilde{u}\frac{\partial \widetilde{u}}{\partial x} - \nu\frac{\partial^2 \widetilde{u}}{\partial x^2} + \frac{\partial \widetilde{u'^2}}{\partial x} = -\frac{\partial}{\partial z}(\widetilde{u'w'} + \nu\frac{\partial \widetilde{u}}{\partial z} - \widetilde{u}\widetilde{w}) - \frac{1}{\rho}\frac{\partial \widetilde{p}}{\partial x}$

integrate equation (4) from 0 to z_t

(noting $\nu\frac{\partial \widetilde{u}}{\partial z}(0) = \frac{\tau_w}{\rho}$ and $\widetilde{u'w'}(0) = 0$ for a fixed boundary, and $\nu\frac{\partial \widetilde{u}}{\partial z}(0) - \widetilde{u'w'}(0) = \frac{\tau_w}{\rho}$ for a mobile boundary) :

$\int_0^{z_t}\left(\frac{\partial \widetilde{u}}{\partial t} + \frac{1}{\rho}\frac{\partial \widetilde{p}}{\partial x}\right)dz + \int_0^{z_t} I\,dz - \int_0^{z_t}\frac{\partial}{\partial z}(\nu\frac{\partial \widetilde{u}}{\partial z} - \widetilde{u'w'} - \widetilde{u}\widetilde{w})dz = 0$

$\int_0^{z_t}\left(\frac{\partial \widetilde{u}}{\partial t} + \frac{1}{\rho}\frac{\partial \widetilde{p}}{\partial x}\right)dz + \int_0^{z_t} I\,dz - \nu\frac{\partial \widetilde{u}}{\partial z} + \widetilde{u'w'} + \widetilde{u}\widetilde{w} + \nu\frac{\partial \widetilde{u}(0)}{\partial z} - \widetilde{u'w'}(0) = 0$

$$\int_0^{z_t}\left(\frac{\partial\widetilde{u}}{\partial t}+\frac{1}{\rho}\frac{\partial\widetilde{p}}{\partial x}\right)dz+\int_0^{z_t} I\,dz-\nu\frac{\partial\widetilde{u}}{\partial z}+\widetilde{u'w'}+\widetilde{u}\widetilde{w}+\frac{\tau_w}{\rho}=0 \tag{H.5}$$

integrate equation (5) from 0 to z_t:

$\left[\int_0^{z_t}\int_0^{\eta}\left(\frac{\partial\widetilde{u}}{\partial t}+\frac{1}{\rho}\frac{\partial\widetilde{p}}{\partial x}\right)dzd\eta\right]+\left[\int_0^{z_t}\int_0^{\eta} Idzd\eta\right]-\nu\int_0^{z_t}\frac{\partial\widetilde{u}}{\partial z}dz+\int_0^{z_t}\widetilde{u'w'}dz+\int_0^{z_t}\widetilde{u}\widetilde{w}dz+\frac{\tau_w}{\rho}\int_0^{z_t}dz=0$

$$\begin{aligned}\left[z_t\int_0^{z_t}\left(\frac{\partial\widetilde{u}}{\partial t}+\frac{1}{\rho}\frac{\partial\widetilde{p}}{\partial x}\right)dz-\int_0^{z_t} z\left(\frac{\partial\widetilde{u}}{\partial t}+\frac{1}{\rho}\frac{\partial\widetilde{p}}{\partial x}\right)dz\right]+\left[z_t\int_0^{z_t} Idz-\int_0^{z_t} zIdz\right]-\ldots\\ \nu(\widetilde{u}-\widetilde{u}(0))+\int_0^{z_t}\widetilde{u'w'}dz+\int_0^{z_t}\widetilde{u}\widetilde{w}dz+\frac{\tau_w}{\rho}z_t=0\end{aligned} \tag{H.6}$$

integrate equation (6) from 0 to z_t:

$\left[\int_0^{z_t}\eta\int_0^{\eta}\left(\frac{\partial\widetilde{u}}{\partial t}+\frac{1}{\rho}\frac{\partial\widetilde{p}}{\partial x}\right)dzd\eta-\int_0^{z_t}\int_0^{\eta} z\left(\frac{\partial\widetilde{u}}{\partial t}+\frac{1}{\rho}\frac{\partial\widetilde{p}}{\partial x}\right)dzd\eta\right]+\left[\int_0^{z_t}\eta\int_0^{\eta} Idzd\eta-\int_0^{z_t}\int_0^{\eta} zIdzd\eta\right]-\ldots$

$\nu\int_0^{z_t}\widetilde{u}dz+\int_0^{z_t}\int_0^{\eta}\widetilde{u'w'}dzd\eta+\int_0^{z_t}\int_0^{\eta}\widetilde{u}\widetilde{w}dzd\eta+\frac{\tau_w}{\rho}\int_0^{z_t} zdz=0$

$$\begin{aligned}\left[\frac{z_t^2}{2}\int_0^{z_t}\left(\frac{\partial\widetilde{u}}{\partial t}+\frac{1}{\rho}\frac{\partial\widetilde{p}}{\partial x}\right)dz-\int_0^{z_t}\frac{z^2}{2}\left(\frac{\partial\widetilde{u}}{\partial t}+\frac{1}{\rho}\frac{\partial\widetilde{p}}{\partial x}\right)dz-z_t\int_0^{z_t} z\left(\frac{\partial\widetilde{u}}{\partial t}+\frac{1}{\rho}\frac{\partial\widetilde{p}}{\partial x}\right)dz-\int_0^{z_t} z^2\left(\frac{\partial\widetilde{u}}{\partial t}+\frac{1}{\rho}\frac{\partial\widetilde{p}}{\partial x}\right)dz\right]+\ldots\\ \left[\frac{z_t^2}{2}\int_0^{z_t} Idz-\int_0^{z_t}\frac{z^2}{2}Idz-z_t\int_0^{z_t} zIdz-\int_0^{z_t} z^2Idz\right]-\nu\int_0^{z_t}\widetilde{u}dz+\int_0^{z_t}(z_t-z)\widetilde{u'w'}dz+\int_0^{z_t}(z_t-z)\widetilde{u}\widetilde{w}dz+\frac{\tau_w}{\rho}\int_0^{z_t} zdz=0\end{aligned} \tag{H.7}$$

rearranging equation (7) and combining terms:

$$\boxed{\tau_w=\underbrace{\frac{2\mu}{z_t^2}\int_0^{z_t}\widetilde{u}dz}_{\text{I}}-\underbrace{\frac{2\rho}{z_t^2}\int_0^{z_t}(z_t-z)\widetilde{u'w'}dz}_{\text{II}}-\underbrace{\frac{2\rho}{z_t^2}\int_0^{z_t}(z_t-z)\widetilde{u}\widetilde{w}dz}_{\text{III}}-\underbrace{\frac{\rho}{z_t^2}\int_0^{z_t}(z_t-z)^2Idz}_{\text{IV}}-\underbrace{\frac{\rho}{z_t^2}\int_0^{z_t}(z_t-z)^2\left(\frac{\partial\widetilde{u}}{\partial t}+\frac{1}{\rho}\frac{\partial\widetilde{p}}{\partial x}\right)dz}_{\text{V}}} \tag{H.8}$$

In fully developed channel flow, the fourth term on the RHS of the Eq. 8 is 0.

replacing I:

$$\begin{aligned}\tau_w=\frac{2\mu}{z_t^2}\int_0^{z_t}\widetilde{u}dz-\frac{2\rho}{z_t^2}\int_0^{z_t}(z_t-z)\widetilde{u'w'}dz-\frac{2\rho}{z_t^2}\int_0^{z_t}(z_t-z)\widetilde{u}\widetilde{w}dz-\frac{\rho}{z_t^2}\int_0^{z_t}(z_t-z)^2\frac{\partial}{\partial z}(\nu\frac{\partial\widetilde{u}}{\partial z}-\widetilde{u'w'}-\widetilde{u}\widetilde{w})\ldots\\ -\frac{\rho}{z_t^2}\int_0^{z_t}(z_t-z)^2\left(\frac{\partial}{\partial z}(\nu\frac{\partial\widetilde{u}}{\partial z}-\widetilde{u'w'}-\widetilde{u}\widetilde{w})-\frac{\partial\widetilde{u}}{\partial t}-\frac{1}{\rho}\frac{\partial\widetilde{p}}{\partial x}\right)dz-\frac{\rho}{z_t^2}\int_0^{z_t}(z_t-z)^2\left(\frac{\partial\widetilde{u}}{\partial t}+\frac{1}{\rho}\frac{\partial\widetilde{p}}{\partial x}\right)dz\end{aligned} \tag{H.9}$$

$$\boxed{\tau_w = \underbrace{\frac{2\mu}{z_t^2}\int_0^{z_t}\widetilde{u}dz}_{\text{I}} - \underbrace{\frac{2\rho}{z_t^2}\int_0^{z_t}(z_t-z)\widetilde{u'w'}dz}_{\text{II}} - \underbrace{\frac{2\rho}{z_t^2}\int_0^{z_t}(z_t-z)\widetilde{u}\widetilde{w}dz}_{\text{III}} - \underbrace{\frac{\rho}{z_t^2}\int_0^{z_t}(z_t-z)^2\frac{\partial}{\partial z}(\nu\frac{\partial\widetilde{u}}{\partial z} - \widetilde{u'w'} - \widetilde{u}\widetilde{w})dz}_{\text{IV+V}}} \tag{H.10}$$

If the equation is then time averaged $\widetilde{u}\widetilde{w} = 0$ in irrotational progressive waves, and Eq. 10 becomes

$$\boxed{\tau_w = \underbrace{\frac{2\mu}{z_t^2}\int_0^{z_t}\widetilde{u}dz}_{\text{I}} - \underbrace{\frac{2\rho}{z_t^2}\int_0^{z_t}(z_t-z)\widetilde{u'w'}dz}_{\text{II}} - \underbrace{\frac{\rho}{z_t^2}\int_0^{z_t}(z_t-z)^2\frac{\partial}{\partial z}(\nu\frac{\partial\widetilde{u}}{\partial z} - \widetilde{u'w'})dz}_{\text{IV+V}}} \tag{H.11}$$

APPENDIX I

DATASETS

Appendix I provides detail on several datasets being used or to be used in the dissertation.

Datasets are described in the following text including the instruments used. More detail about resolution and errors associated with each instrument are in Appendix C.

I.0.1 MEGAPEX Dataset

Data was collected during a campaign at the Sand Engine mega-nourishment as a part of the MEGA-Perturbation EXperiment (MEGAPEX) in the fall of 2014 on the Delfland Coast of the Netherlands. Since the installment of the 20 million cubic meter of sand mega-nourishment in 2011, the Sand Engine has dramatically changed shape; in 2011 it stretched 2 km in the alongshore and 1 km into the North Sea, and in 2014 it stretched 4 km alongshore and 800 m in the cross shore (Stive et al., 2013). On the large scale, the nourishment is very dynamic; raising the question of the dynamic nature of its small scale morphology.

Local small scale morphology and hydrodynamics were observed just seaward of the low tide shoreline (S1) and just shoreward of the subtidal sandbar (S2) at the tip of the Sand Engine (Figure I.1). Morphology was sampled at both locations with two stationary sweeping and rotating 1 MHz Imagenex 881a pencil beam sonars with a 3 m diameter footprint, S1 was sampled every 20 minutes with a 1.4° sweep step and a 2.4° rotation step from 26 Sept. to 23 Oct. 2014 (day of year 269-296), and S2 was sampled twice at 2 hours increments with a 1.4° sweep step and a 1.4° rotation step from 2 Oct. to 18 Oct. (day of year 275 to 291). Concomitant hydrodynamic forcing was measured using an a downward looking high resolution acoustic Doppler current profiler (ADCP) positioned 0.4 m above the boundary

and sampled at 4 Hz at S1, and an acoustic Doppler velocimeter (ADV) positioned 1 m above the boundary and sampled at 64 Hz at S2 (Figure I.1b). The mean lower low water depth at S1 was -0.3 m NAP (Normaal Amsterdam Peil) and at S2 was 0.5 m NAP and the median sediment grain size at both sites was 350 μm. Generally, the tidal range was approximately 1.5 m. Large scale bathymetry was measured with an echo sounder during regular jet ski surveys.

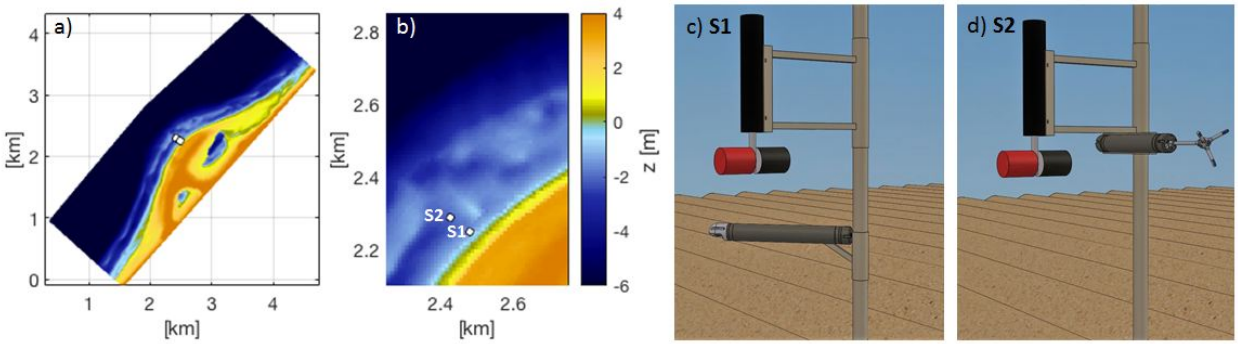

Figure I.1: Instrument setup at MEGAPEX. From left to right shows the Sand Engine, a zoom into the two bedform sampling locations (S1 and S2), S1 with an Imagenex Sonar and an ADCP, and S2 with an Imagenex Sonar and an ADV.

I.0.2 Marquillie, Luval, and Dolganov (2008) DNS over Hump Dataset

Abstract explanation of direct numerical simulation (DNS) over a hump model from Marquillie et al. (2008) (Figure I.2: *A direct numerical simulation (DNS) of a channel flow with one curved surface was performed at moderate Reynolds number (Re_τ = 395 at the inlet). The adverse pressure gradient was obtained by a wall curvature through a mathematical mapping from physical coordinates to Cartesian ones. The code, using spectral spanwise and normal discretization, combines the advantage of a good accuracy with a fast integration procedure compared to standard numerical procedures for complex geometries. The turbulent flow slightly separates on the profile at the lower curved wall and is at the onset of separation at the opposite flat wall. The thin separation bubble is characterized with a reversal flow*

fraction. Intense vortices are generated near the separation line on the lower wall but also at the upper wall.

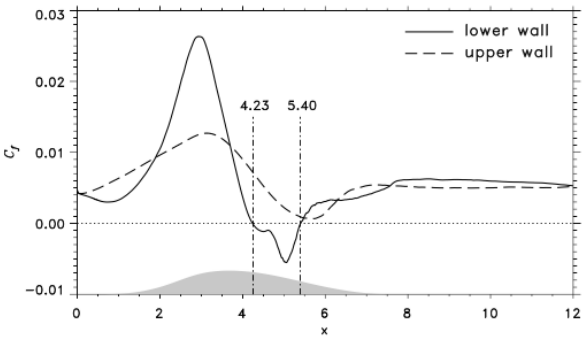

Figure 6: Skin friction coefficient $C_f = \tau_w / \left(\frac{1}{2}\rho U_{max}^2\right)$ (with $\tau_w = \mu \frac{d\langle u_t \rangle}{dy}|_{y=0}$) computed at the two walls with the mean tangential velocity $< u_x >$ averaged over $\Delta T = 9s$ and the maximum velocity at the inlet ($U_{max} = 1.03$). The separation region defined with negative shear stress is indicated with two vertical lines.

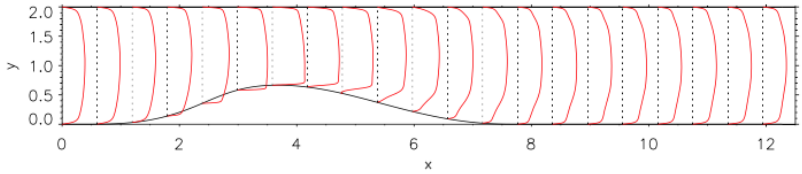

Figure 7: Profiles of mean streamwise velocity $\langle u_x \rangle$.

Figure I.2: Marquillie et al. (2008) figure 6 and 7 showing results from DNS simulation of unidirectional flow over a hump. Top panel shows boundary stress on top and bottom walls of channel as a function of x (distance along channel), bottom panel shows boundary layer profiles as a function of x.

I.0.3 Hagan and Dubief (2017) LES over Ripples Dataset

A Euler-Lagrange large eddy simulation (LES) dataset was created for the purpose of this research to understand the capabilities of the MIM in separated flows with a slip condition at the boundary. A coupled LES volume-filtered Eulerian flow and Lagrangian particle model are used to model unidirectional and oscillatory flow over an unfixed rippled bed. In order to limit computational time the flow field around individual particles is resolved, instead the Navier-Stokes equations are volume filtered, thus replacing flow characteristics (fluid velocity, pressure, etc.) by smoother, locally filtered fields and to close the equations

an effective viscosity is used to account for enhanced dissipation by the particles (Figure I.3). An adhesion model was used to more closely mimic natural sand mobility and periodic boundary conditions were used to simulate a fully-developed turbulent flow. Additionally, to interpolate the fluid variables to the particle location a second order trilinear interpolation scheme is used, and then a force balance is preformed to move the particle. Additional model details are outlined in Arolla and Desjardins (2014) and Omidyeganeh and Piomelli (2011). Simulations are preformed with particles with a 0.1 mm diameter initially set into ripples with 13 cm wavelength and a height of 2 cm. The flow field was forced in two ways, the first with unidirectional flow, and the second with an oscillating pressure gradient with 2.4 s period.

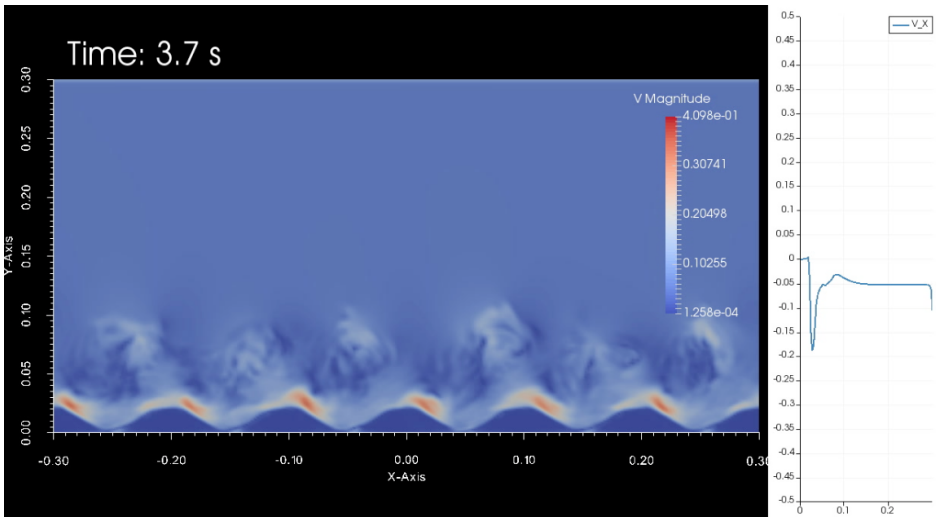

Figure I.3: Snapshot of LES model over ripples in oscillatory flow from Hagan and Dubief (2017) LES dataset. Left panel shows 2D flow field, right panel shows example velocity profile at crest of ripple.